Università di Modena e Reggio Emilia
Dipartimento di Scienze Chimiche e Geologiche
Doctoral School M3ES: Models and Methods for Materials
and
Environmental Sciences
Cycle XXXII

Ph.D. co-advised with

École Nationale Supérieure de Chimie de Paris
École Doctorale 388: Chimie Physique et Chimie Analitique de Paris-Centre

Computational studies of ceria-based catalytic materials

thesis presented by

Luca BRUGNOLI

M3ES Director: **Prof. Maria Giovanna VEZZALINI**
ED388 Director: **Prof. Alexa COURTY**

Committee:

Advisor: **Prof. Maria Cristina MENZIANI** (UNIMORE)
Co-Advisor: **Prof. Carlo ADAMO** (i-CLeHS /ENSCP ParisTech)
Examiner: **Prof. Alexis MARKOVITS** (Sorbonne Université)
Examiner: **Prof. Vincenzo BARONE** (Scuola Normale Superiore)

List of publications:

1. **Brugnoli, L.**; Ferrari, A. M.; Civalleri, B.; Pedone, A.; Menziani, M. C. Assessment of Density Functional Approximations for Highly Correlated Oxides: The Case of CeO_2 and Ce_2O_3. *Journal of Chemical Theory and Computation* **14**, 4914–4927 (2018). https://doi.org/10.1021/acs.jctc.8b00600.
2. Gasperi, G.; **Brugnoli, L.**; Pedone, A.; Menziani, M. C.; Valeri, S.; Luches, P. Reducibility of Ag- and Cu-Modified Ultrathin Epitaxial Cerium Oxide Films. *The Journal of Physical Chemistry C* **123**, 13702–13711 (2019). https://doi.org/10.1021/acs.jpcc.9b02378.
3. **Brugnoli, L.**; Pedone, A.; Menziani, M. C.; Adamo, C.; Labat, F. H_2 Dissociation and Water Evolution on Silver-Decorated CeO_2(111): A Hybrid Density Functional Theory Investigation. *J. Phys. Chem. C* **123**, 25668–25679 (2019). https://doi.org/10.1021/acs.jpcc.9b06805.
4. **Brugnoli, L.**; Pedone, A.; Menziani, M. C.; Adamo, C.; Labat, F. O_2 Activation Over Ag-Decorated CeO_2 (111) and TiO_2(110): a Hybrid DFT Comparative Investigation. (In preparation).

Riassunto

I materiali a base di ossido di cerio (ceria) sono ampiamente impiegati nell'ambito della catalisi eterogenea come: abbattimento e controllo delle emissioni dei veicoli a motore a combustione interna, produzione e purificazione di idrogeno e in dispositivi per la conversione dell'energia pulita come nelle celle a combustibile. In queste applicazioni, spesso, l'azione catalitica è il risultato della sinergia tra la ceria e gli altri elementi, generalmente metallici, che incrementa la reattività, la selettività e la stabilità delle componenti attive. La modellizzazione teorica di questi materiali e dei fattori che ne regolano l'attività catalitica è di grande utilità al fine di progettare catalizzatori nuovi o migliorati, con un minore contenuto di metalli preziosi, diminuendone il costo e promuovendone l'utilizzo nelle applicazioni sopracitate. In questo lavoro di tesi, la reattività delle superfici ideali, con difetti e modificate dell'ossido di cerio è stata simulata attraverso l'uso della Teoria del Funzionale della Densità (DFT) applicata a modelli periodici. In primo luogo, la valutazione di diverse famiglie di funzionali ibridi, sulle proprietà di stato fondamentale delle fasi cristalline degli ossidi di cerio, CeO_2 e Ce_2O_3, e della superficie (111) di CeO_2 con vacanze di ossigeno ha permesso di definire dei protocolli di calcolo robusti, adatti ad essere estesi alla modellizzazione della reattività. Il funzionale ibrido PBE0 è stato selezionato come il più performante, in combinazione con un adatto set di base di funzioni Gaussiane, centrate sugli atomi.

Successivamente, la più alta riducibilità CeO_2 (111) dopata con Cu e Ag osservata sperimentalmente è stata razionalizzata facendo uso di semplici modelli di dopaggio sostitutivo per valutare l'energia di formazione di vacanze di ossigeno compensative di carica e attive. I conti DFT hanno trovato una maggiore riducibilità per la ceria dopata con Ag, data la più bassa energia di formazione delle vacanze di ossigeno.

In seguito, gli effetti di un cluster di argento (Ag_{10}) supportato su CeO_2(111) sulla riducibilità superficiale e sulla reattività nei confronti della dissociazione di H_2 e la formazione di H_2O sono stati caratterizzati: la deposizione del cluster induce la riduzione della superficie di ceria per trasferimento di carica dal cluster agli ioni di cerio sotto di esso. La formazione di vacanze di ossigeno è soppressa lungo il perimetro dell'interfaccia. La barriera di attivazione per la dissociazione di H_2 risulta minore in presenza della particella di Ag, in particolare sui siti di contatto tra ossido e metallo. Anche la cinetica di formazione di H_2O è favorita dalla presenza di Ag, mentre, complessivamente, tutte le reazioni diventano più endotermiche.

Infine, è stata studiato il processo della dissociazione riduttiva di O_2 su superfici con difetti di ossigeno di ceria e di rutilo, sia nude che in presenza del cluster Ag_{10} precedentemente considerato. La reazione risulta favorita sulla ceria, e il cluster di argento promuove la reazione.

Résumé

Les matériaux à base d'oxyde de cérium (cérine) sont largement utilisés dans les catalyseurs hétérogènes tels que la réduction et le contrôle des émissions des véhicules à moteur à combustion interne, la production et la purification de l'hydrogène et dans les dispositifs de conversion de l'énergie propre comme dans les piles à combustible.

Dans ces applications, l'action catalytique est souvent le résultat de la synergie entre la cérine et les autres éléments, généralement métalliques, qui augmente la réactivité, la sélectivité et la stabilité des composants actifs. La modélisation théorique de ces matériaux et des facteurs qui régulent leur activité catalytique est très utile pour concevoir des catalyseurs nouveaux ou améliorés, à plus faible teneur en métaux précieux, réduisant leur coût et favorisant leur utilisation dans les applications mentionnées ci-dessus. Dans ce travail de thèse, la réactivité des surfaces idéales, défectueuses et modifiées en oxyde de cérium a été simulée par l'utilisation de la théorie de la densité fonctionnelle (DFT) appliquée à des modèles périodiques. Tout d'abord, l'évaluation des différentes familles d'hybrides fonctionnels, sur les propriétés d'état fondamentales des phases cristallines des oxydes de cérium, CeO_2 et Ce_2O_3, et de la surface (111) du CeO_2 avec vacances d'oxygène a permis de définir des protocoles de calcul robustes, extensibles à la modélisation de la réactivité. L'hybride fonctionnel PBE0 a été sélectionné comme le plus performant, en combinaison avec un ensemble de fonctions gaussiennes de base appropriées centrées sur les atomes. Par la suite, la réductibilité plus élevée de CeO_2 (111) dopée au Cu et à l'Ag observée expérimentalement a été rationalisée en utilisant des modèles simples de dopage de substitution pour évaluer l'énergie de compensation de charge et la formation de vacances d'oxygène actif. Les comptes DFT ont trouvé une plus grande réductibilité pour les ceriums dopés à l'Ag, étant donné la faible formation d'énergie des vacances d'oxygène.
Par la suite, les effets d'un cluster d'argent (Ag_{10}) supporté sur CeO_2(111) sur la réductibilité et la réactivité de surface vis-à-vis de la dissociation H_2 et la formation de H_2O ont été caractérisés : le dépôt de cluster induit la réduction de la surface de cérine par transfert de charge du cluster aux ions cerium inférieurs à celui-ci. La formation de vacances d'oxygène est supprimée le long du périmètre de l'interface. La barrière d'activation de la dissociation de H_2 est plus faible en présence des particules d'Ag, en particulier aux sites de contact entre l'oxyde et le métal. De plus, la cinétique de la formation de H_2O est favorisée par la présence d'Ag, alors que, globalement, toutes les réactions deviennent plus endothermiques. Enfin, le processus de dissociation réductrice de l'O_2 sur des surfaces présentant des défauts oxygénés de cérine et de rutile, à la fois nues et en présence du groupe Ag_{10} précédemment considéré, a été étudié. La réaction est favorisée sur la cérine et le cluster d'argent favorise la réaction.

Contents

Chapter 1: Introduction and scope

1.1 Introduction

One of the most important classes of materials in heterogeneous catalysis is represented by metal oxides, which find applications for many industrial and environmental processes.
Environmental catalysis, in particular, plays a fundamental role in improving the quality of life and it is necessary for a sustainable future, being involved in processes spacing from the removal of pollutants from air and water, waste treatment, greenhouse gases abatement to the exploitation of renewable energy sources and the production of cleaner energy vectors, as H_2, for instance.
Their importance rises from the middle 1950s, when it was discovered their efficiency as catalysts for a wide range of reactions, in particular for redox and acid-base ones.
In many cases, the oxide is used as support for small metallic particles catalytically active: the particles are distributed on the high-surface area of the oxide (such as silica, alumina, titania or ceria, for instance), which allows a more efficient use of the metal. Depending on the nature of the metal-oxide interaction, the catalytic activity can results enhanced compared with the stand-alone components, due to the peculiar structure and electronic properties of the junction.
Molecular modelling, more specifically electronic structure methods, are essential to reach an understanding at the atomistic level of these materials and of the complex processes involving them, in order to design new catalysts or improve existing ones.
Among metal oxides, ceria is one of the most intriguing and challenging to be modelled and it is the main subject of this thesis.

1.2 Ceria

CeO_2 is the most relevant oxide of a rare-earth element with industrial applications.
Ceria is the paradigm of the reducible oxides, due to its capability of readily exchange oxygen with the environment (oxygen storage capacity, OSC) depending on the redox potential at the interface.
Initially ceria was believed to be an inert support, able to disperse and stabilize the metallic active phases, but later its non-innocent role of active O buffer lead to its use in many catalytic processes, first of all in the catalytic conversion of the exhaust of the auto-vehicles.
The OSC is intrinsically bound to the easy interconversion $Ce^{4+} \leftrightarrow Ce^{3+}$, the two possible oxidation states of Ce in ceria-based materials. This redox process involves the occupation/depletion of atomic-like Ce 4*f* states, highly localized on the Ce ions. An accurate modelling of this feature is quite challenging for the theoretical tools routinely used for investigating the electronic structure of

more conventional materials, hence a lot of efforts have been spent to reach a satisfactory theoretical description of ceria-based compounds.

1.2.1 The stoichiometric cerium oxides

Metallic Ce exposed to O_2 oxidises forming a series of oxides of stoichiometry CeO_x, with x comprises between 3/2 and 2. CeO_2 and Ce_2O_3 are respectively the fully oxidised (Ce^{4+}) and the fully reduced (Ce^{3+}) oxides.

A satisfactory reproduction of the main structural and electronic properties of the two oxides has been since long considered necessary in order to validate a computational methodology suitable to describe ceria-based materials, since they are characterized by the simultaneous presence of both the oxidation forms of Ce.

The following sections reports the experimental data of the main observables computable for these oxides.

1.2.2 CeO_2

CeO_2 crystallizes in the fluorite (CaF_2) structure (see **Figure 1a**), in the same cubic face centred spatial group $Fm\bar{3}m$.

The structure is fully defined by the lattice parameter *a*, being the Ce at the origin (0, 0, 0) and the O at (¼, ¼, ¼). The Ce cation, formally Ce^{4+}, is coordinated to 8 O^{2-}, and each anion is coordinated to 4 cations, with overall 4 Ce and 8 O in the conventional cell.

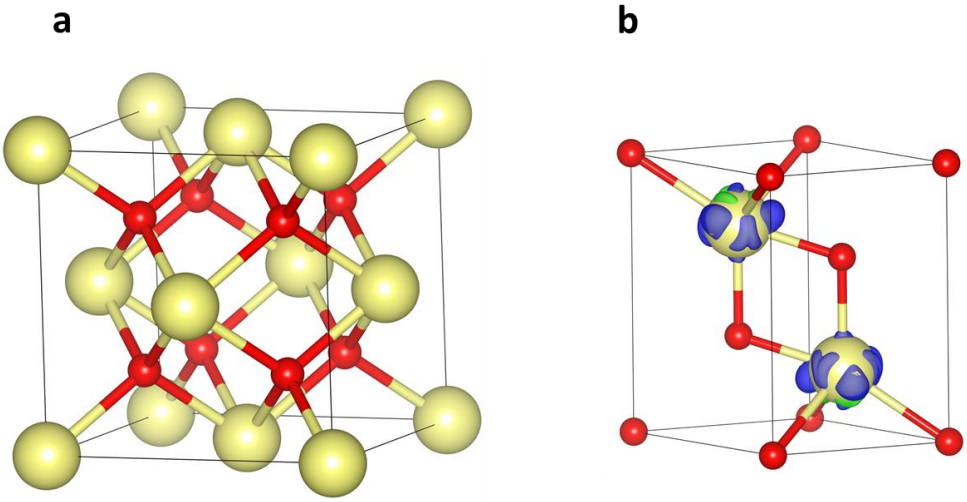

Figure 1: Conventional cells of CeO_2 (a) and phase-A Ce_2O_3(b).

The experimental lattice constant is 5.411 Å [1] at room temperature (rt) and 5.391 Å extrapolated at 0 K[2]. The adiabatic Bulk Modulus B_0, derived by the measured elastic tensor components, is 204

GPa. Considering also the results obtained by using the equation of state (EOS), the experimental results for B_0 range between 204 and 236 GPa[3,4].

The vibrational spectrum is very simple, with 1 active mode IR at 272-283 cm^{-1} of F_{1u} symmetry [5,6] and 1 active mode Raman at 465 cm^{-1} of F_{2g} symmetry[5].

Ceria is an insulator characterized by two band gaps: a regular gap of about 6 eV and a forbidden gap of about 3 eV. The top of the valence band is formed by O 2*p* states, while the lower conduction is formed by a narrow band formed by localized Ce 4*f* empty states, 3 eV above the valence, and by a delocalized Ce 5*d* band about 6 eV above the valence. The gap 2*p*-5*d* gap of about 6 eV is the regular gap, while the 2*p* – 4*f* of about 3 eV is the forbidden gap.

The experimental values reported in the literature for the two band gaps strongly depend on the experimental conditions used. As a consequence, a wide interval of the measured data values is available for the forbidden gap (2.6-3.4 eV) and for the regular gap (5.5-8.4 eV).[2] This prevent to drawn strict conclusions when comparing the computed values with the experimental ones.

As in previous works, we use as reference values 6 eV and 3 eV for the two gaps.

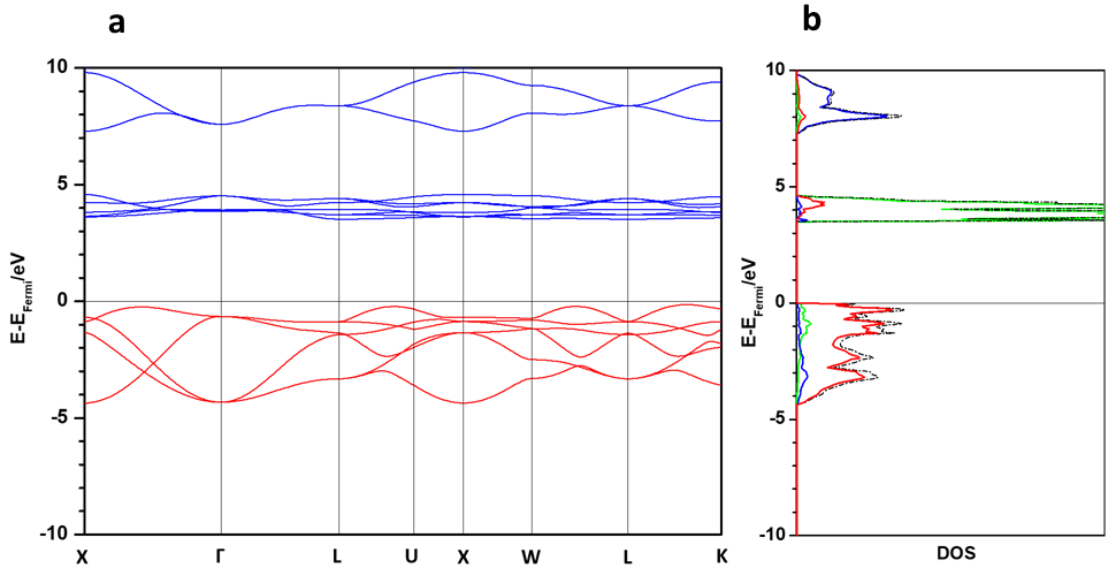

Figure 2: Band structure (a) and projected density of states (b) of the ideal CeO_2 computed at the HSE06 level. In (a) conduction and valence bands are in blue and red lines, respectively. (b) Total and projected density of states: in red, green, blue and black lines the O 2*p*, Ce 4*f*, Ce 5*d* and total projections.

1.2.3 Ce_2O_3

The gradual reduction of the CeO_2 in H_2 leads to the formations of reduced phases with a continuous composition range, up to reach the totally reduced sesquioxide Ce_2O_3. As for the other rare-earth oxides, the sesquioxide can crystallize in three distinct phases: phase A, hexagonal; phase

B, monoclinic; and phase C, cubic. The hexagonal phase (s.g. $P\bar{3}m1$) is the most thermodynamically stable form in the range of temperature and pressure of employment of these oxides, therefore we limit our investigation to this phase.

The structure is characterized by 2 cell parameters, *a* and *c*, and by 2 internal parameters, u_{Ce} and u_O, respectively 3.891 Å, 6.059 Å, 0.2454 and 0.6471, at rt [7].

The measured Bulk Modulus values are 111 GPa (quasi-hydrostatic) and 104 GPa (non-hydrostatic)[8].

The vibrational data are limited to the Raman spectra[9], while for the IR only data obtained on the products of calcination of the cerium carbonate are available[10]. According to group theory, the 12 vibrational modes of the unit cell are classified in 4 Raman active modes of symmetry E_g (409 cm^{-1}), A_{1g} (409 cm^{-1}), A_{1g} (189 cm^{-1}) and E_g (103 cm^{-1}) and 4 IR active modes of symmetry E_u, A_{2u}, E_u, A_{2u}. Concerning the electronic structure, the oxide is a Mott insulator with an antiferromagnetic ground state and an effective magnetic moment of 2.17 μ_B/mol[11], indicative of one 4*f* e^- per Ce atom of the unit cell. Above 8.5 K the transition from the antiferromagnetic to ferromagnetic occurs, with no-changes measured in the lattices structure. The Ce 4*f* band splits in an occupied narrow band, on top of the valence of the oxide, and in an unoccupied diffuse band, mixed with the Ce 5*d* band, at the bottom of conduction.

The observed optical gap is 2.4 eV[12], which constitutes a lower limit for the computable fundamental gap, for which no measurements have been reported.

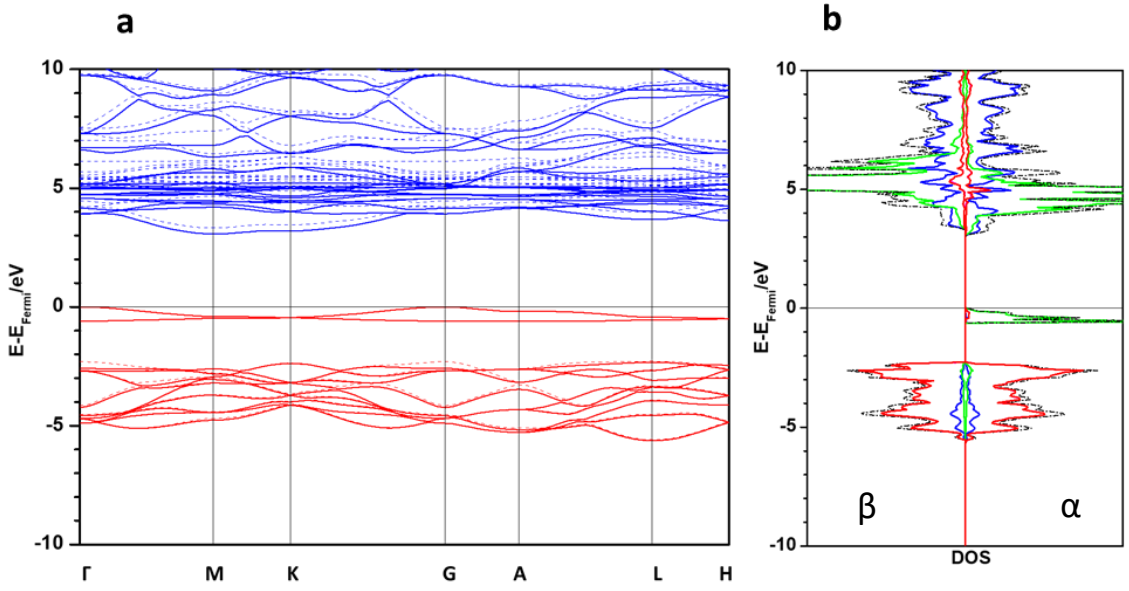

Figure 3: Band structure (a) and project density of states (b) of the ideal Ce_2O_3 computed at the HSE06 level. See caption Figure 2 for the colour legend. In (a) solid and dashed lines are used respectively for α and β bands. (b) Total and projected density of states: in red, green, blue and black lines the O 2*p*, Ce 4*f*, Ce 5*d* and total projections.

Lastly, we considered the enthalpy of the reduction of CeO_2 to Ce_2O_3 derived from the tabulated heat of formation[13]:

$2CeO_2 \rightarrow Ce_2O_3 + \frac{1}{2}\ O_2$; $\Delta H = 4.03$ eV (R1)

$2CeO_2 + H_2 \rightarrow Ce_2O_3 + H_2O$; $\Delta H = 1.54$ eV (R2)

R1 and R2 are equivalent reactions to express the reduction of the bulk phases, but R2 does not incur in open-shell molecules.

1.3 Applications of CeO_2 in catalysis

The first relevant application of CeO_2 in catalysis is found in the three-way catalysts (TWCs) of the automotive catalytic converter[14], the most relevant example of environmental catalysts.

The purpose of the TWCs is to simultaneously oxidise CO and non-combusted hydrocarbons (HCs) and to reduce nitrogen oxides (NO_x) produced from the combustion of gasoline.

The catalytic device is composed by: a thermally stable support made of Al_2O_3; a disperse active phase constituted by noble metals nanoparticles (Pt and/or Pd for oxidation, Rh for reduction) and the ceria promoter (usually doped with ZrO_2). The catalyst works optimally in a narrow interval of air/fuel ratio, difficult to maintain constant due to the fluctuant combustion regime of the engine: ceria acts as oxygen buffer, extending the window of work by releasing O_2 in O lean condition, then up-taken in O rich regime[15,16].

Nowadays this technology can be considered mature, with room for improvements limited essentially to the reduction of the quantity of active precious metals.

In addition to CO, CHs and NO_x, diesel engines release also soot: the abatement of this harmful pollutant requires the use of filters, regenerated by the catalytic activity of the coating in ceria, which highly decrease the temperature of combustion of soot.

The trapped soot reacts at the contact with the ceria catalyst: O_2 is activated at the ceria-soot interphase, oxidising the soot to CO/CO_2. Furthermore, NO_2, catalytically formed by NO and O_2 on CeO_2, contributes to the oxidation of the soot. To these purposes, alkaline metals doped-ceria, nano-structured ceria and ceria supporting Co_3O_4 catalysts show much higher performance with respect to pristine ceria [17,18].

One of the most promising applications for ceria is as constituent of the solid oxide fuel cells (SOFCs), a very attractive class of fuel cells, with the only output being electricity, heat and water, if H_2 is used as fuel. The oxidation of the fuel involves the extraction of O from the anodic oxide surface, which is replenished by the flux of O^{2-} across the electrolyte, and generate at the cathode, where occurs the reduction of O_2.

Ceria can be used in many components of the SOFCs: as solid electrolyte; as a barrier layer between the electrodes and the YSZ(yttria-stabilized-zirconia) electrolyte, to prevent side reactions; as co-catalyst at both anode and cathode[19,20].

The solid electrolyte exploits the ionic conducting and electronic insulating properties of ceria: the stable fluorite type structure of this oxide allows the support of high concentration of oxygen vacancies (V_O), without undergo relevant structural reconstruction, enabling relatively high O^{2-} conductivity even at intermediate temperatures (800-1110 K).

Dopants as Gd, Sm, Y and Ca increase the concentration of V_O and the O^{2-} conductivity, as well nanostructures, since oxide ions diffuse faster at the grain boundaries than on the bulk[21,22].

The adoption of ceria as co-catalyst contrast the carbon deposition, allowing to feed directly CHs fuels to the anode[23]. Furthermore, with ceria at the anode, the tolerance to sulphur (H_2S) in the H_2 feed is highly enhanced[24]. Examples of promising anodic composition are Gd-doped ceria, Ru-CeO_2, Cu-CeO_2, Pd@CeO_2 core-shell and microspheres of ceria[25]

Besides SOFCs, ceria finds application also in the polymer electrolyte-membrane fuel cells (PEMFCs), albeit at a lesser.

Ceria combined with the conventional Pt/C catalyst enhances the rate for the oxygen reduction process[26]. Similarly, the nanocomposite CeO_2-Pt/C exhibits higher resistance to corrosion and to loss of performances compared to Pt/C alone[27].

Being ceria soluble in acidic conditions, an alternative route is the development of alkaline PEMFCs: in addition to ceria stabilization, the basic environment would allow also the use of metals less precious than Pt.

For instance, a direct ethanol PEMFCs with an anode of Pd on CeO_2/C has been successfully produced. The ceria support has a decisive role, being the energetic efficiency halved if only the Pd/C catalyst is employed[28].

Another emerging use of CeO_2 is in the H_2 production and purification technologies. The research of ceria-based catalyst for use in reforming (stream/dry/autothermal reforming) has grown exponentially in the last two decades. The most promising results come from ceria-zirconia mixed oxide, used as active support for several metal nanoparticles, including Co,Ni, Pt, Ru, Rh, Au, Ag and Cu[25]. Methane is the primary feed to the reforming, since the process forms much less coke than with higher HCs, however adding ceria to the conventional Ni/SiO_2/Al2O_3 catalyst hinders the coke deposition[29]. Pd-ceria based catalyst, instead, shows stable reaction rates in the steam-reforming of light HCs as n-butane[30].

The syn-gas generated from reforming necessitates a treatment to adjust the composition before being employed in specific processes. For instance, ammonia production requires the almost total

abatement of CO, as well the H_2 feed to PCMFCs. To purify H_2 from CO, the most promising approach is to combine the water-gas-shift reaction (WGSR) and the preferential oxidation (PROX) of CO in excess of H_2, with O_2. For these processes, many noble and non-noble metals supported on ceria (doped or not) can act as active catalyst. Pt, Au and Cu are among the most promising and investigated systems[29,31].

In the field of waste-treatment, ceria-based materials are particularly efficient for VOCs catalytic combustion, due to their extraordinary oxidation properties. Following the MvK mechanisms, ceria donates O to the organic reactant, and it is successively re-oxidized by O_2. Many researches concern the methane oxidation, because of its hazardous global warming and ozone depletion effects. Doped ceria and noble metal (Pd, Pt, Au) supported ceria highly decrease the optimal combustion temperature, beneficial to the lifetime of the catalyst.

Chlorinated VOCs are another critical class of compounds for their toxicity and stability, widely used in the industries, for which ceria-based catalysts are promising candidates for their oxidation[32, 33]. Similarly, also the oxidation of HCl, by-product of many important chemical processes, can be accomplished by ceria supported on zirconia[34].

For the selective hydrogenation of alkyne to olefins ceria possess an extraordinary stand-alone activity, higher than the state of the art and expensive Lindar's catalyst, with the only drawback of higher working temperature and pression, due to the slow kinetic for the H_2 activation.

As photocatalyst for wastewater treatment and for water-splitting, ceria has drawn a lot of interest in the past decade as possible alternative to TiO_2, being active in the near UV. Despite many promising results and the possibility to modulate the electronic gap with nano-structuring and doping, the performance so far achieved are much less promising than for other visible light photocatalysts[25].

Much more fruitful is the research in the thermochemical water splitting: by employing concentrate solar energy as source of heat, high conversion rates solar to fuel are achieved.

In the process, H_2O and CO_2 splitting occurs simultaneously on the thermally reduced ceria.

The rapid redox kinetic and the high thermal stability have bestow to ceria the role of state-of-the-art catalyst in this field[35].

Lastly, being biocompatible, ceria finds uses also in the biomedical sector: consequently to the OSC it exhibits many enzymatic mimetic activities as radical scavenger, superoxide dismutase and more[36]. In particular, nanoceria is able to protect rodent neurons from oxidative stress[37].

1.4 Modelling ceria and ceria-based materials

Most calculations on CeO_2 based systems have been performed with the Kohn-Sham Density Functional Theory (KS-DFT), being the best performing approach, in terms of ratio accuracy vs computational cost, to deal with extended systems as materials and macromolecules.
Unfortunately, the quality of any DFT calculation results significantly depend on the chosen density functional approximation (DFA). This aspect will be further discussed in chapter 3.
Literature reports a large number of papers concerning DFT works on ceria, accounted up to 2013 in the excellent review of Paier *et al*[38].
In the following, the principals challenge concerning the modelling of the ceria-based materials are discussed.

1.4.1 Stoichiometric Bulk-phase

The valency of Ce in ceria has been long debated in both experimental and theoretical material research, being problematic to obtain evidence on the occupation of the 4*f* states. The simplest vision was to consider the compound fully ionic, therefore with a tetravalent Ce in the $4f^0$ configuration, in contrast with the mixed tri/tetra valency of static or time-evolving nature, revealed by X-ray spectroscopy[16, 39, 40, 41].
The first electronic structures investigation on Ceria date back to 1983, when Koelling *et al.*[42] performed Linear Augmented Plane Wave (LAPW) calculations, adopting the Slater exchange (SX) functional, to investigate the role of the *f*-electrons in the isostructural CeO_2 and PrO_2. The works shows a non-zero occupation of the 4*f* orbitals, which partially hybridize with the O 2*p* orbitals of the valence band, as well the Ce 5*d* orbitals, enlightening a degree of covalency in ceria.
Later on, Hill and Catlow[43] performed all-electron restricted Hartree-Fock calculations to investigate the structural, thermodynamic and electronic properties: the work, despite the minimal GTO basis set used that discarded the 4*f* orbitals, provided an adequate description of this oxide, in agreement with the Hartree-Fock performance on other main-groups oxides. The lack of the 4*f* orbitals has been considered not critical to define the ground state properties of the oxide, since also when reduced up to 20%, thus with occupied 4*f* orbitals, the lattice parameter of ceria shows minimal variation from the stoichiometric one.
The problem of the occupation of the 4*f* states and their role in bonding was tackled again in 2001 by Skorodumova *et al* [44], which performed LDA and GGA calculations with the full potential linear muffin-tin orbitals method (FP-LMTO) to investigate some structural and optical properties of the CeO_2 and Ce_2O_3. They adopted two distinct models for the 4*f* states of Ce: the valence band model

(VBM) and the core state model (CSM), which treated the 4*f* electron respectively as valence electron and as localized core state.

With both LDA and GGA, the VBM provided more accurate results for CeO_2; instead, the CSM gives the best description of Ce_2O_3. Their results suggested that the 4*f* electron do not significantly contribute to the bonding in Ce_2O_3, while in CeO_2 the unoccupied 4*f* states behave essentially as empty atomic orbitals. Moreover, at difference with Hill and Catlow investigations, the description of the bonding for CeO_2 and Ce_2O_3 is closer to ionic polarized than partially covalent. In a following publication, Skorodumova *et al*[45] proposed an explanation for the reversible transition CeO_2-Ce_2O_3 (cubic phases) associated with the process of Vo formation and migration: adopting the same approach as in their previous work, they found that when a Vo forms in bulk CeO_2, the 2 extra electrons of the oxide ion O^{2-} are left in the lattice and localize over 2 of the Ce nearby, which are reduce to Ce (III). By sampling many possible configurations for the 2 Ce^{3+} with respect to the vacancy, they found that the most stable one for both is with V_O as the nearest neighbour. Then, they proposed that the mechanism of the V_O migrations involves the transfer of 2 e^- from the O to 2 Ce^{4+} when the vacancy forms and from the 2 Ce^{3+} to the O when the vacancy leaves. However, the problem with this approach was that the Ce^{3+} ions were assigned in input of the calculation by treating them with the CSM, while the others Ce^{4+} were considered with the VBM. Instead, when the VBM is adopted for all the Ce, the material results metallic, with the 4*f* electron density delocalized over the whole system, with a similar fractional occupation of the 7 cartesian 4*f* orbitals of each Ce.

This ill description, in contrast with the experimental evidence of a narrow localized occupied band of 4*f* character at about 1.5-2 eV above the top of the O 2*p* band of defective ceria, is due to the self-interaction error (SIE) intrinsic in the LDA and GGA formulation. The pathological effects of SIE (see chapter 2) are evident when dealing with the so-called highly correlated materials as ceria, NiO_2 and many other transition state and rare-earth compounds, since an erroneous description of the electronic structure is provided.

One method to deal with SIE is by adopting the Self Interaction Correction (SIC)[46] to the LDA: on cerium oxides, this approach resulted successful in separating the 4*f* manifold of the sesquioxide into a valence and a conduction band, correctly describing Ce_2O_3 as insulant(AFM)[47], but it was soon abandoned in favour of other methods.

One alternative is the so-called DFT + U approach[48,49]: the functional (LDA or GGA) is corrected for on-site Coulomb correlation effects by an Hubbard-type term, U, orbital specific.

This scheme was first adopted on the cerium oxides by Fabris *et al*[50,51] and by Nolan *et al*[52], which investigated respectively the bulk oxides and the low index reduced surfaces of CeO_2. This

methodology provided a satisfactory description of the Ce^{4+} and the Ce^{3+} oxides and of the mixed valency of reduced CeO_2. In fact, the results correctly localize the 4*f* electrons on 2 Ce nearest neighbour to V_O, allowing an accurate description of the physics of the mixed-valency ceria systems.

Being the computed properties highly sensitive to the value of U_{eff}, the effective on-site potential acting on the 4*f* orbitals, many studies focused on finding the best value. The main approach was to fit U_{eff} to an experimental observable, such as the band gap, the lattice constants or the energetic of a reaction.

One other approach is to compute the best value of U with a variational method (self-consistently) as from linear response theory[79].Whichever approach is used, the U value chosen does not reproduce all the ground-state properties of these oxides satisfactorily. However, some author claims that LDA+U, with U_{eff}=6 eV provides a satisfying description of pristine ceria and of the polaronic Ce^{3+} state[53,54], superior to the more sophisticated hybrid functionals, without need to include the thermochemistry of reduction.

The DFT+U, successfully applied on many other correlated materials with semi-occupied *d* or *f* shells, has allowed the investigation of processes as the effects of doping, the adsorption of small molecules and metal particles on the surface, vacancies migration and catalytic reactions. Despite the ability to localize the occupied 4*f* states, it still suffers from the other shortcomings of the LDA or GGA functionals, as, for instance, a bad description of the transition state structures and underestimation of the related activation energies[55,56].

Better results concerning reactivity are expected to come from the employment of hybrid functionals[57]: Hay *et al*[58] were the first to perform an investigation of the cerium oxides at the hybrid level with the range separated functional HSE06, obtaining much accurate structural, electronic and magnetic properties with respect to LDA, PBE and the meta-GGA TPSS. Successively, De Silva *et al* [59]compared the performances of hybrid DFT (HSE06 and PBE0) with DFT and DFT + U (LDA and PBE): the hybrids, especially HSE, provided a more accurate description, but shortcomings as the underestimation of the enthalpy of reduction were underlined. Kullgren *et al*[60] performed another assessment of hybrid DFT (B3LYP and PBE0), conventional DFT and DFT+U: they found LDA+U more accurate for structure and electronic properties, but the investigation did not account for the energetic of reduction. Moreover, their work showed that GTO and PAW basis set could provide very similar results if care in the choice of the GTO basis set is taken.

Another hybrid DFT investigation with GTOs basis set on the cerium oxides was performed by Graciani *et al*[61]: they investigated the dependence of the calculated structural, electronic and

thermochemical properties on the fraction of HF exchange (or exact exchange, EE), in particular the effect on the energetic of the reaction of reduction. The optimal value falls in the range 10-28 %, depending on the local component of the hybrid functional (PBE0, B3LYP and B1WC), with B1WC overall best performer in the original formulation with 16% of EE.

1.4.2 Oxygen vacancy at surfaces

In materials, very often the most important properties depend, directly or indirectly, on the presence of defects. In oxides and ceramics point defects as vacancies or interstitial are dominant. These defective centres affect the optical, electronic and transport properties of the material, as well the surface chemistry.

In oxides, the oxygen vacancy is probably the main type of defect. It is naturally widespread in oxide, isolated or associated with other defects. According to the tendency to form the Vo, the oxides can be classified as reducible and non-reducible[62].

O vacancies form in all oxides by lowering the partial pressure of O_2 and increasing T, but in reducible oxides they forms in mild conditions, while in non-reducible ones high T and ultra-high-vacuum conditions[38] are required.

The aptitude of ceria to form O vacancies makes it the paradigm of the reducible oxides.

The presence of O vacancies highly affects reactivity (since they act as anchoring sites for metal particles or other substrates) and highly influence the activity and selectivity of the catalyst[63]. In oxidation catalysis, the oxide ions in the lattice act as reservoir of oxygen, which can be released or uptake at the catalyst surface depending on the redox environment. Therefore, the activity of the catalyst is correlated with its ability to release the oxygen, i.e. the cost to form an oxygen vacancy. Since the formation of an oxygen vacancy alters the structural and electronic properties of the material, and as consequence its reactivity, the microscopic understanding of these phenomena is thus helpful to design materials with a controlled activity for specific applications.

With this goal, a large amount of experimental and theoretical works has been done to characterized O vacancies in ceria-based materials.

In the following we report a short comprehensive of the main results obtained.

1.4.3 Experimental findings

When an O atom is removed from the lattice, two electrons are left behind in the formed vacancy, and are accepted by two Ce, reducing them to Ce3 ($4f^1$). In the Kroger-Wink notation the process is:

$$O_O^X + 2Ce_{Ce}^X \rightarrow V_O^{\bullet\bullet} + 2Ce'_{Ce} + \frac{1}{2}O_2(g)$$

or alternatively:

$$O^{2-} + 2\,Ce^{4+} \rightarrow 2\,Ce^{3+} + \frac{1}{2}O_2(g)$$

The variation of the oxidation state can be followed by X-ray photoelectron spectroscopy (XPS), which detects the occupation of the 4*f* states or the characteristic shifts in the Ce 3*d* core levels, allowing the quantification of the degree of reduction of the material (surface). However, this technique provides only a spatially averaged information, without relating the localization of the 4*f* states to the vacancy positions. Instead, surface analysis techniques as scanning tunnelling microscopy (STM) and atomic force microscopy (AFM) can provide images of the first atomic layers of the material, detailed at the atomistic level. The vacancies at the (111) surface have been long investigated with these methods, revealing asymmetric structural distortions around the vacancy site: the Ce atoms first neighbour to the Vo move away from it, while the O atoms second neighbour move towards the vacancy. The formed Ce^{3+} have a larger ionic radius of the Ce^{4+}, thus the structural relaxation to different Ce-O bond distances is observed.

These V_O form both at surface and subsurface sites (for CeO_2 111), with similar concentrations, according to STM measures. Combining the STM measurements with the DFT results a spatial correlation between the surface vacancy and the associated Ce^{3+} pair[64] was obtained, remarking the importance of the combined experimental-theoretical approach.

1.4.4 Theoretical investigations

The modelling of a solid requires first to choose between a finite cluster model and a infinite periodic model. While the first offers the possibility to use sophisticated post-HF methods, the obtainable results would be extremely dependent on the size, shape, and morphology of the clusters. The periodic model, instead, is ideal to model perfect crystals or crystalline surfaces, but also imperfections as defects can be included: changing the size of the periodic cell is possible to model different concentration of defects or adatoms, but with the isolated defect out of reach.

The surfaces of ceria are an interesting model system for the study of reactions of catalytic interest, therefore they have been investigated since long. The three most thermodynamically stable low index surfaces are, in decreasing order of stability, the 111, the 110 and the 100, as shown by XPS and LEED (low-energy electron diffraction) measurements and by force-field, Hartree-Fock[65] and DFT[66] calculations.

Conventional DFA fails to describe the Vo in ceria: the first GGA (PW91) investigation[67] of the reduced surfaces found the excess of electrons delocalized over the whole system, which resulted

metallic. Moreover, no asymmetrical distortions around the vacancy sites has been obtained following the structure relaxation. Despite this incorrect description, the authors argued that the energetic of the process of formation of the Vo was reliable for the capability of the GGA to reproduce the reduction energy of the bulk phases.

Successively, Fabris *et al*[68] investigated the formation on the (111) and (110) facets and on the bulk ceria with the DFT+U (LDA and PBE) methodology. As shown for Ce_2O_3, the Hubbard method was able to localize the excess of electrons in 4*f* atomic like orbitals, correctly describing the material as insulant. However, the work shown a rather unsettling dependence of the computed energies of formations (E_{fv} (½ O_2)) on the projectors adopted to solve the KS equations (atomic orbitals or Wannier functions), which varied in a range of 3.2 eV. Noland *et al* computed the E_{fv} with PW91+U the Vo for the 111, 110, 100 facets consistently for the same V_O concentrations Θ=¼, confirming the easier formation of Vo at 110 with respect to 111. Overall, the formation of the Vo at the surfaces has revealed easier for the surface with respect to the bulk, with an energy difference of about 30% for the 111.

Other investigations adopted cluster models to study the Vo: Burrow *et al*[69] used the hybrid functional PBE0 to model the defect in bulk and 111 ceria, adopting electrostatically embedded clusters along with Periodic Boundary Conditions. Despite the correct localization of the Ce3+ centres, the trends obtained for the formation energies of the vacancy disagree from most of other investigations: the bulk vacancy resulted more stable than the surface vacancy, and the subsurface vacancy less stable than the superficial one. These deviations may be ascribed to the use of a large core ECP for Ce in the geometry optimization, retained inaccurate for the description of the Ce^{3+} form by Kullgren *et al*[60].

Herschend *et al*[70] instead adopted HF and MP2 on a isolated cluster to model the Vo on CeO_2 110, obtaining the same localization features of the DFT+U approach.

1.4.5 Configurations of the defects

The works discussed so far found the 4*f* density localizes on the Ce first neighbour to the defect, i.e. nearest neighbour to the vacancy. Ganduglia-Pirovano *et al*[71] and Li *et al*[72] found, independently, the existence of multiple configurations for the pair of Ce^{3+} around the vacancy on CeO_2 111, all within few tenths of eV. The most stable solutions were found with both the Ce^{3+} in the second cationic shell from the vacancy. These results were confirmed with both DFT+U and the hybrid HSE06, even if the latter predicts more endothermic energies of formation, closer to the experimental results.

Later on this picture was confirmed by STM measurements[64], showing that at least one of the Ce^{3+} associated with the Vo is not in next neighbour position.

The existence of multiple quasi-degenerate configurations for the Ce^{3+} ions is justified by the non-participation of the 4*f* orbitals to chemical bond and to the open fluorite structure of the ceria, able to relax for optimizing the coordination environment. Preferential reduction sites exhibit longer Ce-O average length. If the Vo is formed on the ideal bulk or surface structures, the electrons localize always on two Ce first neighbour to the V_O, being the configuration closest to the local minima (if no bias are applied in the Self-consistent-field procedure). Other configurations are obtainable by manually elongating the Ce-O bonds of the specific reduction sites. Alternatively, the structures of the specific configurations can be pre-optimized with a force-field method able to differentiate Ce^{3+} and Ce^{4+}. These and other approaches are nominated by Cormack and coworkers[73] but almost no other theoretical works explains how to obtain different Ce^{3+} configurations.

The existence of many solutions closes in energy for both the position of Ce^{3+}, for the 4*f* sub-shell occupation and for the local structure makes the SCF difficult to converge to a minimum, so that finding the global minimum in presence of more than 2 Ce^{3+} is unfeasible in most cases.

1.5 Doped ceria

One way to modify the reactivity of ceria is to insert a dopant: many works have shown that the substitutional doping of Ce with transition, noble and rare earth metals decreases the formation energies of the V_O, increasing the OSC activity[74,75,76].

Interesting for applications in SOFCs is the enhancing of the ionic conductivity by doping with Gd and Pr, which allow a lower working temperature of the device.

Two kinds of effects are involved in the lowering the E_{fv} by doping: local effects as structure relaxation and alteration of the chemical bond Me-O, and global effects related to the electronic structure of the material[75].

A typical local effect is observed by doping with an isovalent element with, as Zr. Zr^{4+} is smaller than Ce^{4+} and prefers the coordination number 6 instead that 8: it distorts the local structure of CeO_2 due to the shorter Zr-O bonds. The E_{fv} decreases near the Zr, driven by the structure relaxation alone, being Zr non-reducible.

In the case of a non-reducible dopant with lower valence as La(+3), an O 2*p* hole state appears in the valence band: as the vacancy forms the hole state is filled before the 4*f*, being lower in energy, and only a Ce^{3+} forms. Alternatively, a localized O 2*p* hole can form on one of the O neighbours to the dopant: formally, this is an $*O^-$ radical ion, easier to remove from the lattice than O 2*p* due to the smaller electrostatic interactions with respect to O^{2-}.

1.6 Ceria as support for metals

One of the most important properties of ceria is its capability to stabilize supported metal particles, hindering their coalescence (Strong metal oxide support interaction).[77]

This allows a finer dispersion of the metal powders, increasing the total active surface of the catalyst.

After deposition, metal particles with a low work function are easily oxidized by the ceria support from a direct electron transfer from the cluster to the closest Ce^{4+} ions, then reduced to Ce^{3+}. This process alters the electronic properties at the interphase, potentially enhancing the reactivity of the system even with scarcely active metals. For instance, Cu, which has a low activity towards H_2 oxidation, when supported on ceria contributes to catalyse the reaction of oxidation of H_2 and the following process of formation of water.

This has been shown with PBE+U calculations on the model catalyst $Cu_{10}/CeO_2(111)$: indeed, the dissociation of H_2 occurs with lower barriers at the cluster-oxide interphase (three-phase-boundary) than on the ceria surface[4]. Moreover, the HO recombination to form water is facilitated by presence of the metal particle.

The deposition of a metal cluster affects also the E_{fv}: for most oxides, reducible and non-reducible, DFT calculations show lower energy of formations both at interfacial sites (with O involved in the bonding with the metal) and at peripherical sites on the oxide surface. Ceria seems to be an exception, being the V_O formation suppressed at the interface, and almost unchanged at peripherical sites, according calculations on the surface 111. This behaviour find explanation by considering the reduction of the surface upon the metal deposition: a further reduction by forming the Vo is hindered. However, the formation of the Vo at the interphase is affected both by electronic factors and by the structural relaxation of the defect site, on which contribute the flexibility of the metal cluster[78].

1.7 Aim of the thesis

The scope of this thesis is to present an affordable computational protocol to model ceria-based materials, relying on the use of density functional theory at the hybrid functional level, within a GTO implementation, useful to improve the theoretical description of catalytic processes in several technological applications.

In this introductory chapter the applications, the main properties and the body of the theoretical investigation concerning the cerium oxides have been presented.

In chapter 2 the theoretical background of the quantum mechanical methods used in the thesis is reported. In chapter 3 is presented the assessment of the computational protocol to investigate the

cerium oxides. After a careful choice of the GTO basis set, several hybrid functionals have been tested on the ground state properties of the cerium oxides CeO_2 and Ce_2O_3, and on the test model of the oxygen vacancy on the surface 111 of CeO_2. Once appointed the computational protocol to described mixed valence CeO_x systems, the investigation is extended to study cases relevant for catalysis.

Chapter 4 is focused on Ag and Cu modified CeO_2 (111): the effects of the dopant atoms on the electronic structures and on the reducibility of the systems are investigated.

In chapter 5 an ideal metal supported oxide system, Ag_{10}/CeO_2 (111), is considered: first it is examined the formation of the interphase Ag-CeO_2 and the role of the metal particle on the reducibility. Then, the reactivity of this system and of the ideal ceria surface towards the process of oxidation of H_2 and of water formation are compared.

In chapter 6 it is presented the process of O_2 activation at oxide surfaces: the reactivity is compared for the Ag_{10}/CeO_2 (111) and CeO_2(111) model systems and for an analogous Ag_{10}-TiO_2(110) and TiO_2 (110) system. Finally, conclusions are drawn in chapter 7.

1.8 References

1. Gerward, L. & Olsen, J. S. Powder diffraction analysis of cerium dioxide at high pressure. *Powder Diffr.* **8**, 127–129 (1993).
2. Castleton, C. W. M., Kullgren, J. & Hermansson, K. Tuning LDA+U for electron localization and structure at oxygen vacancies in ceria. *J. Chem. Phys.* **127**, 244704 (2007).
3. Gerward, L. *et al.* Bulk modulus of CeO_2 and PrO_2—An experimental and theoretical study. *J. Alloys Compd.* **400**, 56–61 (2005).
4. Duclos, S. J., Vohra, Y. K., Ruoff, A. L., Jayaraman, A. & Espinosa, G. P. High-pressure x-ray diffraction study of CeO_2 to 70 GPa and pressure-induced phase transformation from the fluorite structure. *Phys. Rev. B* **38**, 7755 (1988).
5. Mochizuki, S. Infrared optical properties of cerium dioxide. *Phys. Status Solidi B* **114**, 189–199 (1982).
6. Santha, N. I. *et al.* Effect of Doping on the Dielectric Properties of Cerium Oxide in the Microwave and Far-Infrared Frequency Range. *J. Am. Ceram. Soc.* **87**, 1233–1237 (2004).
7. Bärnighausen, H. & Schiller, G. The crystal structure of A-Ce_2O_3. *J. Common Met.* **110**, 385–390 (1985).
8. Lipp, M. J. *et al.* Comparison of the high-pressure behavior of the cerium oxides Ce_2O_3 and CeO_2. *Phys. Rev. B* **93**, (2016).

9. Avisar, D. & Livneh, T. The Raman-scattering of A-type Ce. *Vib. Spectrosc.* **86**, 14–16 (2016).
10. Vayssilov, G. N., Mihaylov, M., Petkov, P. St., Hadjiivanov, K. I. & Neyman, K. M. Reassignment of the Vibrational Spectra of Carbonates, Formates, and Related Surface Species on Ceria: A Combined Density Functional and Infrared Spectroscopy Investigation. *J. Phys. Chem. C* **115**, 23435–23454 (2011).
11. Pinto, H., Mintz, M. H., Melamud, M. & Shaked, H. Neutron diffraction study of Ce_2O_3. *Phys. Lett. A* **88**, 81–83 (1982).
12. Prokofiev, A. V., Shelykh, A. I. & Melekh, B. T. Periodicity in the band gap variation of Ln_2X_3 (X= O, S, Se) in the lanthanide series. *J. Alloys Compd.* **242**, 41–44 (1996).
13. Zinkevich, M., Djurovic, D. & Aldinger, F. Thermodynamic modelling of the cerium–oxygen system. *Solid State Ion.* **177**, 989–1001 (2006).
14. Kummer, J. T. Catalysts for automobile emission control. *Prog. Energy Combust. Sci.* **6**, 177–199 (1980).
15. Lööf, P., Kasemo, B. & Keck, K.-E. Oxygen storage capacity of noble metal car exhaust catalysts containing nickel and cerium. *J. Catal.* **118**, 339–348 (1989).
16. Yao, H. C. & Yao, Y. F. Y. Ceria in automotive exhaust catalysts: I. Oxygen storage. *J. Catal.* **86**, 254–265 (1984).
17. Bueno-López, A. Diesel soot combustion ceria catalysts. *Appl. Catal. B Environ.* **146**, 1–11 (2014).
18. Liu, S., Wu, X., Weng, D. & Ran, R. Ceria-based catalysts for soot oxidation: a review. *J. Rare Earths* **33**, 567–590 (2015).
19. Hansen, U. R. & Mogensen, G. Physical Propertiesof Mixed Conductor Solid Oxide FuelCell Anodesof Doped CeO_2. *J Electrochem Soc* **141**, 7 (1994).
20. Marina, O. A solid oxide fuel cell with a gadolinia-doped ceria anode: preparation and performance. *Solid State Ion.* **123**, 199–208 (1999).
21. Inaba, H. Ceria-based solid electrolytes. *Solid State Ion.* **83**, 1–16 (1996).
22. Tuller, H. Ionic conduction in nanocrystalline materials. *Solid State Ion.* **131**, 143–157 (2000).
23. Park, S., Vohs, J. M. & Gorte, R. J. Direct oxidation of hydrocarbons in a solid-oxide fuel cell. *Nature* **404**, 265–267 (2000).
24. Kurokawa, H., Sholklapper, T. Z., Jacobson, C. P., De Jonghe, L. C. & Visco, S. J. Ceria Nanocoating for Sulfur Tolerant Ni-Based Anodes of Solid Oxide Fuel Cells. *Electrochem. Solid-State Lett.* **10**, B135 (2007).

25. Montini, T., Melchionna, M., Monai, M. & Fornasiero, P. Fundamentals and Catalytic Applications of CeO_2 -Based Materials. *Chem. Rev.* **116**, 5987–6041 (2016).
26. Xu, H. & Hou, X. Synergistic effect of CeO_2 modified Pt/C electrocatalysts on the performance of PEM fuel cells. *Int. J. Hydrog. Energy* **32**, 4397–4401 (2007).
27. Lei, M. *et al.* Self-assembled mesoporous carbon sensitized with ceria nanoparticles as durable catalyst support for PEM fuel cell. *Int. J. Hydrog. Energy* **38**, 205–211 (2013).
28. Bambagioni, V. *et al.* Energy Efficiency Enhancement of Ethanol Electrooxidation on Pd-CeO_2/C in Passive and Active Polymer Electrolyte-Membrane Fuel Cells. *ChemSusChem* **5**, 1266–1273 (2012).
29. Bion, N., Epron, F., Moreno, M., Mariño, F. & Duprez, D. Preferential Oxidation of Carbon Monoxide in the Presence of Hydrogen (PROX) over Noble Metals and Transition Metal Oxides: Advantages and Drawbacks. *Top. Catal.* **51**, 76–88 (2008).
30. Wang, X. & Gorte, R. J. Steam reforming of n-butane on Pd/ceria. *Catal. Lett.* **73**, 15–19 (2001).
31. Ratnasamy, C. & Wagner, J. P. Water Gas Shift Catalysis. *Catal. Rev.* **51**, 325–440 (2009).
32. Li, H. *et al.* Hierarchical Organization and Catalytic Activity of High-Surface-Area Mesoporous Ceria Microspheres Prepared Via Hydrothermal Routes. *ACS Appl. Mater. Interfaces* **2**, 838–846 (2010).
33. Dai, Q., Wang, X. & Lu, G. Low-temperature catalytic combustion of trichloroethylene over cerium oxide and catalyst deactivation. *Appl. Catal. B Environ.* **81**, 192–202 (2008).
34. Moser, M. *et al.* Supported CeO_2 catalysts in technical form for sustainable chlorine production. *Appl. Catal. B Environ.* **132–133**, 123–131 (2013).
35. Chueh, W. C. *et al.* High-Flux Solar-Driven Thermochemical Dissociation of CO_2 and H_2O Using Nonstoichiometric Ceria. *Science* **330**, 1797–1801 (2010).
36. Xu, C. & Qu, X. Cerium oxide nanoparticle: a remarkably versatile rare earth nanomaterial for biological applications. *NPG Asia Mater.* **6**, e90–e90 (2014).
37. Schubert, D., Dargusch, R., Raitano, J. & Chan, S.-W. Cerium and yttrium oxide nanoparticles are neuroprotective. *Biochem. Biophys. Res. Commun.* **342**, 86–91 (2006).
38. Paier, J., Penschke, C. & Sauer, J. Oxygen Defects and Surface Chemistry of Ceria: Quantum Chemical Studies Compared to Experiment. *Chem. Rev.* **113**, 3949–3985 (2013).
39. Angelow, B. M. Energies and electronic energy levels of lanthanide dioxides. *J. Phys. C Solid State Phys.* **14**, L757–L759 (1981).
40. Zhou, Y., Nakashima, M. & White, J. M. Interaction of platinum with ceria and silica. *J. Phys. Chem.* **92**, 812–818 (1988).

41. Wuilloud, E., Delley, B., Schneider, W.-D. & Baer, Y. Spectroscopic Evidence for Localized and Extended f -Symmetry States in CeO_2. *Phys. Rev. Lett.* **53**, 202–205 (1984).
42. Koelling, D. D., Boring, A. M. & Wood, J. H. The electronic structure of CeO_2 and PrO_2. *Solid State Commun.* **47**, 227–232 (1983).
43. Hill, S. E. & Catlow, C. R. A. A Hartree-Fock periodic study of bulk ceria. *J. Phys. Chem. Solids* **54**, 411–419 (1993).
44. Skorodumova, N. V. *et al.* Electronic, bonding, and optical properties of CeO_2 and Ce_2O_3 from first principles. *Phys. Rev. B* **64**, (2001).
45. Skorodumova, N. V., Simak, S. I., Lundqvist, B. I., Abrikosov, I. A. & Johansson, B. Quantum Origin of the Oxygen Storage Capability of Ceria. *Phys. Rev. Lett.* **89**, (2002).
46. Perdew, J. P. & Zunger, A. Self-interaction correction to density-functional approximations for many-electron systems. *Phys. Rev. B* **23**, 5048–5079 (1981).
47. Petit, L., Svane, A., Szotek, Z. & Temmerman, W. M. First-principles study of rare-earth oxides. *Phys. Rev. B* **72**, (2005).
48. Anisimov, V. I., Aryasetiawan, F. & Lichtenstein, A. I. First-principles calculations of the electronic structure and spectra of strongly correlated systems: the LDA+ U method. *J. Phys. Condens. Matter* **9**, 767–808 (1997).
49. Liechtenstein, A. I., Anisimov, V. I. & Zaanen, J. Density-functional theory and strong interactions: Orbital ordering in Mott-Hubbard insulators. *Phys. Rev. B* **52**, R5467–R5470 (1995).
50. Fabris, S., de Gironcoli, S. & Baroni, S. Electron localization in pure and defective ceria by a unified LDA+ U approach. *ArXiv Prepr. Cond-Mat0312601* (2003).
51. Fabris, S., de Gironcoli, S., Baroni, S., Vicario, G. & Balducci, G. Taming multiple valency with density functionals: A case study of defective ceria. *Phys. Rev. B* **71**, (2005).
52. Nolan, M., Grigoleit, S., Sayle, D. C., Parker, S. C. & Watson, G. W. Density functional theory studies of the structure and electronic structure of pure and defective low index surfaces of ceria. *Surf. Sci.* **576**, 217–229 (2005).
53. Castleton, C. W. M., Lee, A. L., Kullgren, J. & Hermansson, K. Description of polarons in ceria using Density Functional Theory. *J. Phys. Conf. Ser.* **526**, 012002 (2014).
54. Castleton, C. W. M., Lee, A. & Kullgren, J. Benchmarking Density Functional Theory Functionals for Polarons in Oxides: Properties of CeO_2. *J. Phys. Chem. C* **123**, 5164–5175 (2019).
55. Janesko, B. G. & Scuseria, G. E. Hartree–Fock orbitals significantly improve the reaction barrier heights predicted by semilocal density functionals. *J. Chem. Phys.* **128**, 244112 (2008).

56. Zhao, Y., González-García, N. & Truhlar, D. G. Benchmark Database of Barrier Heights for Heavy Atom Transfer, Nucleophilic Substitution, Association, and Unimolecular Reactions and Its Use to Test Theoretical Methods. *J. Phys. Chem. A* **109**, 2012–2018 (2005).

57. Paier, J. Hybrid Density Functionals Applied to Complex Solid Catalysts: Successes, Limitations, and Prospects. *Catal. Lett.* **146**, 861–885 (2016).

58. Hay, P. J., Martin, R. L., Uddin, J. & Scuseria, G. E. Theoretical study of CeO_2 and Ce_2O_3 using a screened hybrid density functional. *J. Chem. Phys.* **125**, 034712 (2006).

59. Da Silva, J. L. F., Ganduglia-Pirovano, M. V., Sauer, J., Bayer, V. & Kresse, G. Hybrid functionals applied to rare-earth oxides: The example of ceria. *Phys. Rev. B* **75**, (2007).

60. Kullgren, J., Castleton, C. W. M., Müller, C., Ramo, D. M. & Hermansson, K. B3LYP calculations of cerium oxides. *J. Chem. Phys.* **132**, 054110 (2010).

61. Graciani, J. *et al.* Comparative Study on the Performance of Hybrid DFT Functionals in Highly Correlated Oxides: The Case of CeO_2 and Ce_2O_3. *J. Chem. Theory Comput.* **7**, 56–65 (2011).

62. Pacchioni, G. Ab initio theory of point defects in oxide materials: structure, properties, chemical reactivity. *Solid State Sci.* **2**, 161–179 (2000).

63. Ganduglia-Pirovano, M. V. Oxygen Defects at Reducible Oxide Surfaces: The Example of Ceria and Vanadia. in *Defects at Oxide Surfaces* (eds. Jupille, J. & Thornton, G.) vol. 58 149–190 (Springer International Publishing, 2015).

64. Jerratsch, J.-F. *et al.* Electron Localization in Defective Ceria Films: A Study with Scanning-Tunneling Microscopy and Density-Functional Theory. *Phys. Rev. Lett.* **106**, (2011).

65. Gennard, S., Corà, F. & Catlow, C. R. A. Comparison of the Bulk and Surface Properties of Ceria and Zirconia by ab Initio Investigations. *J. Phys. Chem. B* **103**, 10158–10170 (1999).

66. Skorodumova, N. V., Baudin, M. & Hermansson, K. Surface properties of CeO_2 from first principles. *Phys. Rev. B* **69**, (2004).

67. Yang, Z., Woo, T. K., Baudin, M. & Hermansson, K. Atomic and electronic structure of unreduced and reduced CeO_2 surfaces: A first-principles study. *J. Chem. Phys.* **120**, 7741–7749 (2004).

68. Fabris, S., Vicario, G., Balducci, G., de Gironcoli, S. & Baroni, S. Electronic and Atomistic Structures of Clean and Reduced Ceria Surfaces. *J. Phys. Chem. B* **109**, 22860–22867 (2005).

69. Burow, A. M., Sierka, M., Döbler, J. & Sauer, J. Point defects in CaF_2 and CeO_2 investigated by the periodic electrostatic embedded cluster method. *J. Chem. Phys.* **130**, 174710 (2009).

70. Herschend, B., Baudin, M. & Hermansson, K. Electronic structure of the CeO_2(110) surface oxygen vacancy. *Surf. Sci.* **599**, 173–186 (2005).

71. Ganduglia-Pirovano, M. V., Da Silva, J. L. F. & Sauer, J. Density-Functional Calculations of the Structure of Near-Surface Oxygen Vacancies and Electron Localization on CeO_2 (111). *Phys. Rev. Lett.* **102**, (2009).

72. Li, H.-Y. *et al.* Multiple configurations of the two excess 4 f electrons on defective CeO_2 (111) : Origin and implications. *Phys. Rev. B* **79**, (2009).

73. Wang, B., Xi, X. & Cormack, A. N. Chemical Strain and Point Defect Configurations in Reduced Ceria. *Chem. Mater.* **26**, 3687–3692 (2014).

74. Gupta, A., Waghmare, U. V. & Hegde, M. S. Correlation of Oxygen Storage Capacity and Structural Distortion in Transition-Metal-, Noble-Metal-, and Rare-Earth-Ion-Substituted CeO_2 from First Principles Calculation. *Chem. Mater.* **22**, 5184–5198 (2010).

75. Hu, Z. & Metiu, H. Effect of Dopants on the Energy of Oxygen-Vacancy Formation at the Surface of Ceria: Local or Global? *J. Phys. Chem. C* **115**, 17898–17909 (2011).

76. Nolan, M. Enhanced oxygen vacancy formation in ceria (111) and (110) surfaces doped with divalent cations. *J. Mater. Chem.* **21**, 9160 (2011).

77. Farmer, J. A. & Campbell, C. T. Ceria Maintains Smaller Metal Catalyst Particles by Strong Metal-Support Bonding. *Science* **329**, 933–936 (2010).

78. Ruiz Puigdollers, A., Schlexer, P., Tosoni, S. & Pacchioni, G. Increasing Oxide Reducibility: The Role of Metal/Oxide Interfaces in the Formation of Oxygen Vacancies. *ACS Catal.* **7**, 6493–6513 (2017).

79. Cococcioni, M. & de Gironcoli, S. Linear response approach to the calculation of the effective interaction parameters in the LDA + U method. *Physical Review B* **71**, (2005).

Chapter 2: Theoretical background

2.1 Introduction

The continuous improvement in computational power makes theoretical methods and simulations an ever-growing resource in all areas of the research.

In material sciences, molecular simulations come often before experiments, primarily due to the necessity to screen among a large number of experimental variables, or due to the infeasibility to reach extreme conditions in the laboratory.

Different computational methods exist to deal with phenomena occurring at different space and time scales, ranging from the macroscopic realm, perceptible with the human senses (the continuum), to the sub-atomic realm, understandable only with quantum mechanics tools.

To understand the systems investigated, it is necessary to appreciate the properties arising from their electronic structure such as the defect chemistry, the magnetic ordering, the metal-metal oxide electron transfer. Among the quantum mechanical methods, the Density Functional Theory (DFT) is the most effective theoretical tools to describe the electronic structure of materials, and the literature reports many successful results of DFT studies on the system of interest here.

In this chapter is presented a brief overview on the quantum mechanics methods, a more comprehensive description of the Hartree-Fock (HF), and the approximations underling the DFT, in order to understand the limitations of the methods, with a focus on the applications on materials.

2.2 Quantum chemical calculations

The description of a many-electron system is quite a formidable task for theoretical chemistry.

In principle, to obtain the wavefunction, the mathematical object which contains all the information on the system, is necessary to solve the time dependent Schrödinger equation in a non-relativistic framework and if the phenomena under investigation are time-independent the SE can be written as follow:

$$\hat{H}\Psi(\mathbf{r}_i,\mathbf{R}_a)=E\Psi(\mathbf{r}_i,\mathbf{R}_a) \tag{2.1}$$

The wavefunction Ψ depends on the spatial coordinates **r** of the i-th electron and **R** of the a-th nucleus. $\hat{H}$ is the Hamiltonian operator of the system of N electron and M nuclei:

$$\hat{H}(\mathbf{r},\mathbf{R})=\hat{T}_n(\mathbf{R})+\hat{T}_e(\mathbf{r})+\hat{V}_{en}(\mathbf{r},\mathbf{R})+\hat{V}_{ee}(\mathbf{r})+\hat{V}_{nn}(\mathbf{R}) \tag{2.2}$$

$\hat{T}_n(\mathbf{R})$ and $\hat{T}_e(\mathbf{r})$ are the kinetic energy operators of nuclei and electrons, respectively; $\hat{V}_{en}(\mathbf{r},\mathbf{R})$ is the electron-nucleus attractive potential, $\hat{V}_{ee}(\mathbf{r})$ the electron-electron repulsive potential and $\hat{V}_{nn}(\mathbf{R})$ is the nucleus-nucleus repulsive potential.

The explicit Hamiltonian for a system of M nuclei and N electron, adopting the atomic units, is then:

$$\hat{H} = -\frac{1}{2}\sum_{i}^{N}\nabla_i^2 - \frac{1}{2}\sum_{A}^{M}\frac{\nabla_A^2}{M_A} - \sum_{i}^{N}\sum_{A}^{M}\frac{Z_A}{r_{iA}} + \sum_{i}^{N-1}\sum_{i<j}^{N}\frac{1}{r_{ij}} + \sum_{A}^{M-1}\sum_{B<A}^{M}\frac{Z_A Z_B}{R_{AB}} \qquad (2.3)$$

M_A, R_{AB}, Z_A, r_{iA}, r_{ij} are respectively the nuclei A mass, the distance between nuclei A and B, the nuclear charge, the electron-nucleus distance and the interelectronic distance.

By applying the Born-Oppenheimer approximation[1], which validity holds for most ground-state problems in quantum chemistry, the nuclear motion is decoupled by the electronic one.

The approximation is grounded on the large difference in mass between nuclei and electrons, which makes the electronic cloud follows the nuclear motion adiabatically. Hence, the total energy of the systems is separable into an electronic and a nuclear term.

$$\hat{H} = \hat{H}_{el} + \hat{H}_{nucl} \qquad (2.4)$$

$$\hat{H}_{el} = -\sum_{i}\frac{1}{2}\nabla_i^2 - \sum_{i}\sum_{A}\frac{Z_A}{r_{iA}} + \sum_{i}\sum_{i<j}\frac{1}{r_{ij}} \qquad (2.5)$$

$$\hat{H}_{nucl} = -\sum_{A}\frac{1}{2}\nabla_A^2 + \sum_{A}\sum_{A<B}\frac{Z_A Z_B}{R_{AB}} \qquad (2.6)$$

This assumption allows the separation of the molecular wavefunction $\Psi(\mathbf{r}_i,\mathbf{R}_A)$ into the product $\varphi((\mathbf{r}_i;\mathbf{R}_A)\chi(\mathbf{R}_A)$, where $\varphi((\mathbf{r}_i;\mathbf{R}_A)$ is the electronic wavefunction and $\chi(\mathbf{R}_A)$ is the nuclear wavefunction. The former depends by the nuclear coordinates only parametrically:

$$\hat{H}_{el}\,\varphi(\mathbf{r}_i,\mathbf{R}_A) = E_{el}\varphi(\mathbf{r}_i,\mathbf{R}_A) \qquad (2.7)$$

The Eq. 7 is not solvable exactly for systems with more than 1 electron, therefore further

approximations have been developed to tackle the problem.
For static calculations, the electronic problem is solved for different nuclear configurations, allowing to explore the potential energy surface (PES) of the system. Stationary points, the most interesting configurations of the PES, can be identified with suitable algorithms.
The next sections will deal with the approximations adopted to solve the electronic problem. In all the dissertation the non-relativistic formulation and the Born-Oppenheimer approximation are considered.

2.3 The Hartree-Fock approximation

The first attempt to simplify the many-body problem was to assume each particle independent and interacting only with the average potential generated by the others N-1 particles. This is often called the *mean-field approximation* or the *independent particles approximation* and was introduced by Douglas Hartree in the 1928, only one year after the discovery of the SE. Within this approximation, the electron-electron repulsive potential in the Hamiltonian is replaced by the interaction electron-mean field (Fock). The Hamiltonian is hence simplified, it becomes the sum of independent terms, therefore the wavefunction is simplified to a product of monoelectronic functions, the spin-orbitals $\phi(\mathbf{r};\boldsymbol{\omega})$:

$$\phi(\mathbf{r};\boldsymbol{\omega})=\psi(\mathbf{r})\sigma(\boldsymbol{\omega}) \tag{2.8}$$

where **r** and **ω** are the spatial and spin variables, respectively. The product of the N spin-orbitals is then called Hartree product:

$$\varphi(\mathbf{x}_1, \mathbf{x}_2, \dots, \mathbf{x}_N) = \phi_1(\mathbf{x}_1)\phi_2(\mathbf{x}_2) \dots \phi_N(\mathbf{x}_N) \tag{2.9}$$

The Hamiltonian became the sum of monoelectronic operators $\hat{h}(I)$, and the SE of the N electrons system is simplified as a system of N monoelectronic equations.
The total energy is given by the sum of the one- ϕ energies.
Despite the first success of the method, the Hartree product does not respect one fundamental property: the wavefunction of a system of electrons (fermions) should be antisymmetric with respect to the operation of exchange of coordinates of a couple of particles.
The model of Hartree was then refined by Slater and Fock into the Hartree-Fock model:
by reformulating the Hartree product in the form of a determinant of Slater (Ψ_{SD}), the anti-symmetry is reintroduced, and as consequence, the Pauli exclusion principle is respected.

$$\Psi_{\mathrm{SD}}(\mathbf{x}_1, \mathbf{x}_2, \dots, \mathbf{x}_{\mathrm{N}}) = \frac{1}{\sqrt{\mathrm{N!}}} \begin{vmatrix} \phi_1(\mathbf{x}_1) & \phi_1(\mathbf{x}_2) & \cdots & \phi_1(\mathbf{x}_{\mathrm{N}}) \\ \phi_2(\mathbf{x}_1) & \phi_2(\mathbf{x}_2) & & \phi_2(\mathbf{x}_{\mathrm{N}}) \\ \vdots & \vdots & \ddots & \vdots \\ \phi_{\mathrm{N}}(\mathbf{x}_1) & \phi_{\mathrm{N}}(\mathbf{x}_2) & \cdots & \phi_{\mathrm{N}}(\mathbf{x}_{\mathrm{N}}) \end{vmatrix} \tag{2.10}$$

The term $\frac{1}{\sqrt{N!}}$ is the normalization factor. In the Slater determinant, the N electrons occupy N spin-orbitals without assigning explicitly one electron to one-orbital, respecting the indistinguishability principle of identical particles.

Starting from this formulation, the best approximated wavefunction of the N electron system is searched by minimizing the energy of the Slater's determinant. This is possible by exploiting the *Variational Principle*, which states that to any approximated wavefunction of the ground-state correspond an expectation value $\tilde{E}$ larger or, at best, equal to the exact ground-state energy E_0.

$$\tilde{E} = \int \Psi_{HF}^{*} \hat{H} \Psi_{HF} d\boldsymbol{x} \quad \rightarrow \quad \tilde{E} \geq \int \Psi_0^{*} \hat{H} \Psi_0 d\boldsymbol{x} = E_0 \tag{2.11}$$

The energy is minimized by varying the spin-orbitals, under the orthonormality constraint, looking for the spin-orbitals which make the energy stationary.

To keep the constraint of orthonormality of the spin-orbitals it is adopted the formalism of the Lagrange multipliers, that will not be shown in this dissertation. In the following it is presented the result of the development of the equations, that can be found in many reference books as Szabo and Ostlund[2] or Leach[3].

The expression for the Hartree-Fock energy became:

$$\tilde{E} = E_{\mathrm{HF}} = \sum_{a} \int \phi_{\mathrm{a}}^{*}(1) \hat{\mathrm{h}} \phi_{\mathrm{a}}(1)\, \mathrm{dx}_1 \tag{2.12}$$

$$- \sum_{ab} \int \phi_{\mathrm{a}}(1) \phi_{\mathrm{b}}^{*}(1) \frac{1}{\mathrm{r}_{12}} \phi_{\mathrm{b}}(2) \phi_{\mathrm{a}}^{*}(2)\, \mathrm{dx}_1\, \mathrm{dx}_2 + \frac{1}{2} \sum_{ab} \int \phi_{\mathrm{a}}(1) \phi_{\mathrm{a}}^{*}(1) \frac{1}{\mathrm{r}_{12}} \phi_{\mathrm{b}}(2) \phi_{\mathrm{b}}^{*}(2)\, \mathrm{dx}_1\, \mathrm{dx}_2$$

The first term of the eq. 12 is the one-electron energy term, it contains the kinetic energy and the attractive potential electron-nuclei.

The other two terms in eq. 12 involve both two electrons and are respectively the Coulomb term and the Exchange term. The latter arise as consequence of the anti-symmetry of the Slater determinant.

The Coulomb term contains the classical electrostatic interaction between two electrons in two distinct orbitals.

The Coulomb operator $\hat{J}_b$ is then defined as:

$$\hat{J}_b = \int |\chi_b(2)|^2 \frac{1}{r_{12}} dx_2 \tag{2.13}$$

The Exchange term has not a classical interpretation, but it can be expressed in the form of operator $\hat{K}_b$ by its effects on the spin-orbitals:

$$\hat{K}_b(1)\phi_a(1) = \left[\int \phi_b^*(2) \frac{1}{r_{12}} \phi_a(2) dx_2 \right] \phi_b(1) \tag{2.14}$$

From the eq.14 it is evident that the action of the operator $\hat{K}_b(1)$ is to exchange the spin-orbital ϕ_a with ϕ_b. Moreover, the effect of $K_b(1)$ on ϕ_a depends on the value of ϕ_a over all the space, therefore it is said that the exchange operator is a non-local operator.

The exchange term in the eq. 12 became:

$$\int \phi_a(1)\phi_b^*(1) \frac{1}{r_{12}} \phi(2)\phi_a^*(2)\ dx_1\, dx_2 = \int \phi_a^*(1)\hat{K}_b(1)\phi_a(1)\ dx_1 \tag{2.15}$$

Then, a one-electron HF equation can be written as an eigenvalue equation:

$$\left[\hat{h}(1) + \sum_{b \neq a} \hat{J}_b(1) - \sum_{b \neq a} \hat{K}_b(1)\right] \phi_a(1) = E_a \phi_a(1) \tag{2.16}$$

The Fock operator $\hat{f}(1)$is then defined as the sum of the one-electron Hamiltonian $\hat{h}(1)$ and an-effective potential given by the Coulomb and Exchange potentials:

$$\hat{f}(1) = \hat{h}(1) + \sum_b \left(\hat{J}_b(1) - \hat{K}_b(1)\right) \tag{2.17}$$

The final HF equation became:

$$\hat{f}(1)\phi_a(1) = E_a\phi_a(1) \tag{2.18}$$

For an N electrons system there are N coupled HF equations: even if they are expressed as eigenvalue problems, they are not solvable directly since the effective potential in the Fock operator depends on the spin-orbitals, solutions of the equations themselves. This problem is tackled by solving the HF equations iteratively in the so-called Self Consistent Field (SCF) procedure: at the first iteration a set of trial functions for each spin-orbital is adopted to compute the Fock operator, then the HF equations are solved generating a new set of spin-orbitals for the next iteration. Self-consistency is practically reached when the difference between the energies obtained from the last two iterations is below a predefined threshold.

Even if in principle any well-behaved function can be used to approximate the spin-orbitals, computational efficiency requires the adoption of manageable functional forms. The spin-orbitals are eigenfunctions of the Fock operator, hence they can be chosen to form a complete set orthonormal. In order to get computational efficiency, the spin-orbitals are approximated as a linear combination of opportunely chosen well-behaved functions, which form a basis set.

Here an important approximation is introduced: the *basis set truncation*.

This is one of the most critical approximations adopted in all *ab-initio* calculations, since independently on the level of theory adopted, the finite size of the basis set impacts on the quality of the computed wavefunction and the derived properties.

In the limit of an infinite basis set, the HF method could provide the best possible mono-determinantal representation of the ground-state wavefunction, and the associated energy is defined as the HF limit energy, which is an upper bound to the true energy of the system.

The difference between the HF limit energy and the true energy is called correlation energy. Due to the mean-field approximation each electron interacts with an averaged potential and not directly with each other, thus their motion is not correlated, and the inter-electronic repulsion is overestimated.

Even if the correlation energy account for a small fraction of the total electronic energy (about 1%), this is relevant to describe many chemical and physical phenomena correctly, and the fact that is neglected by the HF model is heavily reflected in its poor performance for thermochemical applications.

More accurate methods have been developed to improve the HF model by recovering the missing correlation, for instance, Configuration Interaction (CI), Møller-Plesset Perturbation Theory (MPn),

Coupled Cluster (CC), etc… Specifically, CI and CC in their full extension can provide the exact solution to the SE; thus they recover the full correlation, but they are affordable only for systems of very few electrons. Even the truncated forms of these methods are far too computationally demanding to investigate systems with dozens to hundreds of atoms (hundreds to thousands of electrons) as the ones of interest in the present dissertation. Therefore, these methods will not be further discussed, and the next section will deal instead with the alternative approach developed to efficiently tackle the many-particle problem and the missing correlation energy: the Density Functional Theory (DFT).

2.4 Density functional theory

Since the discovery of the SE it was obvious that the wavefunction was a very complex and obscure entity. At the same time, the electron density, a much more understandable object, was known to enclose properties derivable from the wavefunction.

The electron density $\rho(\mathbf{r})$ defines the probability to find any of the N electrons within a volume element $d\mathbf{r}$, while all the other N-1 electrons have arbitrary positions, and it is given by:

$$\rho(\boldsymbol{r}_1) = N \int \cdots \iint |\Psi(x_1, x_2, \dots, x_N)|^2 \, d\sigma_1 \, dx_2 \dots dx_N \tag{2.19}$$

Regardless of the number of electrons of the system, the electron density depends on only the three spatial coordinates, but it still contains all the necessary information to define the Hamiltonian of the system: the integral over all the space of the electron density $\rho(\mathbf{r})$ provides the number N of electrons in the system, the position $\mathbf{R_A}$ of the cusps of the electron density indicates the nuclear coordinates, while the slope of the cusps is related to the nuclear charges Z_A.

The first attempt to get a quantum theory of many electrons system based on the electronic density alone come from the works of Thomas and Fermi[4] (1927).

The Thomas-Fermi model tries to describe the Hamiltonian of the many electron system in terms of the electronic density: it adopted the uniform electron gas (UEG) as a model to compute the kinetic energy and used the classical expressions to compute the nuclear-electron attraction and the electron-electron repulsion. This was a very crude approximation, being the exchange interaction completely neglected, as well the Coulombic correlation, and the kinetic energy evaluated in a rather inaccurate way. A major drawback of the TF model was the failure to describe the formation of molecular bonds. Even with the improvement of the TF model with the inclusion of exchange[5] term for the UEG by Dirac, the method was still too inaccurate for quantitative predictions.

The breakthrough of the modern DFT starts with the alternative formalism introduced by the seminal work of Hohenberg and Kohn [6](1964).
In shorts, their two theorems states:

1-The external potential, and hence the ground state energy, is a unique functional of the electron density (for a non-degenerate ground state).
2-The ground state energy can be obtained variationally: the density which minimizes the total energy is the exact ground-state density.

These theorems prof that from the electron density are obtainable the same observables enclosed in the many-body wavefunction and that it is possible to refine the electron density following the same variational procedure used by HF calculations. Unfortunately, the theorems give no clues on which is the relation between electron density and energy, but the functional in general terms may be expressed as:

$$E[\rho] = \int \rho(\boldsymbol{r}) v(\boldsymbol{r})\, d\boldsymbol{r} + F_H k\big(\rho(\boldsymbol{r})\big) \tag{2.20}$$

Briefly after, Kohn and Sham developed a strategy to deal with the computation of the electron density[7]. They issued the failure of the TFD model primary to the inadequate description of the kinetic energy. In their formalism, the real system of N interacting electrons is replaced by a system of N non-interacting electrons, but subjected to the same external potential, hence the same ground-state density and energy. To compute the kinetic energy, the formulation based on orbitals was reintroduced, leading to the one-electron Kohn-Sham equation:

$$\left(-\frac{1}{2}\nabla^2 + v(\boldsymbol{r}) + \int \frac{\rho(\boldsymbol{r})}{|\boldsymbol{r}-\boldsymbol{r}'|} d\boldsymbol{r}' + v_{xc}(\boldsymbol{r})\right)\varphi_i = \varepsilon\varphi_i \tag{2.21}$$

From the left side of the eq. 21, the terms are: the kinetic energy of the non-interacting electrons, the external potential, the Coulombic repulsion (Hartree potential) and the exchange-correlation potential.
Similarly, to the spin-orbitals of the HF theory, here φ_i are the Kohn-Sham orbitals, while ε_i is the orbital energy.
The total density is then computed as the sum of the square modulus of the occupied orbitals:

$$\rho(r) = \sum_{l}^{N} |\varphi_i|^2 \tag{2.22}$$

The potential energy terms in the eq. 21 can be regrouped to form an effective potential v_{eff}:

$$v_{eff} = v(r) + \int \frac{\rho(r)}{|r - r'|} dr' + v_{xc}(r) \tag{2.23}$$

In this form the eq. 21 became:

$$(-\frac{1}{2}\nabla^2 + v_{eff}(r))\varphi_i = \varepsilon\varphi_i \tag{2.24}$$

This form resemble the HF equation saw before (eq. 17), and similarly it must be solved iteratively with a SCF procedure. In principle, if the exact form of v_{xc}would be known, the exact ground-state density and energy of the real system can be obtained, without approximations if not for the finite basis set. Unfortunately, we do not know yet the exact functional form of the exchange-correlation term, which contains other than the non-classical electron-electron interactions also the kinetic energy components neglected by the reference system of non-interacting particles.
Since the development of the Kohn-Sham method, many efforts have been spent to find more accurate approximations of the exchange-correlation functionals. In the next section the main milestones along the quest for the exact functional are shortly reported.

2.4 Exchange-Correlation Functionals

The Kohn-Sham approach enables us to tackle the many-electron problem for a system relying only on the density instead that on the wavefunction, trickery hidden all the difficulties inside the exchange-correlation (XC) term: the exact formulation of this term is still unknown and possibly it will never be known in a manageable and compact form.
In practice, to make DFT calculations, it is necessary to approximate the XC energy functional. Nowadays, hundreds of different approximations exist, with varying degree of complexity, and many others will come in the future. In order to orient among the hundreds of XC functionals, the categorization proposed by Perdew, the Jacob's ladder[8], come to help by dividing the different approximations according to their complexity in rungs of a ladder. The ladder connects the earth, where the HF approximation and inaccuracy rules, to the heaven, where it is found the exact XC

functional. Among these extremes, on the different rungs of the ladders, lie the different Density Functional Approximations (DFAs).

1st rung: Local Density Approximation (LDA). This is the first and simplest approximation to the XC, nevertheless it is the only one which could provide the exact solution in the ideal case of the UEG[7]. It is based on the concept that the XC energy depends only by the absolute value of the electron density point by point of the space.

$$E_{XC}[\rho] = \int d\boldsymbol{r}\rho(\boldsymbol{r})\upsilon_{xc}\rho(\boldsymbol{r}) \tag{2.25}$$

For the UEG, the exchange expression is known exactly (Dirac-Slater, S), while the correlation term is obtained by fitting the correlation energy of the UEG computed with high quality many-body simulations, as from the quantum Monte-Carlo method[9]. The XC correlation functional can then be formed by assembling two distinct exchange-correlation terms, as for the Dirac-Slater exchange and the Vosko-Wilk-Nusair (VWN) correlation, or it can be formed by a single term for both, as the von Barth-Hedin (VBH).
It must be noted that the separation has not physical meaning, but it simplifies the calculations.
The LDA works well for non-defective systems where the electron density changes smoothly in the space, for example for bulk metals, while for systems with a much inhomogeneous density the results are less reliable.

2nd rung: Generalized Gradient Approximation (GGA). The first sophistication of the LDA include into the XC functional the dependence by the gradient of the density, $\boldsymbol{\nabla}\rho(\mathbf{r})$.
At difference from LDA, for GGA and the successive DFAs, an ideal case for which the approximation provides exact results does not exist. This brings to two different ways to developed GGA functionals:

- an *ab-initio* approach, which include parameters to constrain the functional to reproduce some physical features of the electron density,
- a semi-empirical approach, which relies on the use of many parameters fitted to reproduce the experimental data.

The simplest expression for the XC energy can be written as:

$$E_{XC}[\rho] = \int d\boldsymbol{r}\rho(\boldsymbol{r})\upsilon_{xc}(\rho(\boldsymbol{r}), \nabla\rho(\boldsymbol{r})) \tag{2.26}$$

The exchange and correlation contributions are treated separately and then combined to form the total functional. The exchange term is taken from the LDA, but it includes an enhancement factor (F_X^{en}) and the reduced density gradient $s\big(\nabla\rho(\boldsymbol{r})\big)$, which improve the description of inhomogeneous systems:

$$E_X[\rho] = \int d\boldsymbol{r}\rho_X(\boldsymbol{r})\varepsilon_X(\rho(\boldsymbol{r}))F_X^{en}(s(\nabla\rho(\boldsymbol{r})) \tag{2.27}$$

$$s\big(\nabla\rho(\boldsymbol{r})\big) = \frac{|\nabla\rho_r(\boldsymbol{r})|}{\rho^{\frac{4}{3}}(\boldsymbol{r})} \tag{2.28}$$

The factor F_X^{en} is either parametrized on empirical data, as the noble gas exchange energy[10], or is expressed based on physical considerations. In similar way is derived the correlation functional.
The Perdew-Burke-Ernzerhof (PBE)[11] exchange and correlation functional is one of the most widely used GGA and belong to the *ab-initio* category, while the Becke88 (B88)[10] exchange and the Lee-Yang-Parr (LYP)[12] correlation functionals are among the most used of the semi-empirical class.

3rd rung: meta-GGA. After the GGA, the most natural development was to include the also higher derivatives of the density: meta-GGA include the Laplacian of the density $\nabla^2\rho(r)$. More typically, the modern meta-GGAs include the Laplacian of the occupied orbitals, which is the kinetic energy density τ. The general expression for the energy is then:

$$E_{XC}[\rho(r)] = \int d\boldsymbol{r}\rho(\boldsymbol{r})\varepsilon_{xc}(\rho(\boldsymbol{r}),\nabla\rho(\boldsymbol{r}),\tau\big(\rho(\boldsymbol{r})\big) \tag{2.29}$$

while the kinetic energy density is:

$$\tau(r) = \sum_i^{occ.}\frac{1}{2}|\nabla\varphi_i(\boldsymbol{r})|^2 \tag{2.30}$$

Some of the most successful members of this rung are TPSS, VSXC, PKZB and SCAN.

4th rung: hyper-GGA. Also called hybrid functionals, the DFAs in this rung contain a fraction of exchange computed as in the HF theory, hence considered exact exchange (EX). They classify in three main class, distinguished by the way the EX is included in the XC functional:

1. global hybrids (GHs): the EX is weighted in the functional by a constant parameter;
2. local hybrids (LHs): the weight of EX is function of the spatial positions a = a (**r**);
3. range-separated hybrids (RSHs): the Coulomb potential $1/r_{ij}$ is divided in a long-range (LR) and a short-range (SR) portion (eventually also a middle range component, MR). The EX is then weighted in different way in each portion.
   Being this DFA the most adopted in this thesis work, it will be discussed more in details in the next section.

A general expression for a GH functional is:

$$E_{XC}^{GH} = aE_{XC}^{HF} + (1-a)E_{XC}^{DFT} + E_{C}^{DFT} \tag{2.31}$$

The coefficient *a* regulates the admixture of exact exchange E_x^{HF} and functional exchange E_x^{DFT}, and it is constant along all the spatial domain.

The first attempts of hybrid functional included too much EX, and their performance on the atomization energies of the G2 data base of molecules were worse or comparable to the GGAs of the time[13]. Better results were achieved by Becke[14] with the inclusion of semiempirical coefficients to weight the different components, to form the functional B3PW91:

$$E_{XC}^{B3PW91} = aE_{XC}^{HF} + (1-a)E_{XC}^{LDA} + bE_{X}^{B88} + cE_{C}^{PW91} \tag{2.32}$$

While *a* weight the amount of EX, *b* and *c* regulate the different contributions to the exchange and correlation functional by mixing the B88 exchange functional and the PW91 correlation functional to the LDA exchange and correlation functional. The coefficients were fitted to best reproduce experimental observable as atomization energies, ionization energies and proton affinities from the G2 data base, with optimal values of 0.20, 0.72 and 0.81 for *a*, *b* and *c*, respectively. Successively, Stephen *et al*[15] proposed the probably most popular hybrid functional among chemists, B3LYP, very similar to the previous one, but with the PW91 correlation replaced by the LYP correlation functional, while the values of the parameters were unchanged with respect to the B3PW91 formulation. The reason for the great popularity of B3LYP is its high accuracy in describing many properties of interest of both main-group elements and transition metals compounds[13].

Later, Perdew and co-worker, in order to get rid from the dependence of empirical parameters, proposed the *ab-initio* approach to developed new functionals.
They showed, on the base of the adiabatic connection formula[16] and of perturbation theory arguments,[17,18] that the optimal fraction of EX is close to 25%.
On these results, the popular *ab-initio* PBE0 functional was then derived[19], with performance comparable with the other parametrized GHs.

In the range separated hybrids (RSHs), the amount of EX depends by the interelectronic distance. The Coulomb operator is divided in different ranges by mean of an error function, defined as:

$$\frac{1}{r_{12}} == \frac{erfc(\omega_{SR} r_{12})}{r_{12}} + \frac{1 - erfc(\omega_{SR} r_{12}) - erfc(\omega_{LR} r_{12})}{r_{12}} + \frac{erfc(\omega_{LR} r_{12})}{r_{12}} \qquad (2.33)$$

Where ω is the length scale of separation.
A general form for the RSHs is:

$$E_{XC}^{RSH} = \mathrm{E_{XC}^{DFA}} + \mathrm{c_{SR}}\left(\mathrm{E_{X,SR}^{HF}} - \mathrm{E_{X,SR}^{DFA}}\right) + \mathrm{c_{MR}}\left(\mathrm{E_{X,MR}^{HF}} - \mathrm{E_{X,MR}^{DFA}}\right) + \mathrm{c_{LR}}\left(\mathrm{E_{X,LR}^{HF}} - \mathrm{E_{X,LR}^{DFA}}\right) \qquad (2.34)$$

The coefficients c defines the fraction of EX employed at different ranges, while the ω parameters define the length scale of the separation for the different RSHs.

5th rung: Random-Phase Approximation-Double hybrids functionals. At the last rung, there are the functionals based on the *Random Phase Approximation*[20,21], also called double hybrids: in addition to the EX, also a fraction of correlation is computed according an exact scheme. This requires considering also the virtual orbitals in the computation. In particular, in the double hybrids functionals the exact correlation is computed with a post-HF like method which is then weighted in the energy functional similarly to the EX.
An example of double hybrid is the functional B2PLYP[22], which use 53% of the EX and 73% of the MP2 correlation, while the remaining parts are computed with the B88 exchange and the LYP correlation functionals.

The Jacob's ladder classification can be said to rank the DFA according the general performance of these methods, other than the functional complexity. Unfortunately, the performance of a specific XC functional may be system dependent, so in some cases lower ranked DFAs can perform better

than more sophisticated approximations. Even after decades of benchmarks of the different DFA on thousands of different compounds it is not possible to identify *a priori* the best approximation for the problem to investigate, although trends allow us to restrict the selection.

Nowadays, hybrid functionals are still the most adopted DFA for the study of molecular systems, since they outperform post-HF methods when dealing with medium size systems or larger. They provide more accurate reaction barriers and improve the description of the dissociation limits with compared to the lower approximations[23].

Even for the study of solids, the hybrid functionals are becoming the gold standard[24], they yield more accurate lattice parameters and band gaps, other than improve the calculation of the surface energies[23]. The main obstacle to the widespread use of functional hybrids for the study of solids is that they are slower, from 1 to 3 orders of magnitude, than the other semi-local functionals, depending on the system or calculation program used[23,25]. The reason of this disparity lies in the calculation of the exact exchange, which requires much more resources than the approximate exchange, but the difference in cost depends mainly on the representation used to expand for the basis set.

Gaussian type orbitals (GTOs) atom centred basis set are much more computationally efficient than plane wave basis set, even if the latter type is much simpler to handle[25].

2.6 Limits of DFT: self-interaction error and neglected dispersion forces.

In HF theory, the Coulombic self-interaction is completely taken out by the exchange interaction. In DFT, instead, the exchange is approximated and, consequently, the Coulombic self-interaction is not entirely cancelled, giving rise to the unphysical self-interaction error (SIE).

The most striking case is the error in the description of the infinitely stretched H_2^+ where the single electron of the system is equally shared by the two nuclei. All the standard DFAs give the same erroneous behaviour, the only way to get the proper physical description would be to include the full exact exchange of the HF theory. In many electrons systems, the SIE is more complex to describe, and it is commonly associated to the delocalization error[13,26].

These effects are more or less severe depending on the system and on the properties of interest, but there are specific cases where SIE is at the origin of an erratic description of the physics of the process investigated. The delocalization error affects the description of many processes as bond dissociations, transition state structures and strong correlated systems. Situations with elongated bonds are favoured, as in transition states, for which the associated barriers are underestimated. Materials as Mott insulators, characterized by highly localized *d* or *f* states in the valence band, are erroneously described as metallic, with the *d* or *f* states delocalized over the whole material.

Hybrid functionals, with the inclusion of a fraction of EX, mitigate the SIE. However, the precise fraction required to get the proper description is system dependent: some of the erratic behaviours necessitate the whole exact exchange to be corrected as for the H_2^+ case, while for others 20-25% is a fair amount.

The DFT +U methodology has been developed to deal with the case of the Mott-Insulator. This approach is based on the use of an on-situ orbital specific bias potential, called U, which enforce the localization, by penalizing solutions with partially occupied orbitals. Optimal U values for each material may be computed in an *ab-initio* fashion, but the more pragmatic approach is to fit the U value in order to reproduce a specific observable or to get the best compromise among many. Of the two methods, hybrid functionals are considered more accurate, even if problematic behaviours can be found when applied to metallic systems[24].

The DFT+U method is the most used to deal with SIE in materials since it has cost much more comparable with LDA and GGA than with hybrid functionals.

One other well-known limitation of standard DFT (and HF) is the neglecting of the dispersion interactions, which arise from the instantaneous fluctuation of the electrons density in separated parts of the system. This shortcoming is related to the non-correct evaluation of the electronic correlation, which has a non-local origin, but semi-local functionals approximate it with a local expression (with the exception of the double hybrids) while it is completely neglected by HF.

To overcome these limitations, several methods have been developed to include dispersive interactions in DFT. Three main strategies have been devised:

- Similarly to the classical mechanics-based methods, the dispersive interaction is described with a series of two or three-body interaction terms dependent on some dispersion coefficients C_n. These methods are then classified according to the origin of the C_n parameters. The dispersion energy computed is then added to the Kohn-Sham energy[27,28,29].
- An alternative approach is to include all the van der Walls interaction in the XC functional approximation to give a long-range non-local DFT[30]. The functionals of the Minnesota suits MOX[31, 32,33,34] include dispersion according to this scheme, even if the parameters are empirical, being fitted to reproduce properties of large sets of training systems.
- The last and most expensive approaches are based on the computation of the exact correlation by recurring to post-HF schemes involving the description of the virtual orbitals as for double hybrids functionals[35]. These methods are generally quite accurate, but the computational cost became similar to that of pure-post-HF schemes.

Dispersion interactions have been shown to little affect the structural properties of the oxides considered in this work, while energetics seems to improve when dispersion is accounted in a semiempirical fashion. Hence, we chose to adopt the cost-effective D3 method[28] to consider dispersion for the studies of the processes at the surfaces.

2.7 References

1. Born, M., Oppenheimer, J. R. & Physik, A. On the Quantum Theory of Molecules. 32.
2. Szabo, A. & Ostlund, N. S. *Modern Quantum Chemistry: Introduction to Advanced Electronic Structure Theory*. (Dover Publications, 2012).
3. Leach, A. R. & AR, L. *Molecular Modelling: Principles and Applications*. (Pearson Education, 2001).
4. Thomas, L. H. The calculation of atomic fields. *Math. Proc. Camb. Philos. Soc.* **23**, 542–548 (1927).
5. Dirac, P. a. M. Note on Exchange Phenomena in the Thomas Atom. *Math. Proc. Camb. Philos. Soc.* **26**, 376–385 (1930).
6. Hohenberg, P. & Kohn, W. Inhomogeneous Electron Gas. *Phys. Rev.* **136**, B864–B871 (1964).
7. Kohn, W. & Sham, L. J. Self-Consistent Equations Including Exchange and Correlation Effects. *Phys. Rev.* **140**, A1133–A1138 (1965).
8. Perdew, J. P. & Schmidt, K. Jacob's ladder of density functional approximations for the exchange-correlation energy. *AIP Conf. Proc.* **577**, 1–20 (2001).
9. Vosko, S. H., Wilk, L. & Nusair, M. Accurate spin-dependent electron liquid correlation energies for local spin density calculations: a critical analysis. *Can. J. Phys.* **58**, 1200–1211 (1980).
10. Becke, A. D. Density-functional exchange-energy approximation with correct asymptotic behavior. *Phys. Rev. A* **38**, 3098–3100 (1988).
11. Perdew, J. P., Burke, K. & Ernzerhof, M. Generalized Gradient Approximation Made Simple. *Phys. Rev. Lett.* **77**, 3865–3868 (1996).
12. Lee, C., Yang, W. & Parr, R. G. Development of the Colle-Salvetti correlation-energy formula into a functional of the electron density. *Phys. Rev. B* **37**, 785–789 (1988).
13. Koch, W. & Holthausen, M. C. *A Chemist's Guide to Density Functional Theory*. (Wiley, 2015).

14. Becke, A. D. Density-functional thermochemistry. III. The role of exact exchange. *J. Chem. Phys.* **98**, 5648–5652 (1993).
15. Stephens, P. J., Devlin, F. J., Chabalowski, C. F. & Frisch, M. J. Ab Initio Calculation of Vibrational Absorption and Circular Dichroism Spectra Using Density Functional Force Fields. *J. Phys. Chem.* **98**, 11623–11627 (1994).
16. Ernzerhof, M. Construction of the adiabatic connection. *Chem. Phys. Lett.* **263**, 499–506 (1996).
17. Perdew, J. P., Burke, K. & Wang, Y. Generalized gradient approximation for the exchange-correlation hole of a many-electron system. *Phys. Rev. B* **54**, 16533–16539 (1996).
18. Burke, K., Ernzerhof, M. & Perdew, J. P. The adiabatic connection method: a non-empirical hybrid. *Chem. Phys. Lett.* **265**, 115–120 (1997).
19. Adamo, C. & Barone, V. Toward reliable density functional methods without adjustable parameters: The PBE0 model. *J. Chem. Phys.* **110**, 6158–6170 (1999).
20. Langreth, D. C. & Perdew, J. P. Theory of nonuniform electronic systems. I. Analysis of the gradient approximation and a generalization that works. *Phys. Rev. B* **21**, 5469–5493 (1980).
21. Furche, F. Molecular tests of the random phase approximation to the exchange-correlation energy functional. *Phys. Rev. B* **64**, 195120 (2001).
22. Grimme, S. Semiempirical hybrid density functional with perturbative second-order correlation. *J. Chem. Phys.* **124**, 034108 (2006).
23. Perdew, J. P. Climbing the ladder of density functional approximations. *MRS Bull.* **38**, 743–750 (2013).
24. Paier, J. Hybrid Density Functionals Applied to Complex Solid Catalysts: Successes, Limitations, and Prospects. *Catal. Lett.* **146**, 861–885 (2016).
25. Crowley, J. M., Tahir-Kheli, J. & Goddard, W. A. Resolution of the Band Gap Prediction Problem for Materials Design. *J. Phys. Chem. Lett.* **7**, 1198–1203 (2016).
26. Cohen, A. J., Mori-Sánchez, P. & Yang, W. Challenges for Density Functional Theory. *Chem. Rev.* **112**, 289–320 (2012).
27. Semiempirical GGA-type density functional constructed with a long-range dispersion correction - Grimme - 2006 - Journal of Computational Chemistry - Wiley Online Library. https://onlinelibrary.wiley.com/doi/full/10.1002/jcc.20495.
28. Grimme, S. Accurate description of van der Waals complexes by density functional theory including empirical corrections. *J. Comput. Chem.* **25**, 1463–1473 (2004).

29. Grimme, S., Antony, J., Ehrlich, S. & Krieg, H. A consistent and accurate ab-initio parametrization of density functional dispersion correction (DFT-D) for the 94 elements H-Pu. *J. Chem. Phys.* **132**, 154104 (2010).

30. Dion, M., Rydberg, H., Schröder, E., Langreth, D. C. & Lundqvist, B. I. Van der Waals Density Functional for General Geometries. *Phys. Rev. Lett.* **92**, 246401 (2004).

31. Zhao, Y., Schultz, N. E. & Truhlar, D. G. Exchange-correlation functional with broad accuracy for metallic and nonmetallic compounds, kinetics, and noncovalent interactions. *J. Chem. Phys.* **123**, 161103 (2005).

32. Zhao, Y. & Truhlar, D. G. The M06 suite of density functionals for main group thermochemistry thermochemical kinetics, noncovalent interactions, excited states, and transition elements: two new functionals and systematic testing of four M06-class functionals and 12 other functionals. *Theor. Chem. Acc.* **120**, 215–241 (2008).

33. Zhao, Y. & Truhlar, D. G. A new local density functional for main-group thermochemistry, transition metal bonding, thermochemical kinetics, and noncovalent interactions. *J. Chem. Phys.* **125**, 194101 (2006).

34. Zhao, Y. & Truhlar, D. G. Density functional for spectroscopy: no long-range self-interaction error, good performance for Rydberg and charge-transfer states, and better performance on average than B3LYP for ground states. *J. Phys. Chem. A* **110**, 13126–13130 (2006).

35. Schwabe, T. & Grimme, S. Double-hybrid density functionals with long-range dispersion corrections: higher accuracy and extended applicability. *Phys. Chem. Chem. Phys.* **9**, 3397–3406 (2007).

Chapter 3: Assessment of Density Functional Approximations for Highly Correlated Oxides: The Case of CeO_2 and Ce_2O_3

3.1 Introduction

At the begin of my work with ceria, the systems CeO_2/Ce_2O_3 have been already investigated with both the DFT+U and some hybrid functionals, as well the O vacancy on the surface (111) of CeO_2. However, the relatively recent implementation in the *ab-initio* code Crystal of many flavours of hybrid functionals apart from the few employed in the past works lead us to this systematic investigation on the properties of the two oxides performed with many families of hybrid functionals, including global, range-separated and metal-global hybrids.

From a computational standpoint, modelling Ce (III) materials with Density Functional Theory is quite challenging. Conventional DFA struggle with localized 4*f* states due to the well-known SIE. These are particularly ill cases since the delocalization error prevent to distinguish between Ce (III) and Ce(IV), due to the smearing of the 4*f* electron density over the whole material instead of localizing it around the Ce^{3+} ions, as observed from the STM measurements[1]. This unphysical description affects many properties of interest and prevents a useful modelling of these materials. Hybrid functionals mitigate the SIE, leading to the localization of the 4*f* electrons and thus improving the chemical characterization of the system: this approach has been successfully used to study the case of CeO_2 and Ce_2O_3, with different computational settings, but limiting the investigation to few functionals or properties[2,3,4,5].

In this work, we first evaluated the accuracy of different Gaussian Type Orbitals basis sets on the properties of interest of CeO_2 and Ce_2O_3. Once selected the most balanced basis set, we assessed the performance of many XC belonging to different families of functionals on the structural, electronic and thermochemical properties of the bulk phase of CeO_2 and Ce_2O_3. Then, a subset of functionals was selected to model the formation of a defect of oxygen (V_O) and the concomitant reduction of two Ce^{+4} to Ce^{+3} on the surface 111 of CeO_2.

3.2 Computational details

The results here reported have been obtained with the package CRYSTAL14[6], with the exception of the calculations with CAM-B3LYP[7], performed with the CRYSTAL17[8] version. The properties of

the CeO_2 and Ce_2O_3 bulk phases have been computed using 27 Density Functional Approximations (DFA): 1 GGA (PBE[9]), 1 Meta-GGA (M06-L[10]), 5 Meta-GHs (M05[11], M05-2x[12], M06[13], M06-2x[13], M06-HF[10]), 9 global hybrids (B3LYP[14], B3PW[14,15], PBE0[16], PBE0-13[17], PBEsol0[18], PW1PW91[19], WC1LYP[20], B97H[21,22], B1WC[23]) and 10 RSH (HSE06[9,24], HSEsol[18,25], HISS[9,26,27], LC-ωPBE[9,28], LC-ωPBEsol[18,28], LC-ωBLYP[29], RSHXLDA[30,31], ωB97[21,32], ωB97-X[21,32], CAM-B3LYP[33]) functionals. (See the **Table A1** in **Appendix A** for an overview of the main characteristics of the XC functionals employed). We have performed calculations also with Hartree-Fock to compare the DFT results with a method not suffering from the SIE.

Ce have been described using a relativistic small core Effective Core Potential (scECP) developed by Dolg and co-workers[34] which replaces the $1s^2 2s^2 2p^6 3s^2 3p^6 3d^{10}$ inner core, while the remaining $4s^2 4p^6 4d^{10} 5s^2 5p^6 4f^1 6s^2 5d^1$ electrons have been treated as valence.

This ECP was the same used in previous works [13,15,16,20] and it has been shown to be the most suitable to describe both CeO_2 and Ce_2O_3. Then, 3 valence basis sets (BSs) have been considered to describe the Ce valence electrons: the one used by Graciani et al.[35] (named Ce1, hereafter), a modification of this with an added contraction constituted of a single Gaussian primitive with exponent 0.27 for the 5*d* shell (named Ce2, hereafter) and, lastly, a pruned version of the segmented basis set developed by Dolg and co-workers[36]. In the latter case, all the g functions have been removed, not supported by CRYSTAL14, as well all the functions with exponents lower than 0.11, to avoid pseudolinear dependency issues. The resulting BS has been named as Ce3.

For Oxygen we have used the same BS employed by Graciani *et al*[35] (named O1, hereafter) and a larger basis set of Quadruple-Zeta plus polarization quality[37](O2). For Hydrogen a Triple-Zeta plus polarization BS has been used[38].

From the combination of the 3 BSs for Ce and of the 2 BSs for O, 6 distinct BSs have been obtained to describe the cerium oxides. The effects of the aforementioned BSs on the properties of interest have been tested with the PBE0 functional.

To reduce the computational burden, we investigated only the ferromagnetic (FM) state for Ce_2O_3 instead of the ground state antiferromagnetic (AFM), which requires a broken symmetry or a supercell approach. This decision is supported by the extremely low difference in energy of the two states, of the order of 10 meV, found by previous works and demonstrated by the extremely low Neel temperature[39] (proof of a very weak magnetic coupling). To accelerate the SCF (Self -Consistent -Field) convergence of the Ce_2O_3 the initial occupation of 4*f* AOs of Ce has been set using the keyword FDOCCUP to have a ground state formed by a mixing of the components $(2z^2-3x^2-3y^2)z$ and $(x^2-3y^2)x$. The reciprocal space of the primitive lattices of both oxides has been sampled with a

Monkhorst-Pack grid 6 x 6 x 6 for all the calculations, except for the computation of the elastic properties, which required the use of a finer k-point mesh of 12 x 12 x 12.

The radial and angular points for the integration grid have been generated according to the Gauss-Legendre radial quadrature and the Lebedev two-dimensional angular points distribution schemes. The default grid (XLGRID) have been employed for all calculations. The truncation criteria of the Coulomb and exchange infinite lattice series are controlled by five thresholds, T_i, which have been set to 8 (T_1–T_4) and 20 (T_5) for all the calculations.

Default convergence thresholds on gradients and displacements have been used for all the geometry optimizations of the primitive cells of CeO_2 and Ce_2O_3, while the threshold on energy change has been raised to 10^{-8} Hartree for the geometry optimization and elastic properties computations and to 10^{-10} Hartree for frequencies calculations at the Γ point. Both the atomic positions and the lattice parameters have been optimized for the primitive structures until the full convergence of atomic gradients and displacements. Elastic properties have been calculated according to the model of Reuss-Voigh-Hill for polycrystalline materials, following the automated procedure implemented in the code[40,41].

Defects calculations. Oxygen vacancies have been modelled on the surface (111) of CeO_2, employing a 2D slab model with a p(2x2) periodicity of the surface unit cell, composed by 3 CeO_2 layers (overall 36 atoms for the pristine cell). This is the same model employed by Ganduglia-Pirovano *et al*[42] in their HSE06 and DFT+U investigation on the stability of the configurations of the O vacancy and it is justified by the experimentally observed ordering of oxygen vacancy after annealing of a surface 111 of CeO_2[43]. The model does not simulate the isolated vacancy, the defect concentration is θ = ¼, but it is considered sufficiently accurate to allow a consistent comparison of the results with different XC functionals.

In our approach, we remove the O atom, leaving the basis set of Oxygen as ghost functions to describe the electron density of the vacancy.

The reciprocal space for the periodic 2D slab model has been sampled with a k-point mesh of 4 x 4 x 1 for the structure optimization, employing the basis set Ce2-O1.

We have investigated only the ferromagnetic ordering of the Ce^{3+} since most authors reported extremely low magnetic coupling, similarly to the Ce_2O_3 bulk phase.

The total energy has been then computed from single point calculations on the optimized structures employing the largest basis set combination Ce3/O2, with a k-point mesh of 6 x 6 x 1.

In all these calculations, the lattice constants have been fixed to the bulk optimized values while the atomic positions in the cell have been allowed to relax. The starting guess for the occupation matrix has been made by the atomic configurations of Ce and O, without assigning an initial spin polarization

to the single atoms. With this relaxation scheme the excess of spin density localize on two Ce nearest neighbours (NN-NN configuration) to the vacancy, with all the hybrid XC tested.
Convergence of the geometry optimization has been considered achieved when the maximum atomic gradient was below 0.00045 Hartree/Bohr and the energy change from subsequent steps was below 10^{-6} Hartree.

3.3 Results

3.3.1 Basis set evaluation

In order to identify a BS computationally efficient to be used to model extended surfaces of CeO_2 of interest for catalysis, we performed an evaluation of the GTO BS commonly adopted in previously published investigations.
Kullgren *et al*[4] showed the shortcomings of different large core(lc) ECP BSs for Ce in reproducing the structural and electronic properties of the 2 cerium oxides, which instead are satisfactorily reproduced by the use of scECP BSs, at the expense of increase significantly the computational workload.
Successively, Graciani *et al*[5] performed an assessment of 5 hybrid functionals on the properties of the two cerium oxides, including the thermochemistry of reduction in their calculations. They adopted a reoptimized BS for the scECP of Ce, less demanding than the ones tested by Kullgren *et al*[4], aimed to give a balanced description of the Ce^{+4} and Ce^{+3} states. While the computed structural and electronic properties agreed with the PW results (PBE0) of De Silva *et al*[3], the energies of reduction were overestimated by about 0.5 eV.
We selected the BSs of Graciani *et al*[5] for Ce and O (Ce1 and O1) as the best BS of small size. We tried to improve Ce1 by including a contraction of symmetry *d* to formed by a single primitive Gaussian function with exponents of 0.27. This modification is then called Ce2. We included in the evaluation the more extended Ce3, pruned by all the primitives with exponents below 0.11 when used for periodic calculations, and the BS O2, optimized for periodic calculations. We evaluated at the PBE0 level the performance of the BSs on the structural, electronic, vibrational properties of the two oxides, other than the thermochemistry of the reduction process of the CeO_2 to Ce_2O_3. **Table 1** and **Table 2** report the results for CeO_2 and Ce_2O_3, respectively.

Table 1. Computed and experimental properties of the fluorite cubic structure of CeO_2: lattice parameter (*a*), the bulk modulus (B_0), the independent elastic tensor components (C_{11}, C_{12}, C_{33}), the band gap O 2*p* - Ce 4*f*, O 2*p* – Ce 5*d* and Ce 4*f* – Ce 5*d*, the vibrational mode IR and Raman active (F_{1u} and F_{2g}). The energy of reduction (E_r) from CeO_2 to Ce_2O_3 is computed with respect to the formation of ½ O_2: in one case, we used the electronic energy of O plus half the experimental O_2 binding energy (2.58 eV) whereas in the other case half of electronic energy of O_2. All the calculations were obtained with PBE0 and the selected basis sets listed in the first six columns; other results obtained with PBE0 are reported in the column 'Other Cal'.

Basis set	**Ce1/O1**	**Ce1/O2**	**Ce2/O1**	**Ce2/O2**	**Ce3/O1**	**Ce3/O2**	**Exp.**	**Other Cal.**
a **(Å)**	5.403	5.394	5.407	5.403	5.400	5.401	5.411[44]; 5.406[45]; 5.391[46]	5.411 (GTO)[47] 5.393 (GTO)[48] 5.423 (GTO)[49] 5.39 (PAW)[3]
B_0 (GPa)	217.2	220.4	212.6	211.7	204.6	209.0	204[50]-220[44]-230[50]-236[45]	219 (GTO)[48]
C_{11} (GPa)	420.9	424.3	411.3	410.2	402.5	406.9	403[50]	426 (GTO)[48]
C_{12} (GPa)	115.4	118.4	113.3	112.4	105.6	110.1	105[50]	116 (GTO)[48]
C_{33} (GPa)	62.9	68.6	61.7	63.2	59.2	60.4	60[50]	65 (GTO)[48]
2*p* - 4*f* (eV)	4.35	4.30	4.29	4.42	4.33	4.33	2.6-3.9[51]	4.32 (GTO)[48] 4.5 (PW)[3]
2*p* - 5*d* (eV)	8.58	8.50	8.15	8.41	8.01	8.40	5.5-8.4[51]	8.24 (GTO)[48] 7.93(PW)[3]
4*f* - 5*d* (eV)	3.10	3.38	2.73	3.02	2.46	3.00		2.25(PW)[3]
Freq (cm^{-1}) F_{1u} I	294	287	290	277	285	269	272[17,18]	295(GTO)[48]
Freq (cm^{-1}) F_{2g} R	469	465	463	458	463	457	464-465[50,52,53]	470(GTO)[48]
E_r (eV) (O + ½ Exp binding)	3.35	3.28	3.21	3.11	3.00	2.80	4.03[54]	
E_r (eV) (½ O_2)	3.68	3.17	3.54	3.00	3.33	2.69	4.03[54]	3.14(PW)[3]

Table 2: Computed and experimental properties of the hexagonal phase of Ce_2O_3. All the calculations were obtained with PBE0 and the selected basis sets listed in the first six columns; other results obtained with PBE0 are reported in the column 'Other Cal'.

Basis set	**Ce1/O1**	**Ce1/O2**	**Ce2/O1**	**Ce2/O2**	**Ce3/O1**	**Ce3/O2**	**Exp.**	**Other Calc.**
a (Å)	3.860	3.859	3.869	3.869	3.868	3.868	3.888[55], 3.891[56]	3.87(PW)[3]
c (A)	6.038	6.043	6.055	6.065	6.072	6.087	6.063[55], 6.059[56]	6.06(PW)[3]
c/a	1.564	1.566	1.565	1.571	1.570	1.574	1.559[55],1.557[56]	
Bo H (GPa)	142.3	138.9	136.1	132.7	136.1	132.3	111[57]	
C_{11} (GPa)	249.2	254.5	237.9	236.3	237.0	234.7		
C_{12} (GPa)	141.2	136.8	137.8	134.5	136.8	131.2		
C_{13} (GPa)	98.9	93.1	94.4	89.2	92.9	88.2		
C_{33} (GPa)	160.0	156.4	152.0	150.8	154.7	152.4		
C_{44} (GPa)	76.6	78.1	72.8	71.3	69.7	68.0		
C_{46} (GPa)	-38.1	-36.7	-36.5	-36.9	-37.2	-37.4		
2*p* - 4*f* (eV)	2.40	2.17	2.07	2.05	1.83	1.79	2.40[58,59]	2.75(PW)[3]
2*p* - 4*f*/5*d* (eV)	7.08	7.42	6.58	6.67	6.38	6.33		6.25(PW)[3]
4*f* - 4*f*/5*d* (eV)	4.25	4.60	3.85	3.95	3.88	3.86		3.50(PW)[3]
Freq (cm^{-1}) E_g R	108.0	110.7	106.6	107.0	105.6	104.2	103[60]	
Freq (cm^{-1}) E_u I	192.0	185.2	192.3	194.5	201.4	192.1		
Freq (cm^{-1}) A_{1g} R	203.0	202.0	202.2	195.6	193.5	188.3	189[60]	
Freq (cm^{-1}) A_{2u} I	208.0	219.0	218.7	214.8	222.3	208.7		
Freq (cm^{-1}) E_u I	392.9	392.1	387.5	380.0	380.1	375.5		
Freq (cm^{-1}) E_g R	426.1	425.2	422.8	417.4	418.4	410.2	409[60]	
Freq (cm^{-1}) A_{1g} R	432.0	429.6	425.0	423.1	425.7	415.9	409[60]	
Freq (cm^{-1}) A_{2u} I	475.4	473.8	466.8	464.1	468.8	459.0		

Structures. The results show that the lattice vector *a* of both oxides is little affected by the BS, while the *c* vector of Ce_2O_3 (**Table 2**) increases with the size of the BS for both Ce and O, giving a more elongated structure compared to experiment (increasing *c/a* ratio).

Elastic properties. The bulk modulus of both oxides decreases when extending the basis set of Ce. The increment of the size of the O BS rises the data value of the bulk modulus for CeO_2 but decreases it for Ce_2O_3. The adiabatic bulk modulus of CeO_2 (204 GPa) and the independent elastic tensor

components C_{11}, C_{22} and C_{44}, are well reproduced by all the BSs with an almost perfect agreement found for the larger Ce3/O1 and Ce3/O2 BSs. Instead, the adiabatic bulk modulus of Ce_2O_3 is overestimated of about 20-30 GPa with all the BSs tested. However, it is worth to note that since the dispersion of the experimental data reported in the literature is large all the results can be considered acceptable.

Vibrational frequencies. The harmonic vibrational frequencies decrease when the size of the basis of Ce and O increase for both oxides, except for the vibrational modes below 250 cm^{-1} in Ce_2O_3 whose exhibit an oscillating dependence by the size of the basis set.

Electronic structure. The O 2*p* – Ce 4*f* band gap of CeO_2 (**Table 1**) is little affected by the BS and well reproduced with all of them compared to other results obtained with PBE0, both with GTO and PW basis set, but it is higher compared to the experimental values, confirming the general trend of PBE0 to overestimate the band gap of semiconductors[61].

The O 2*p* – Ce 5*d* gap is also overestimated with respect to the experimental data and decreases with the BS size from 8.58 eV to 8.01 eV for Ce1/O1 and Ce3/O1, respectively. The fundamental gap of Ce_2O_3, defined as the gap between the filled Ce 4*f* states and the upper conduction band constituted by the Ce 4*f* and the Ce 5*d* empty states, is also influenced by the BS. It decreases from Ce1 to Ce2 and Ce3. The latter two BSs provide the same results. The same trend was observed for O 2*p* - Ce 4*f*/5*d* gap. The intra-gap between the filled O 2*p* and Ce 4*f* states decreases as the BS size increases (**Table 2**), in correlation with the reduction energies of CeO_2 to Ce_2O_3 (**Table 1**).

Thermochemistry. The energy of reduction of the cubic CeO_2 to hexagonal Ce_2O_3 and molecular O_2 (see **Table 1**) computed with the Ce1-O1 BS is overestimated with respect to the PW calculations of De Silva et al[3]. This is due to the poor description of the molecular O_2 since the O BS was optimized for the oxide, as was reported by Paier *et al*[62]. In fact, by improving the oxygen BS (Ce1-O2 and Ce2-O2) the reduction energy come closer to the one found with PW calculations (3.14 eV)[3]. However, a further improvement of the basis set of Ce (Ce3-O2) results in a higher stabilization of the reduced form, which yields an underestimation of 0.45 eV with respect to PW calculations with the same functional.

To explain this difference, we calculated the atomization energy of CeO_2, Ce_2O_3 and O_2 with the BS Ce3-O2 and compared the results with the ones of De Silva et al[3]. Atomic Ce, O and molecular O_2 are modelled as isolated species, all as triplet states. The diffuse primitives removed from the BS Ce3 for the solid calculations were reintegrated in the BS for the atomic calculation.

Our GTO and De Silva's PW results for O_2 provided the same dissociation energy (5.37 eV) and reasonable differences in the atomization energy of CeO_2 (19.37 eV (GTO), 19.13 eV (PW)), which can be ascribed to the different pseudo-potentials employed for Ce and different orbital occupations

for the atomic Ce. For Ce_2O_3 (FM configuration), our GTO result (33.36 eV) is 0.91 eV higher than the PW one (32.44 eV): the same justification used for CeO_2 can explain half of this difference, while the other half (0.45 eV) can be justified if the results obtained with PW were for a metastable solution for Ce_2O_3, which can be easily obtained when starting the SCF process from a different guess. These results show that the modelling of Ce_2O_3 is challenging even with hybrid functionals. Different starting geometry, symmetry and the initial electronic configuration can easily lead to different results. Many metastable states, differentiated by the different occupation of the 4*f* orbitals, exist for Ce_2O_3. For all the calculations on this oxide we checked the convergence towards the occupation of the lowest energy (in the crystalline field environment of Ce_2O_3) 4*f* $(2z^2\text{-}3x^2\text{-}3y^2)z$ and $(x^2\text{-}3y^2)x$ atomic orbitals by inspecting the Mulliken population of spin.

In conclusion, we observed that the modified basis Ce2-O1 performs better than the original one for all the properties tested, better approximating the results of the largest BS. The largest BS (Ce3-O2) provides higher accuracy for most of the properties investigated, except for the band gaps involving the Ce 5*d* conduction band.

3.3.2 Lattice parameters

3.3.2.1CeO_2

The optimized cell parameter obtained for the different Hamiltonians is reported in **Table A2.**

The largest deviation from the experiment is by about 0.1 Å, computed with the meta-GGA M06L. Among hybrids, distinctions can be made between the Minnesota functionals (M05, M052X, M06, M062X, M06HF), the XC functionals based on the LYP correlation functional (B3LYP, WC1LYP, LC-BLYP, CAM-B3LYP), the ones derived by PBE and similar GGAs (PW1PW91, B1WC, B3PW91) and lastly the ones based on PBEsol.

PBE and PBE derived hybrid XC provided the smaller deviations from the experimental value, independently by the typology of hybrid (global, short/medium/long range separated). LYP derived hybrids overestimate the lattice constant by about 0.04-0.06 Å, while PBEsol derived ones underestimate it by 0.03-0.05 Å. The Minnesota family of XC performed non-homogeneously, with the computed value spanning from +0.09 to -0.05 Å from the experimental value. Within each family of functionals, we observe an inverse correlation between the computed lattice parameter and the weight of EE incorporate in the functional.

The more evident case is for the series PBE, PBE0 and PBE0-13, with respectively 0, 25 and 33 % of EE. While PBE overestimates the lattice constant, the hybrids provide results much closer to the experiment.

Similarly, the lattice parameter computed with the M06 family (M06L, M06, M062x and M06HF) exhibit the same correlation with the fraction of EE in the XC.

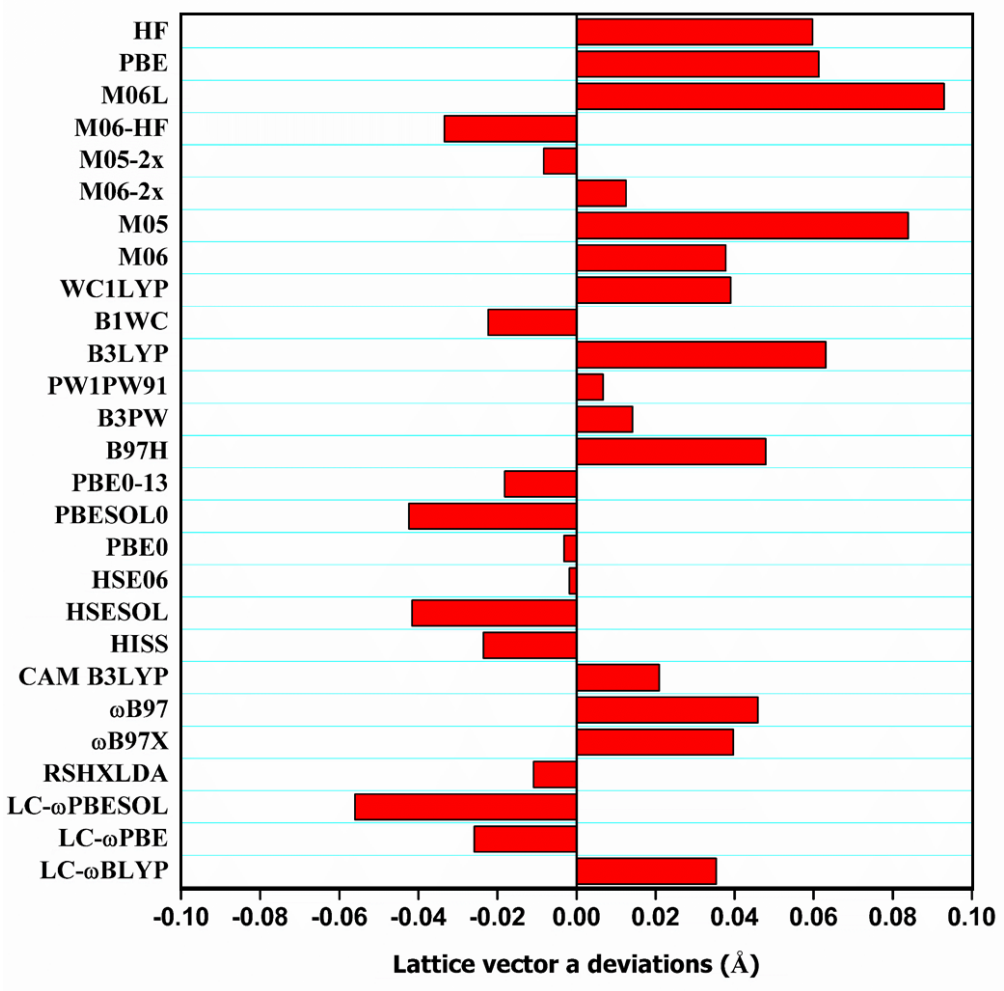

Figure 1. Difference between the calculated equilibrium cell parameter and the experimental value for CeO_2.

3.3.2.2Ce_2O_3

The computed parameters are reported in **Table A3**.

The largest deviations for the lattice parameter *a* are about ± 0.04 Å, while for *c* the largest deviations are + 0.19 and -0.14 Å.

The same trends observed for the cell parameter of CeO_2 are also found for the sesquioxide: the PBEsol based XC overbind with respect to the PBE based XC, while the ones based on the LYP correlations overestimate more *c* than *a*, which results in an elongated cell along the z-axis.

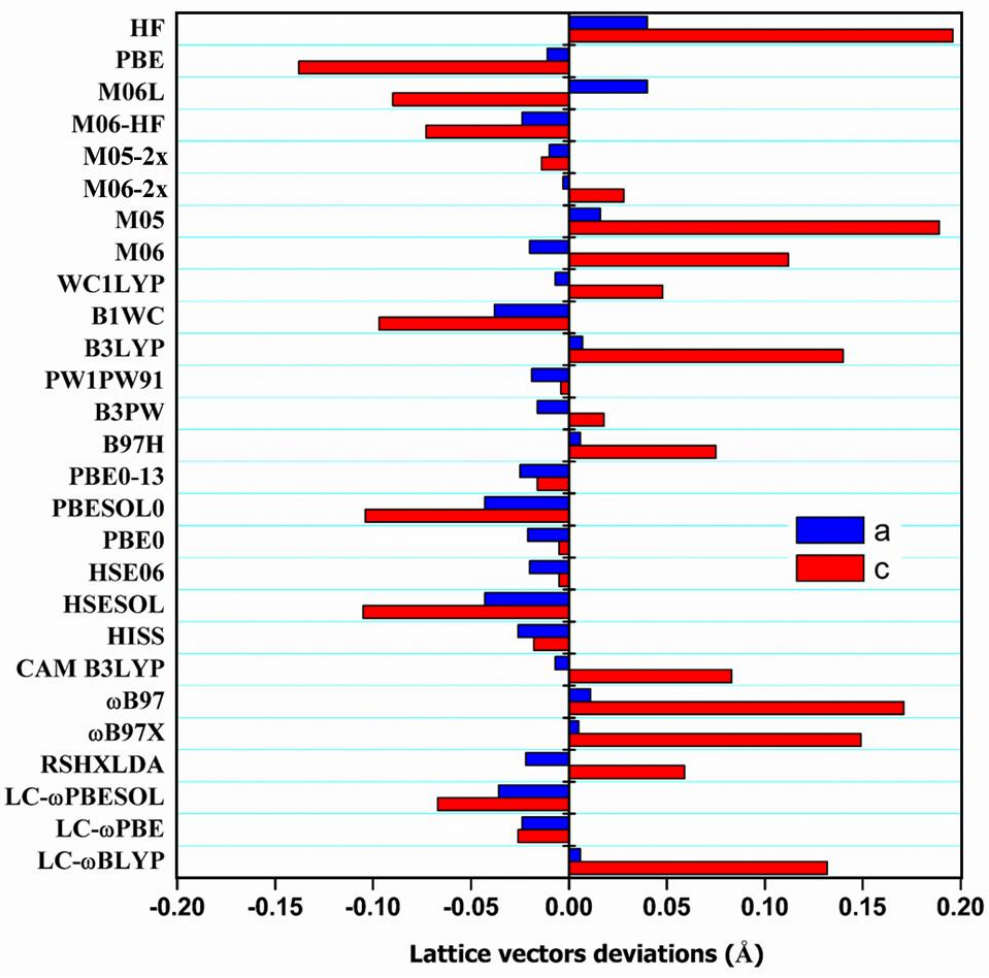

Figure 3. Difference between the calculated equilibrium cell parameters *a* and *c* and the experimental values for Ce_2O_3.

The comparison of the deviations for *a* and *c* shows a much larger dispersion among the values of *c*. Cases with ratio *c*/*a* closest to the experimental value of 1.56 exhibit a distance Ce-Ce intracell very similar (ideal case 3.71 and 3.81 Å). For elongated cells the difference between the two distances close-up (Δ up to 0.05 Å), while it increases for compressed cell (Δ up to 0.16 Å).

3.3.3 Elastic Properties.

After the lattice optimization, the elastic properties of the solid can be computed and compared with experiments to validate the method. Elastic properties characterize the mechanical hardness of the materials and their structural stability. In the present work, we adopted the second derivative method to get the elastic tensor by computing the non-zero components by the exploitation of the Laue class of the lattices. The second derivatives are computed as numerical derivatives of the analytical energy gradients.

From the 36 components of the tensor, at least 21 are independent. If the crystal group symmetry is considered the number of independent components further decrease according to the Laue class.

The tensor's components are derived from the energy of the structure through a Taylor expansion truncated at the second order of the strain components.

Once obtained the elastic tensor, several elastic properties can be readily computed from simple relations involving the independent elastic constants or their reciprocal, as the Bulk modulus, the shear modulus, the Poisson's ratios and acoustic velocity in the solid.

In this work, we reported the independent elastic tensor components computed and the Bulk modulus (see **Table A2** and **Table A3** for the numerical results of CeO_2 and Ce_2O_3, respectively). The other elastic properties can be directly computed from the elastic constants alone.

3.3.3.1 CeO_2

By exploiting the cubic symmetry of the lattice, the number of independent tensor components to be computed is reduced from 21 to 3, the diagonal elements C_{11}, C_{21}, C_{44}.

The computed Bulk modulus depends significantly on the lattice parameter, increasing with the decrease of the latter. The best performing functionals for lattice parameters are also best performers for Bulk modulus.

The largest deviations obtained are of 31% GPa (M06-HF) and about -13% GPa (M06L and PBE).

Interesting, also the Bulk modulus is affected by the amount of EE incorporated in the functional, increasing with the latter, in agreement with an increase ionicity of the lattice.

To this regard, we found for the series PBE, PBE0, and PBE0-13 a direct proportionality between the Mulliken's charge of Ce (2.35, 2.59, and 2.66 respectively) and the Bulk modulus (176.9, 212.6, 222.7 GPa). The Minnesota suits of functionals behave differently from the others: when comparing Bulk modulus of structures with similar lattice parameter, the Minnesota functionals have higher Bulk modulus, thus higher rigidity. A possible explanation is that the Minnesota functionals have been parametrized to include dispersion interactions, resulting in stronger cohesive forces.

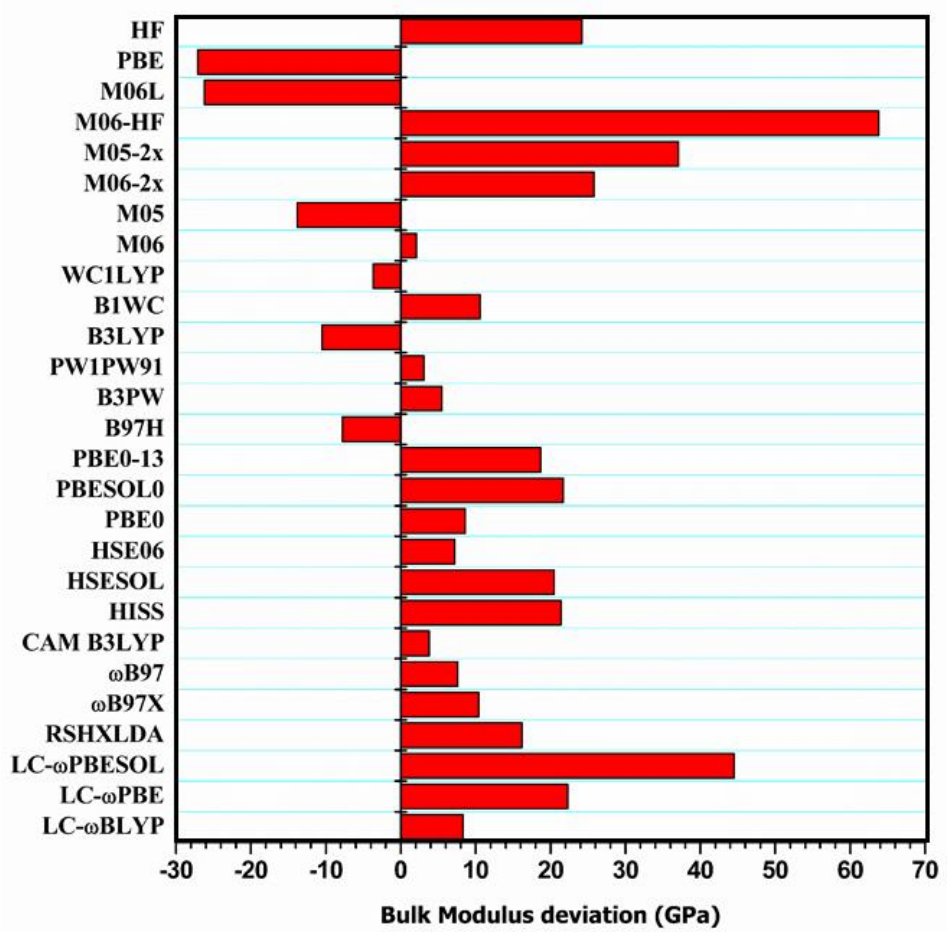

Figure 4. Difference between the computed adiabatic Bulk Modulus B_0 and the experimental value for CeO_2.

3.3.3.2 Ce_2O_3

The hexagonal symmetry of the lattice requires to compute 5 independent tensor components, listed in the **Table A3.3**. For the hexagonal case, B_0 can be calculated according to different formulas. Here we reported the Hill's Bulk modulus, computed as an average of the Reuss and Voigt values. To the best of our knowledge, there are no other B_0 values computed at the hybrid level for Ce_2O_3 in literature, and only an experimental value of 111 GPa has been reported.

All the functionals tested overestimate the experimental value by 10-45 GPa (11-44 %), at the exception of PBE, in very good agreement (109 GPa) and M06L which overestimates it by 10 GPa. All the hybrids well reproducing the lattice constant overestimate the Bulk Modulus by at least 25 GPa.

As seen in **Tables 1 and 2**, the elastic properties are moderately affected by the BS quality. With respect to Ce3-O2, Ce2-O1 provides a B_0 larger by about 9 and 6 GPa for CeO_2 and Ce_2O_3, respectively.

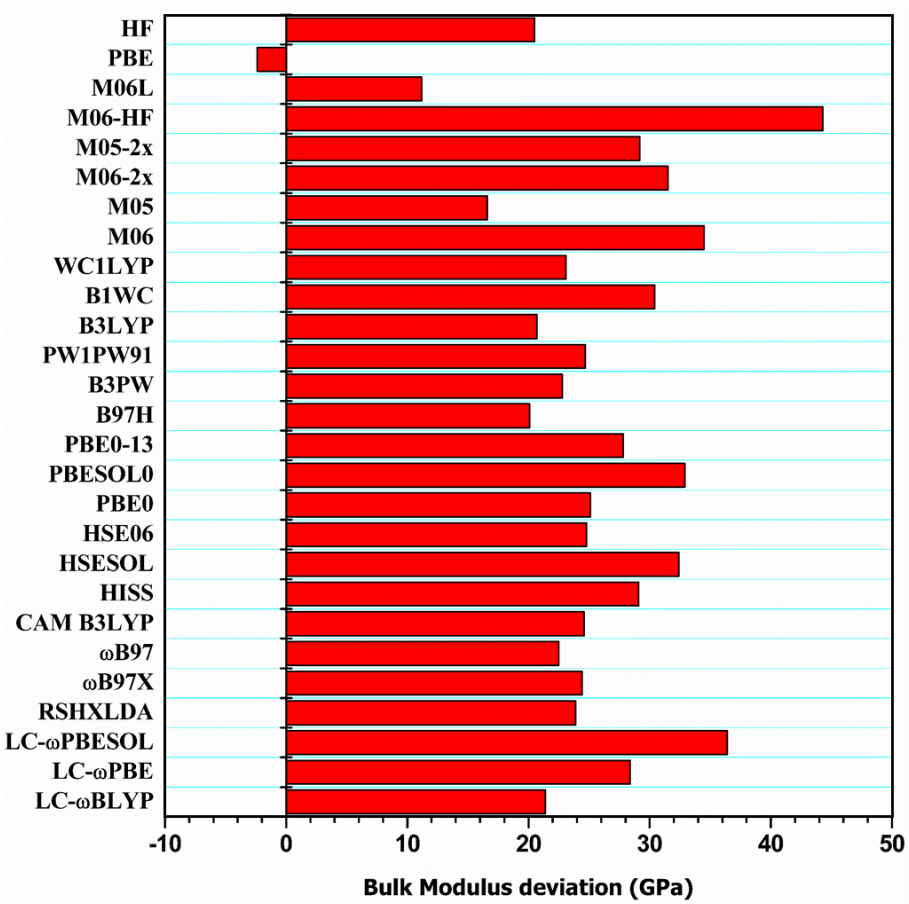

Figure 5. Difference between the computed adiabatic Bulk Modulus B_0 and the experimental value for Ce_2O_3.

3.3.4 Vibrational Frequencies

In order to calculate the mass-weighted Hessian matrix required for a vibrational frequency calculation in the harmonic approximation, the force-constants can be computed either from numerical differentiation using the finite difference approach or from a density functional perturbation theory (DFPT) technique. The first method is implemented in the CRYSTAL package: the second derivatives of the energies are computed numerically by using the analytical gradients.

3.3.4.1 CeO_2

The vibrational structure of lattice with cubic symmetry as ceria is extremely simple, with 1 active mode IR of F_{1u} symmetry at 272-276 cm^{-1} and 1 active mode Raman of F_{2g} symmetry at 464-465 cm^{-1}. Here the harmonic frequencies have been computed at the Γ point exploiting the full symmetry of the lattice space group and are reported in **Table A4**

In general, the Minnesota's family of XC gives the largest deviations for both vibrational modes, with the worst performance by M06-HF which underestimates the F_{2g} mode by about 75 cm^{-1} and overestimates the F_{1u} mode by 170 cm^{-1}. Global Hybrids and Range Separated performs rather similarly, with the exception of the GH B97H which underestimate the low frequency mode by 112

cm^{-1}. As previously reported, HSE06 and PBE0 perform rather well. However, it has to be considered the BS effect on the computed frequencies: the assessment performed with PBE0 shows a blue-shift of 21 and 7 cm-1 for the F_{1u} and F_{2g} modes from the Ce2-O1 to the Ce3-O2 BS results. Therefore, the relative performance of the XC with the smaller deviations could change if the more extensive BS is adopted.

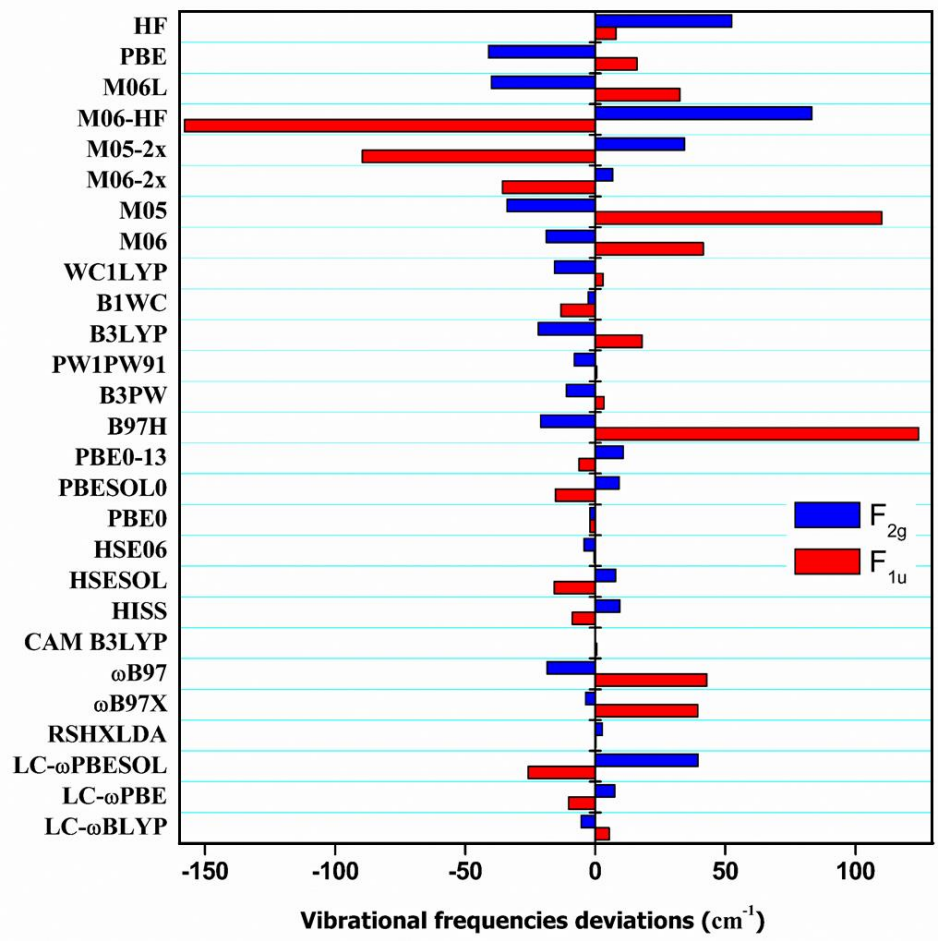

Figure 6. Difference between the computed harmonic vibrational modes and the experimental value for CeO_2.

3.3.4.2 Ce_2O_3

The vibrational data concerning the sesquioxide are limited to the Raman spectra[60], while for the IR exists only very partial data obtained on the product of the decomposition of the cerium carbonate[63]. According to group theory, the 12 vibrational modes of the unit cell are classified in 4 different Raman active modes of symmetry Eg, A_{1g}, E_g and A_{1g} and 4 distinct IR active modes of symmetry E_u, A_{2u}, E_u, A_{2u}. We reported all the computed frequencies in **Table A4**.

We selected 3 of the best performing XC to simulate the Raman spectra, namely PBE0, PW1PW91 and B1WC, with the most extensive BS Ce3-O2 (the structures were reoptimized with this BS).

Figure 7 reports the experimental Raman spectra overimposed with the simulated ones. The best match has been obtained with PBE0, which performs very similar to HSE06 results in the PW implementation, used in ref [64] to computed the Raman frequencies.

We have not simulated the HSE06 spectra being not yet implemented the Coupled Perturbed Kohn-Sham procedure for Range-Separated functionals.

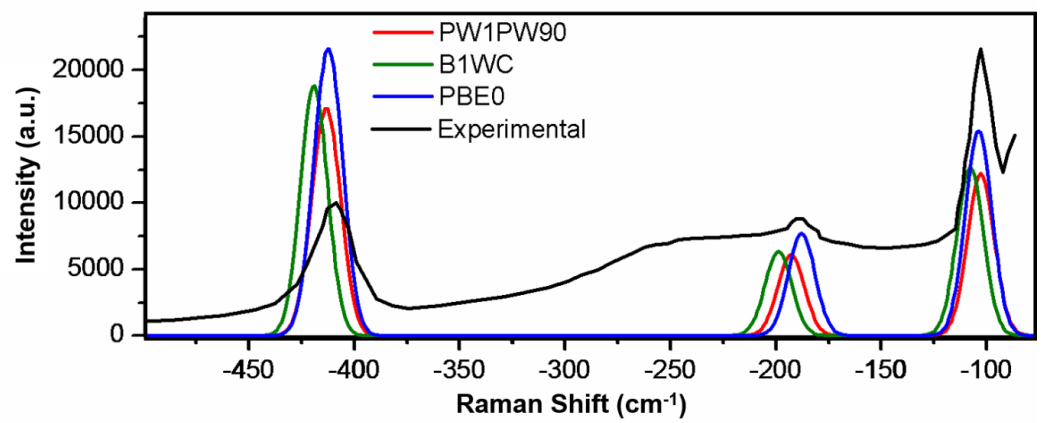

Figure 7: Simulated PBE0, B1WC and PW1PW91 Raman spectra of Ce_2O_3 compared with the experimental spectrum digitalized from ref 64. Calculated intensities were scaled to match the highest intensity experimental peak and convoluted with Gaussian functions. A standard band width of 15 cm^{-1} has been applied.

3.3.5 Electronic Properties

The fundamental gap (E_g)is the most basic property of a periodic solid: it discerns insulators from metals and characterizes the low energy single-electron excitations. It is well known that earlier DFA as LDA and GGA underestimate E_g significantly, while higher level of approximations performs better. Formally, the energy gap between the HO-LO orbitals is computed from the difference between the first ionization potential and the first electronic affinity:

$E_g = I-A$.

Obtaining I and A require to ionize the system, which means to compute the system with N+1 and N-1 electrons. While this approach may be straightforward for molecules, for solids it is not: E_g need to converge (or the cluster size, if this approach is taken), thus requires much more resources to be computed.

Instead, the approach most used to compute E_g in solids is to use the HOCO-LUCO gap, neglecting the orbital relaxation after ionization. This approximation holds for approximated XC functionals, while it would not hold for the exact functional, due to the derivative discontinuity[65]. Nevertheless, it is useful for a fast evaluation of the gap of materials.

Cerium oxides are semiconductors with the band gap involving the 4*f* orbitals.

Experimentally, the band gap of undefective (pristine) cerium oxide falls within 5.5 and 8 eV and it is associated to the transition between O 2*p* valence band and the Ce 5*d* virtual band. In between falls a narrow Ce 4*f* virtual band, 2.6-3.9 eV above the valence band, in the so-called forbidden gap region.

When CeO_2 is reduced, the electrons are trapped in the Ce 4*f* levels, which have a strong atomic character and are localized around the Ce atoms: the Ce 4*f* band then splits into an occupied band about 2 eV above the top of the O 2*p* band, and into the virtual band 1-1.5 eV above the other.

As for partial reduced CeO_2, the top valence of Ce_2O_3 is formed by a narrow band of Ce 4*f* level, while the conduction is formed by a mix of Ce 4*f* and Ce 5*d* states. Experimentally, the corresponding E_g is of 2.4 eV[58]: it has to be remarked that more sophisticated approaches to compute the band structure, as G_0W_0 and GW_0, predict a much smaller gap of 1.29 and 1.50 eV, respectively[66].

3.3.5.1 CeO_2

For simplicity, despite the large dispersion of the experimental data, we chose as reference for the gaps O 2*p* Ce - 4*f* and O 2*p* - Ce 5*d* the values of 3 and 6 eV, similarly to previous works. We remark also that the gap involving the diffuse Ce 5*d* virtual orbitals is particularly sensible to the basis set quality: previous work of Graciani *et al*[5] with GTO BSs underlined a systematic overestimation of about 1 eV with respect to the results of De Silva *et al*[3] obtained with a PW BS. Here, the discrepancy with the PW results has been reduced with the inclusion of a diffused 5*d* contraction. The computed band gap is well known to be affected much more by the weight of the EE respect the underling LDA or GGA functional.

O 2p – Ce 4f gap.

The forbidden gap is predictably overestimated by HF (+11 eV) and M06HF (+10 eV) which have both the full EE. Also, LRHs, with 100 % of EE at long range, largely overestimate the gap by about 5-7 eV. CAM-B3LYP with the 90% at long range (and 30 % at short range) performs slightly better (+ 3.4 eV). Reliable values (within 1 eV from the reference) are provided by global hybrids with % of EE in the range of 26 (M06) and 16 (B1WC, WC1LYP), and by the SRHs (HSE06, HSEsol). PBE and M06L, the only non-local functionals considered, both underestimate the gap by 1.1 and 0.9 eV, respectively.

O 2p – Ce 5d gap.

All the functionals tested overestimate the gap, including the local XC PBE and M06L (+0.3 and + 0.7 eV). The trends are similar to the ones observed for the other gap, but on average the deviations

are larger by about 0.5-2.0 eV. Only exceptions are M06-HF and HF which overestimate less the 2*p* – 5*d* gap with respect to the forbidden one.

Since GGAs are known to systematically underestimate the band gap of insulators, at increasing extent with the increase of band gap, it is likely that the reference value of 6 eV for the 2*p* – 5*d* gap here considered is an underestimation of the effective gap.

Figure 8 depicted the computed deviations, while the numerical values are reported in **Table A5**.

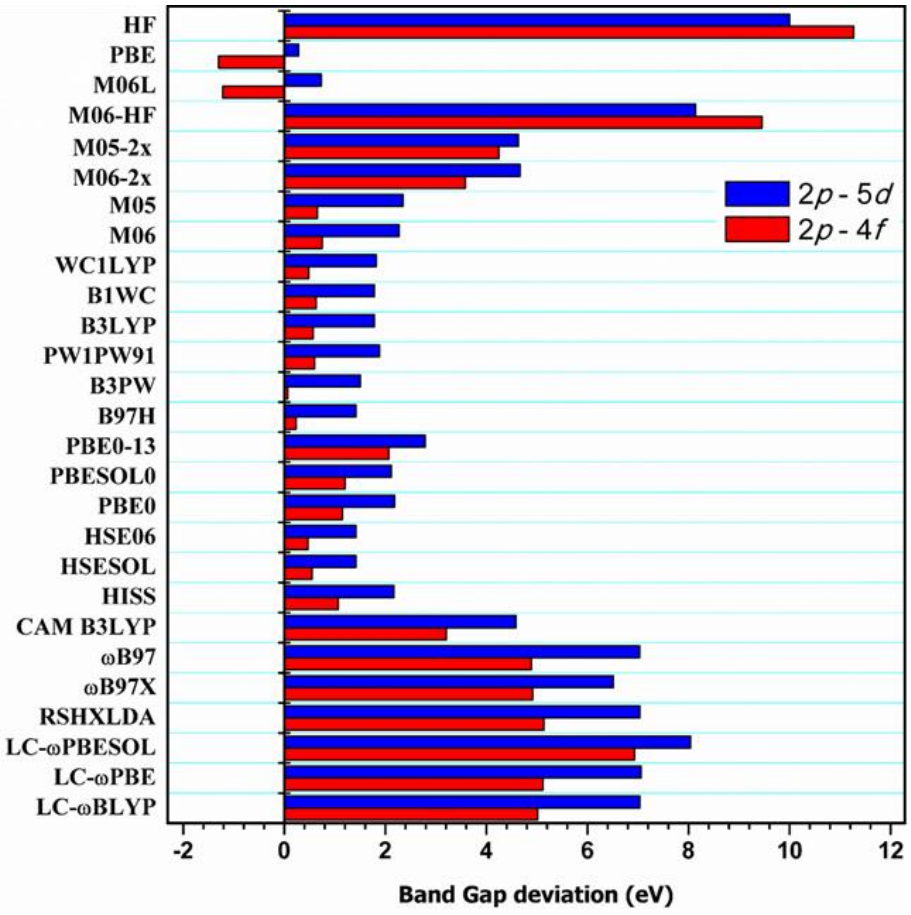

Figure 8. Difference between the computed O 2*p* – Ce 4*f* and O 2*p* Ce 5*d* gaps and the experimental band gaps for CeO_2.

3.3.5.2 Ce_2O_3

In Ce_2O_3 the Ce 4*f* levels are divided into an occupied band (top valence) and a virtual band (conduction). The latter is mixed with the Ce 5*d* virtual levels to form the conduction.

Similar trends to the gaps for CeO_2 are observed. HF and M06-HF overestimate the gap the most, followed by LRSHs. Best performing GHs contain between 16 and 20 % of EE or are the SRHs HSE06 and HSEsol.

Here PBE predicts a 0 eV gap material (not metallic but semi-metallic), while the meta-GGA M06L predicts a band gap of 0.6 eV, similarly to the result with TPPS of Hay *et al*[2].

Unfortunately, M06L is the only meta-GGA actually implemented in CRYSTAL, thus it was not possible to evaluate other promising meta-GGA as SCAN[67] or mBJLDA[68], both well reproducing the band gap of semiconductors. **Figure 9** depicted the computed deviations, while the numerical values are reported in **Table A6**.

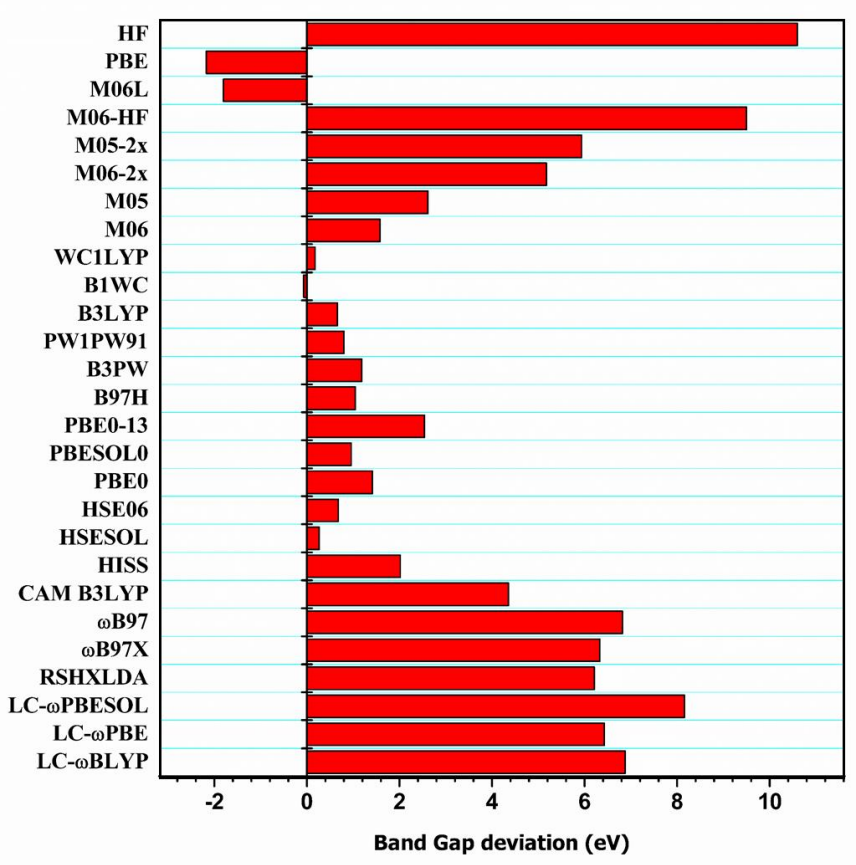

Figure 9. Difference between the computed Ce $4f_{occupied}$ – Ce $4f_{virtual}$ gap and the experimental band gap for Ce_2O_3.

3.3.6 Cohesive Energies

The cohesive energy for a solid is an indicator of the strength of the bonds which hold the atoms together. Here it was simply computed as the difference between the ground electronic energy of the unit cell of the oxides and of the constituent atoms. Since the basis set requirement to correctly describe the isolated atomic phase is higher than for the condensed phase, the basis set of Ce and O (Ce3, O2) have been augmented with all the diffuse contractions present in the original versions of the basis, in order to account for the long-range decay of the wavefunction.

The experimental cohesive energies values have been derived by subtracting the tabulated enthalpy of formation of the oxides from the atomization energy of the alpha-Ce (most stable phase) and the dissociation energy of O_2. **Figure 10** shows the computed deviations, where the numerical results are reported in **Table A7.** While Hartree-Fock largely overestimates the cohesive energy of both the

oxides, most of the other Hamiltonians underestimates the stability of structures, with similar deviations. Few functionals, namely PBEsol0, HSEsol, B1WC and M06L show deviations below 0.04 eV per atom. Except for M06L, the other three XC have been specifically developed to model solids, at the expense of accuracy for molecules: for instance, the O_2 binding energy is overestimated by 0.63, 0.63, 0.76 and 0.03 eV, by PBEsol0, HSEsol, B1WC and M06L respectively. Also, PBE performs rather well, but in this case the deviation for the O_2 binding energy is of 1.05 eV.

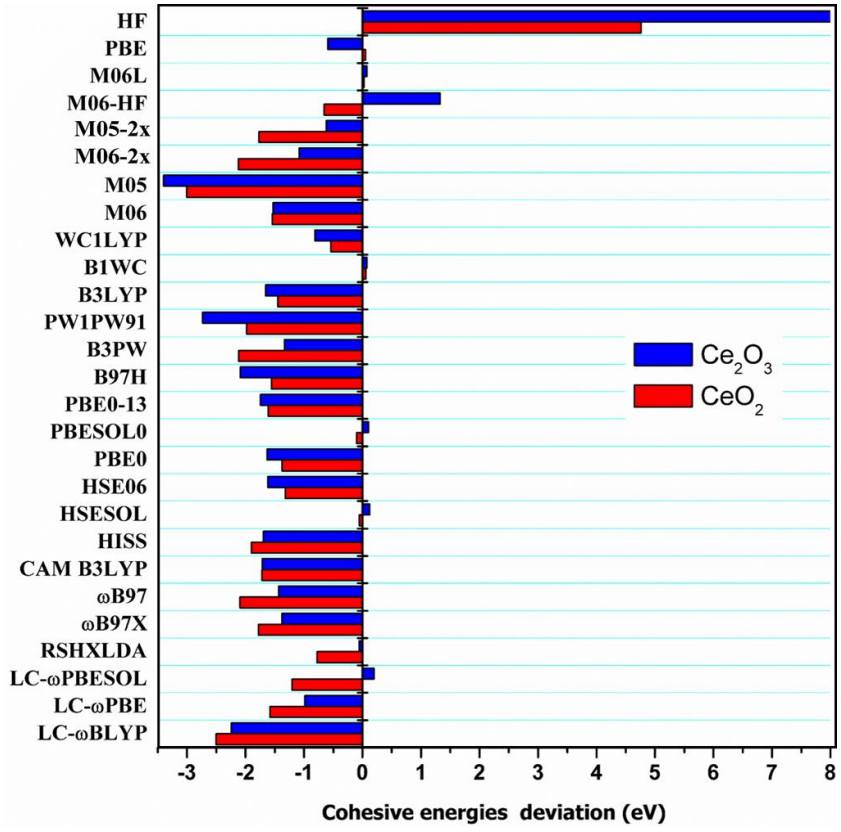

Figure 10. Difference between the computed cohesive energies and the tabulated ones for the two oxides.

3.3.7 Energetics of reduction

In order to assess how the different XCs perform in describing reactions involving the change of oxidation state of the Ce in the oxide, we consider the following simple reactions:

$2CeO_2 \rightarrow Ce_2O_3 + O_2$; $\Delta H = 4.03$ eV (R1)

$2CeO_2 + H_2 \rightarrow Ce_2O_3 + H_2O$; $\Delta H = 1.54$ eV (R2)

R1 is the commonly reported reduction process, however the computed energies may be affected by the XC error in the description of bond strength of the triplet state O_2, therefore we consider also R2 were the molecular species are all closed shells.

Paier *et al* reported in their review[62] small values of zero point vibrational and thermal contribution for the enthalpies of formation of these oxides, as well for the reaction here considered.
Confirming these results, we computed a zero-point correction of -0.08 eV for R1 and of -0.11 eV for R2, with the only PBE0. Thus, for the benchmark we considered only the electronic energies for all the involved species. **Figure 11** reports the deviations from the experimental results for the energetic of the two reactions, while the numerical results are collected in **Table A8.**
The reactions of reduction here considered, in particular R1, are closely related to the process of formation of the oxygen vacancy, which involves the same Ce^{4+}/Ce^{3+} interconversion.
Experimentally is difficult to obtain reliable results for the energy of formation of a single vacancy, which depends on the measurement technique and the sample purity[62]: the best estimate is 4.2 ± 0.3 eV[69], for a bulk phase vacancy, a value close to the 4.03 eV of R1.
Thus, the associated energy of reduction is related to the energy of formation of the vacancy, and likely it represent a upper limit to this process[62]. Therefore, a good esteem of the reduction energy is an expected requisite to reproduce also the formation energy of the vacancy.
The best performer among hybrids, B1WC, underestimates the two reaction energies by about 0.5 eV, while PBE and M06L provide much closer results, with deviations of about +0.05 and - 0.25 eV, respectively.
The good performance of PBE for the energetics of R1 has been considered by De Silva *et al* [42] a fortuitous error cancellation effects, being the other structural and electronic properties of these oxides not satisfactory reproduced.
As observed by Graciani *et al*,[5] the energy of reduction decreases with the increase of the fraction of EE: going from PBE to PBE0 and then to PBE0-13, the energy for R1 decrease from 4.08 eV to 2.69 eV and then to 2.46 eV. The same trend is observed for the energies of R2. The reaction energies correlated with the intra-gap O 2*p* – Ce 4*f* of Ce_2O_3.
To explain these trends, we have considered the effect of the EE on the filled bands of the solid: the intra-gap of O 2*p* - Ce 4*f* in Ce_2O_3 decreases as the weight of the EE increases. The reaction of reduction involves the extraction of a neutral O atom, which leaves in the solid 2 unbound electrons, which occupy the 4*f* states of Ce. The cost for extracting the atom is then associated with the energy required to fill the 4*f* band, rather than to the structural relaxation induced by the process. In the totally reduced Ce_2O_3, the extraction of O involves the transfer of $2e^-$ from the O 2*p* band to the Ce 4*f* valence band. Being the intra-gap directly proportional to the weight of the EE, the process of reduction is systematically favoured by the hybrids with respect to the local functionals. Exceptions are the functionals for which the intra-gap became really small (M05-2x) or zero (M06-HF), for which the dependency reaction energy-intra-gap is reverted.

According to these results, the inclusion of a high fraction of EE worsen the reproduction of the energetics of the reduction.

Graciani *et al* evidenced that the reduction energy can be reproduced by fitting the value of the EE in the XC, in particular for their investigations with PBE0, B3LYP and B1WC this value falls in the range of 10 and 28 %. Considering the bias of their BS towards higher reduction energies of about 0.9-1.0 eV, the optimal value should be in a much lower range. Unfortunately, fitting the EE in these GHs to reproduce the reduction energy would compromise the performance for most of the other properties, as happen with the DFT + U approach[51].

These results show that including the EE in the functional worsen the reproduction of the reduction energies according R1 and R2.

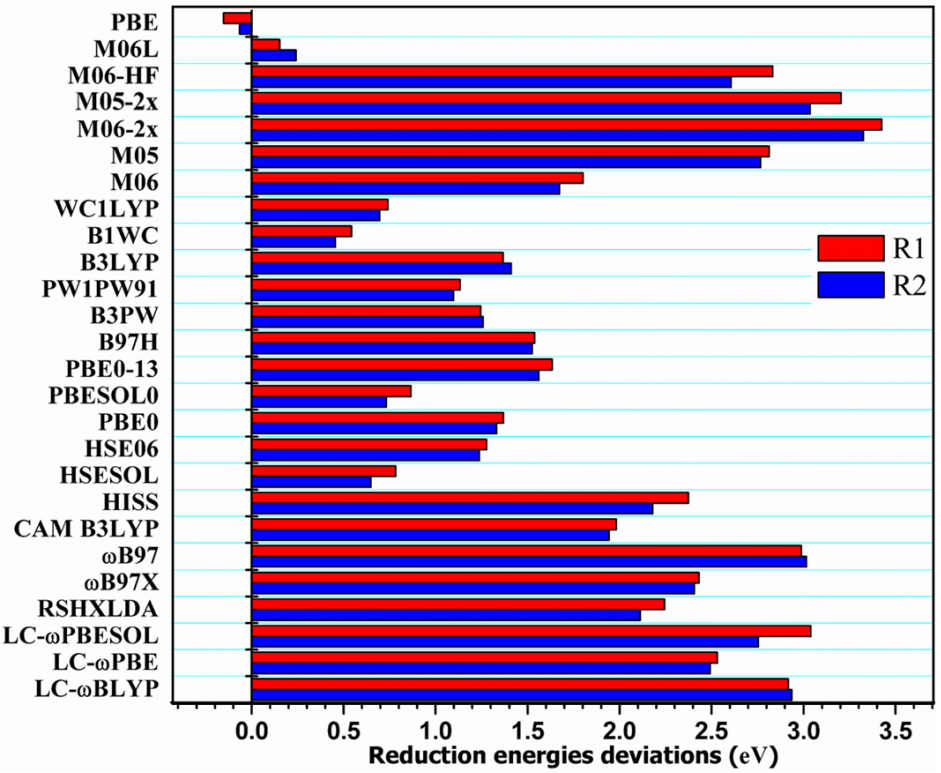

Figure 11. Difference between the computed reaction energies R1 and R2 and the experimental ones.

3.3.8 Vo formation on CeO_2 (111)

In ceria O vacancies (V_O) are the principal type of intrinsic defect, they are practically always present in the samples of the material when they are not prepared and stored at high partial pressure of O_2 (P_{O_2}).

Surface V_O are considered as reactive sites for many processes, acting as nucleophilic sites for oxygenated species and other electron donors. Moreover, an active oxide surface can transfer the O

atoms to a substrate following the Mars van Krevelen mechanism[70], which results in the formation of a surficial V_O and an oxygenated substrate.

The V_O on CeO_2 (111) have been also thoroughly investigated: as in the bulk, the formation of an O vacancy is followed by the reduction of a couple of Ce^{4+} to Ce^{3+} ions, summarized as:

$[2Ce^{4+}, O^{2-}] \rightarrow [2Ce^{3+}, V_O] + ½\ O_2$

When the vacancy forms, the reduction involves supposedly two of the Ce nearest neighbour (NN-NN) to the vacant site, to give the configuration NN-NN of Ce^{3+} ions. This configuration is not necessary the most stable, and calculations both with DFT+U and HSE06 have shown that the configuration with one or two Ce^{3+} in next nearest neighbour position (NNN) with respect to the vacancy are most stable by about 0.2 and 0.5 eV[71] for the configurations NN-NNN and the NNN-NNN, respectively (with variations depending on the supercell size and methodology).

In order to obtain these latter configurations, it is necessary to alter the starting geometry of the pristine CeO_2 (111) or to bias the calculations to localize the 4*f* states on these other sites.

Since the NN-NN configuration is obtained straightforward with our computational protocol, we limit our investigation to vacancy with this configuration of Ce for the XC assessment.

A selection of the best performing functionals includes three GHs with 16, 20 and 25 % of EE, namely B1WC, PW1PW91, PBE0, and the SRH HSE06. Moreover, the M06L, and the PBEsol0 functionals have also been tested, but we have not managed to obtain converged solutions. The **Figure 12** shows the slab model of the surface adopted for the study. We have considered the formation of a surface V_O (V_{OSur}) and of a subsurface one (V_{OSub}), depicted in **Figure 13**.

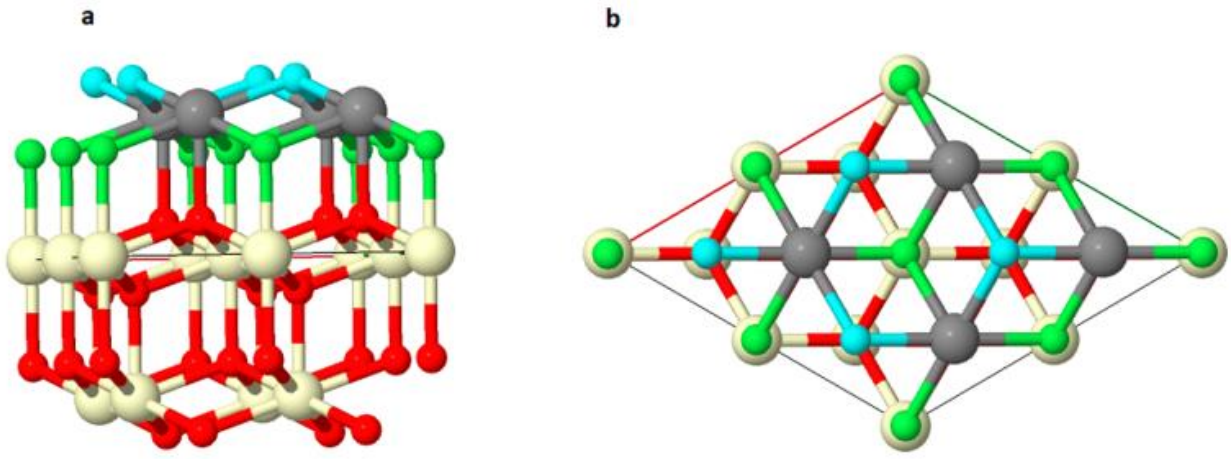

Figure 12. Side (a) and top (b) view of the CeO_2 111 p(2 × 2) slab. The superficial layer of O is represented in light blue, the sub superficial layer of O is represented in light green. Between the two, the Ce layer is represented in gray. The underneath layers of O and Ce are represented in red and white, respectively.

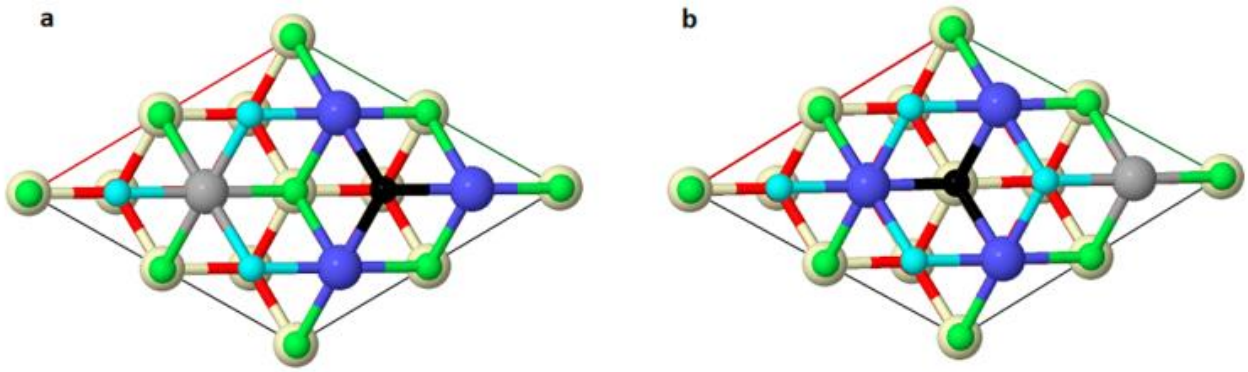

Figure 13. Modeled vacancy in the superficial O layer (a) and in the subsuperficial O layer (b). The vacant O is colored in black for both cases. The three Ce atoms in the first cationic shell of the vacancy (earest neighbors, NNs) are represented in cyan. Ce atoms in the second cationic sphere of the vacancy (next nearest neighbor, NNN) are represented in gray.

To evaluate the performance of the functionals we considered the energy of formation of the vacancies, the degree of spin localization on the Ce^{3+} ions (the magnetization M, derived from Mulliken population analysis), the structural rearrangement around the Ce^{3+} ions (change of the average Ce-O distance), the electronic structure (intra-gap O 2*p* – Ce $4f_{occup}$ and band gap Ce $4f_{occup}$ - Ce $4f_{virtual}$). The main results are summarized in **Table 3**, reported at the end of this section.
All the functionals predict the surface V_O less stable than the subsurface V_O, in agreement with previous calculations at the DFT+U and HSE06 level[62,72,73].
As for the reduction energies discussed in the previous section, also the energy of formation of the oxygen vacancies (E_{fv}) shows a dependence from the weight of the EE, being the highest for B1WC and the smaller for PBE0.
When the Vo forms, the dangling bonds with the neighbouring Ce rearrange to reduce two Ce^{4+} to Ce^{3+}, with the extra electron on semi-occupied 4*f* orbitals. Ce^{3+} then is distinguished from the Ce^{4+} for the atomic spin polarization, which arises entirely from the 4*f* electron. **Table 3** reports the two largest magnetic moments computed from the Mulliken's spin population of the associated to the Ce.
The Ce^{3+} ions are also characterized by a different coordination environment with respect to the Ce^{4+} ions: after reduction, the ionic radius of Ce increases inducing an elongation of the average distances Ce-O, in the first coordination shell. The structural relaxation around the Ce^{3+} ions is then evaluated as the ratio between the average distances Ce-O in the reduced form and in the pristine structure. The relaxation factor evidences a larger relaxation for the structures with the subsurface Vo with respect to the surface Vo case (2.5 % vs 1.8 % for PBE0), which explains the higher stability of the former.

Again, the degree of relaxation decreases as the fraction of EE decrease.

The density of states shows the main electronic structure features of the reduced surfaces: the occupied Ce 4*f* states appears as a narrow band about 0.2 eV wide between the O 2*p* and the Ce 4*f* band gap of the oxide. The intra-gap O 2*p* - Ce 4*f* is the smaller for PBE0 and increase for XC with less EE. The computed band gap 4*f* – 4*f* depends on the fraction of EE and ranges from 1.96 (PBE0) to 0.50 eV (B1WC). Given the dispersion of the experimental data, all these functionals reproduce reasonably well the intra-gap, while the band gap, observed close to 1 eV is best reproduced by HSE06 and PW1PW91. PBE0 overshoot it by about 1 eV and B1WC underestimates it by 0.5 eV or more.

In conclusion, all the tested functionals provide the same relative order of stability for the two Vo, but the degree of relaxation around the Ce^{3+} ions and their spin polarization increase with the weight of the EE in the functional. As shown for the bulk phases, the amount of EE also affects the electronic structure, with the intra-gap O 2*p* – Ce 4*f* occupied which decrease going from the 16% to 25 % while the band gap 4*f* – 4*f* increases. These results suggest that 16 % of EE in B1WC is not enough to well characterize the Ce^{3+} in the sublattice of ceria, even if it performs well for the two pure oxides. The other three functionals have similar performance and provide a better description of the considered properties, even though the formation energies of the defects worsen. PBE0 and HSE06, the two most popular hybrid functionals for solid-state calculations, confirms their reputation. The PW1PW91 is rather similar to PBE0, but with 20% of EE instead of 25%: the smaller amount of EE of this GH mimic the effect of the Coulombic screening of HSE06 on the band gaps (but not on the intra-gap, more sensible to the % of EE at short range), providing then similar values. HSE06 gives overall the best description, but it is less performing with respect to PBE0, with the computational setting adopted, due to a higher cost by a factor 2-3 (see CRYSTAL17 User's manual, range separated hybrids). Overall, for applications on large systems is advisable to use PBE0, at least for geometry optimization.

Table 3: Summary table for the Oxygen vacancies on CeO_2(111). Oxygen vacancy formation energy on surface (E_{gzSurf}) and subsurface (E_{vSub}) positions. With μ Ce^{3+} we indicate the magnetic moment over the formally Ce^{3+}.r̄ (Ce^{3+}-O) is the average distance between Ce^{3+} and the O in its first coordination shell. R_f is the relaxation factor, computed as the ratio between r̄ (Ce^{3+}-O) and the average Ce-O distance in the pristine surface. 2*p* - 4*f* is the gap between the valence O 2*p* states and the occupied Ce 4*f* states, while 4*f* - 4*f* is the gap between the occupied Ce 4*f* states and the conduction empty Ce 4*f* states. The slash divides the data for the two reduced Ce^{3+}.

Method	**Ef_{vSurf} (eV)[a]**	**2*p* - 4*f* (eV)**	**4*f* - 4*f* (eV)**	**μ Ce^{3+} (μ_B)**	**r̄ (Ce^{3+}-O) (Å)[b]**	**R_f**	**E_{vSub} (eV)[a]**	**2*p* - 4*f* (eV)**	**4*f* - 4*f* (eV)**	**μ Ce^{3+} (μ_B)**	**r̄ Ce^{3+}-O (Å)[b]**	**R_f**
PBE0(25)/this work	3.00 (3.10)	1.80	1.96	1.000/0.999	2.374/2.371 (2.330)	1.018	2.77 (2.87)	1.99	1.87	1.000/1.000	2.388/2.387 (2.330)	1.025
HSE06(25, screen)/ this work	3.10 (3.19)	1.89	1.25	0.997/0.996	2.372/2.371 (2.330)	1.018	2.86 (2.96)	1.99	1.17	1.000/1.000	2.387/2.387 (2.330)	1.024
PW1PW91(20)/this work	3.39 (3.56)	2.02	1.26	0.994/0.995	2.364/2.366 (2.335)	1.013	3.04 (3.20)	2.13	1.02	1.000/1.000	2.385/2.385 (2.335)	1.021
B1WC(16) /this work	3.78 (4.15)	2.40	0.55	0.969/0.969	2.347/2.346 (2.323)	1.010	3.63 (4.00)	2.50	0.22	0.962/0.961	2.362/2.363 (2.323)	1.017
HSE06/p(2x2) 3L[42]	3.30		1.0				3.21		0.9			
HSE06/p(4x4)[74]	2.44						2.26					
PBE0/PEECM [75]	3.3(T)[c]		2.5				3.54(T)[c]/3.33(S)[c]		2.2			

a) In brackets: the energies calculated with respect to the ground state energy of O (triplet state) and 1/2 of the experimental binding for O_2 (2.58 eV)[76].
b) In brackets: the average Ce-O distance for the Ce in the 2nd atomic layer of the relaxed pristine surface
c) T and S are respectively Triplet and Singlet spin multiplicity for the ferromagnetic and antiferromagnetic configurations.

3.4 Conclusions

In this chapter, it is discussed the assessment of the performance of several hybrids functional on the properties of the cerium oxides CeO_2 and Ce_2O_3 and on the O defective CeO_2 (111) surface. The effects of the BS of Ce and O has been evaluated at the PBE0 level in order to select the most computationally efficient combination to perform the study. The BS Ce2-O1 emerged as the most balanced to reproduce the structural, the electronic and vibrational properties, but a more accurate evaluation of the thermochemical properties required the use of a larger BS, as the Ce3-O2 combination adopted in this work.

The lattice parameters are reproduced within the 2% of deviation from the experimental values and are mostly affected by the semi-local component of the XC terms. Vibrational and elastic properties are better reproduced by GHs and HSE06, while the family of the Minnesota functionals, and at a lesser extent, the long-range corrected hybrids predict more rigid structures, with higher Bulk modulus.

The % of EE and its spatial partitioning highly affect the band gaps, which are overestimated when the % of EE is higher than 20, excepted for HSE06 and HSEsol.

The reduction energies are also highly affected by the EE, and in general, are underestimated at increasing extent with the weight of the EE. The local PBE and M06L provide the smaller deviations for the reaction energies, but their performance is worse than hybrids for most of the other properties. The study highlights a strong correlation between the computed reduction energies and the intra-gap O 2*p* – Ce 4*f* in the sesquioxide. Overall, the best description of the oxides is obtained by global hybrids with the % of EE between 16 and 25 % and HSE06. From these functionals, we selected B1WC, PW1PW91, PBE0 and HSE06 to model O vacancies on CeO_2 (111). All the functionals reproduce the relative order of stability of the vacancies, but all the properties result highly dependent on the EE amount. The most balanced description for the surface vacancies has been provided by PW1PW91, followed by HSE06. PBE0, even if overestimates the band gaps, it provides structures and energetics almost identical to HSE06, with about the 1/3 of the computational costs, and it has much fewer convergences issues than PW1PW91 when dealing with the surface vacancies, thus we chose it for the successive investigations presented in this thesis.

3.5 References

1. Shao, X., Jerratsch, J.-F., Nilius, N. & Freund, H.-J. Probing the 4f states of ceria by tunneling spectroscopy. *Phys. Chem. Chem. Phys.* **13**, 12646–12651 (2011).
2. Hay, P. J., Martin, R. L., Uddin, J. & Scuseria, G. E. Theoretical study of CeO_2 and Ce_2O_3 using a screened hybrid density functional. *J. Chem. Phys.* **125**, 034712 (2006).
3. Da Silva, J. L. F., Ganduglia-Pirovano, M. V., Sauer, J., Bayer, V. & Kresse, G. Hybrid functionals applied to rare-earth oxides: The example of ceria. *Phys. Rev. B* **75**, (2007).
4. Kullgren, J., Castleton, C. W. M., Müller, C., Ramo, D. M. & Hermansson, K. B3LYP calculations of cerium oxides. *J. Chem. Phys.* **132**, 054110 (2010).
5. Graciani, J. *et al.* Comparative Study on the Performance of Hybrid DFT Functionals in Highly Correlated Oxides: The Case of CeO_2 and Ce_2O_3. *J. Chem. Theory Comput.* **7**, 56–65 (2011).
6. Dovesi, R. *et al.* CRYSTAL14: A program for the ab initio investigation of crystalline solids. *Int. J. Quantum Chem.* **114**, 1287–1317 (2014).
7. Yanai, T., Tew, D. P. & Handy, N. C. A new hybrid exchange–correlation functional using the Coulomb-attenuating method (CAM-B3LYP). *Chem. Phys. Lett.* **393**, 51–57 (2004).
8. Dovesi, R. *et al.* Quantum-mechanical condensed matter simulations with CRYSTAL. *Wiley Interdiscip. Rev. Comput. Mol. Sci.* e1360 (2018) doi:10.1002/wcms.1360.
9. Perdew, null, Burke, null & Ernzerhof, null. Generalized Gradient Approximation Made Simple. *Phys. Rev. Lett.* **77**, 3865–3868 (1996).
10. Zhao, Y. & Truhlar, D. G. A new local density functional for main-group thermochemistry, transition metal bonding, thermochemical kinetics, and noncovalent interactions. *J. Chem. Phys.* **125**, 194101 (2006).
11. Zhao, Y., Schultz, N. E. & Truhlar, D. G. Exchange-correlation functional with broad accuracy for metallic and nonmetallic compounds, kinetics, and noncovalent interactions. *J. Chem. Phys.* **123**, 161103 (2005).
12. Zhao, Y., Schultz, N. E. & Truhlar, D. G. Design of Density Functionals by Combining the Method of Constraint Satisfaction with Parametrization for Thermochemistry, Thermochemical Kinetics, and Noncovalent Interactions. *J. Chem. Theory Comput.* **2**, 364–382 (2006).
13. Zhao, Y. & Truhlar, D. G. The M06 suite of density functionals for main group thermochemistry, thermochemical kinetics, noncovalent interactions, excited states, and transition elements: two new functionals and systematic testing of four M06-class functionals and 12 other functionals. *Theor. Chem. Acc.* **120**, 215–241 (2008).

14. D. Becke, A. Density-Functional Thermochemistry. III. The Role of Exact Exchange. *J Chem Phys* **98**, 5648–5653 (1993).
15. Perdew, J. P. & Yue, W. Accurate and simple density functional for the electronic exchange energy: Generalized gradient approximation. *Phys. Rev. B* **33**, 8800 (1986).
16. Adamo, C. & Barone, V. Toward reliable density functional methods without adjustable parameters: The PBE0 model. *J. Chem. Phys.* **110**, 6158–6170 (1999).
17. Guido, C. A., Brémond, E., Adamo, C. & Cortona, P. Communication: One third: A new recipe for the PBE0 paradigm. *J. Chem. Phys.* **138**, 021104 (2013).
18. Perdew, J. P. *et al.* Restoring the Density-Gradient Expansion for Exchange in Solids and Surfaces. *Phys. Rev. Lett.* **100**, (2008).
19. Bredow, T. & Gerson, A. R. Effect of exchange and correlation on bulk properties of MgO, NiO, and CoO. *Phys. Rev. B* **61**, 5194 (2000).
20. Demichelis, R., Civalleri, B., Ferrabone, M. & Dovesi, R. On the performance of eleven DFT functionals in the description of the vibrational properties of aluminosilicates: Performance of Eleven DFT Functionals. *Int. J. Quantum Chem.* **110**, 406–415 (2010).
21. Chai, J.-D. & Head-Gordon, M. Systematic optimization of long-range corrected hybrid density functionals. *J. Chem. Phys.* **128**, 084106 (2008).
22. Hamprecht, F. A., Cohen, A. J., Tozer, D. J. & Handy, N. C. Development and assessment of new exchange-correlation functionals. *J. Chem. Phys.* **109**, 6264–6271 (1998).
23. Bilc, D. I. *et al.* Hybrid exchange-correlation functional for accurate prediction of the electronic and structural properties of ferroelectric oxides. *Phys. Rev. B* **77**, (2008).
24. Krukau, A. V., Vydrov, O. A., Izmaylov, A. F. & Scuseria, G. E. Influence of the exchange screening parameter on the performance of screened hybrid functionals. *J. Chem. Phys.* **125**, 224106 (2006).
25. Schimka, L., Harl, J. & Kresse, G. Improved hybrid functional for solids: The HSEsol functional. *J. Chem. Phys.* **134**, 024116 (2011).
26. Henderson, T. M., Izmaylov, A. F., Scuseria, G. E. & Savin, A. Assessment of a Middle-Range Hybrid Functional. *J. Chem. Theory Comput.* **4**, 1254–1262 (2008).
27. Henderson, T. M., Izmaylov, A. F., Scuseria, G. E. & Savin, A. The importance of middle-range Hartree-Fock-type exchange for hybrid density functionals. *J. Chem. Phys.* **127**, 221103 (2007).
28. Vydrov, O. A. & Scuseria, G. E. Assessment of a long-range corrected hybrid functional. *J. Chem. Phys.* **125**, 234109 (2006).

29. Weintraub, E., Henderson, T. M. & Scuseria, G. E. Long-Range-Corrected Hybrids Based on a New Model Exchange Hole. *J. Chem. Theory Comput.* **5**, 754–762 (2009).

30. Vosko, S. H., Wilk, L. & Nusair, M. Accurate spin-dependent electron liquid correlation energies for local spin density calculations: a critical analysis. *Can. J. Phys.* **58**, 1200–1211 (1980).

31. Gerber, I. C. & Ángyán, J. G. London dispersion forces by range-separated hybrid density functional with second order perturbational corrections: The case of rare gas complexes. *J. Chem. Phys.* **126**, 044103 (2007).

32. Becke, A. D. Density-functional thermochemistry. V. Systematic optimization of exchange-correlation functionals. *J. Chem. Phys.* **107**, 8554–8560 (1997).

33. Yanai, T., Tew, D. P. & Handy, N. C. A new hybrid exchange-correlation functional using the Coulomb-attenuating method (CAM-B3LYP). *Chem. Phys. Lett.* **393**, 51–57 (2004).

34. Dolg, M., Stoll, H., Savin, A. & Preuss, H. Energy-adjusted pseudopotentials for the rare earth elements. *Theor. Chem. Acc. Theory Comput. Model. Theor. Chim. Acta* **75**, 173–194 (1989).

35. Graciani, J. *et al.* Comparative Study on the Performance of Hybrid DFT Functionals in Highly Correlated Oxides: The Case of CeO_2 and Ce_2O_3. *J. Chem. Theory Comput.* **7**, 56–65 (2011).

36. Cao, X. & Dolg, M. Segmented contraction scheme for small-core lanthanide pseudopotential basis sets. *J. Mol. Struct. THEOCHEM* **581**, 139–147 (2002).

37. Thakkar, A. J., Koga, T., Saito, M. & Hoffmeyer, R. E. Double and quadruple zeta contracted gaussian basis sets for hydrogen through neon. *Int. J. Quantum Chem.* **48**, 343–354 (1993).

38. Peintinger, M. F., Oliveira, D. V. & Bredow, T. Consistent Gaussian basis sets of triple-zeta valence with polarization quality for solid-state calculations. *J. Comput. Chem.* **34**, 451–459 (2013).

39. Pinto, H., Mintz, M. H., Melamud, M. & Shaked, H. Neutron diffraction study of Ce_2O_3. *Phys. Lett. A* **88**, 81–83 (1982).

40. Perger, W. F., Criswell, J., Civalleri, B. & Dovesi, R. Ab-initio calculation of elastic constants of crystalline systems with the CRYSTAL code. *Comput. Phys. Commun.* **180**, 1753–1759 (2009).

41. Erba, A., Mahmoud, A., Orlando, R. & Dovesi, R. Elastic properties of six silicate garnet end members from accurate ab initio simulations. *Phys. Chem. Miner.* **41**, 151–160 (2014).

42. Ganduglia-Pirovano, M. V., Da Silva, J. L. F. & Sauer, J. Density-Functional Calculations of the Structure of Near-Surface Oxygen Vacancies and Electron Localization on CeO_2 (111). *Phys. Rev. Lett.* **102**, (2009).

43. Torbrügge, S., Reichling, M., Ishiyama, A., Morita, S. & Custance, Ó. Evidence of Subsurface Oxygen Vacancy Ordering on Reduced CeO_2 (111). *Phys. Rev. Lett.* **99**, (2007).

44. Gerward, L. *et al.* Bulk modulus of CeO_2 and PrO_2—An experimental and theoretical study. *J. Alloys Compd.* **400**, 56–61 (2005).

45. Duclos, S. J., Vohra, Y. K., Ruoff, A. L., Jayaraman, A. & Espinosa, G. P. High-pressure x-ray diffraction study of CeO_2 to 70 GPa and pressure-induced phase transformation from the fluorite structure. *Phys. Rev. B* **38**, 7755 (1988).

46. Rossignol, S., Gérard, F., Mesnard, D., Kappenstein, C. & Duprez, D. Structural changes of Ce–Pr–O oxides in hydrogen: a study by in situ X-ray diffraction and Raman spectroscopy. *J. Mater. Chem.* **13**, 3017–3020 (2003).

47. Kullgren, J., Castleton, C. W. M., Müller, C., Ramo, D. M. & Hermansson, K. B3LYP calculations of cerium oxides. *J. Chem. Phys.* **132**, 054110 (2010).

48. Evarestov, R. A. *et al.* Use of site symmetry in supercell models of defective crystals: polarons in CeO_2. *Phys. Chem. Chem. Phys.* **19**, 8340–8348 (2017).

49. Désaunay, T., Ringuedé, A., Cassir, M., Labat, F. & Adamo, C. Modeling basic components of solid oxide fuel cells using density functional theory: Bulk and surface properties of CeO_2. *Surf. Sci.* **606**, 305–311 (2012).

50. Nakajima, A., Yoshihara, A. & Ishigame, M. Defect-induced Raman spectra in doped CeO_2. *Phys. Rev. B* **50**, 13297 (1994).

51. Castleton, C. W. M., Kullgren, J. & Hermansson, K. Tuning LDA+U for electron localization and structure at oxygen vacancies in ceria. *J. Chem. Phys.* **127**, 244704 (2007).

52. Weber, W. H., Hass, K. C. & McBride, J. R. Raman study of CeO_2: Second-order scattering, lattice dynamics, and particle-size effects. *Phys. Rev. B* **48**, 178–185 (1993).

53. Kourouklis, G. A., Jayaraman, A. & Espinosa, G. P. High-pressure Raman study of CeO_2 to 35 GPa and pressure-induced phase transformation from the fluorite structure. *Phys. Rev. B* **37**, 4250–4253 (1988).

54. Zinkevich, M., Djurovic, D. & Aldinger, F. Thermodynamic modelling of the cerium–oxygen system☆. *Solid State Ion.* **177**, 989–1001 (2006).

55. Pinto, H., Mintz, M. H., Melamud, M. & Shaked, H. Neutron diffraction study of Ce_2O_3. *Phys. Lett. A* **88**, 81–83 (1982).

56. Bärnighausen, H. & Schiller, G. The crystal structure of A-Ce_2O_3. *J. Common Met.* **110**, 385–390 (1985).

57. Lipp, M. J. *et al.* Comparison of the high-pressure behavior of the cerium oxides Ce_2O_3 and CeO_2. *Phys. Rev. B* **93**, (2016).

58. Prokofiev, A. V., Shelykh, A. I. & Melekh, B. T. Periodicity in the band gap variation of Ln_2X_3 (X= O, S, Se) in the lanthanide series. *J. Alloys Compd.* **242**, 41–44 (1996).

59. Adachi, G. & Imanaka, N. The Binary Rare Earth Oxides. *Chem. Rev.* **98**, 1479–1514 (1998).

60. Avisar, D. & Livneh, T. The Raman-scattering of A-type Ce_2O_3. *Vib. Spectrosc.* **86**, 14–16 (2016).

61. Garza, A. J. & Scuseria, G. E. Predicting band gaps with hybrid density functionals. *J. Phys. Chem. Lett.* **7**, 4165–4170 (2016).

62. Paier, J., Penschke, C. & Sauer, J. Oxygen Defects and Surface Chemistry of Ceria: Quantum Chemical Studies Compared to Experiment. *Chem. Rev.* **113**, 3949–3985 (2013).

63. Vayssilov, G. N., Mihaylov, M., Petkov, P. St., Hadjiivanov, K. I. & Neyman, K. M. Reassignment of the Vibrational Spectra of Carbonates, Formates, and Related Surface Species on Ceria: A Combined Density Functional and Infrared Spectroscopy Investigation. *J. Phys. Chem. C* **115**, 23435–23454 (2011).

64. Schilling, C., Hofmann, A., Hess, C. & Ganduglia-Pirovano, M. V. Raman Spectra of Polycrystalline CeO_2: A Density Functional Theory Study. *J. Phys. Chem. C* **121**, 20834–20849 (2017).

65. Perdew, J. P. *et al.* Understanding band gaps of solids in generalized Kohn–Sham theory. *Proc. Natl. Acad. Sci.* **114**, 2801–2806 (2017).

66. Jiang, H., Rinke, P. & Scheffler, M. Electronic properties of lanthanide oxides from the G W perspective. *Phys. Rev. B* **86**, (2012).

67. Sun, J., Remsing, R. C., Zhang, Y. & Sun, Z. SCAN: An Efficient Density Functional Yielding Accurate Structures and Energies of Diversely-Bonded Materials. 19.

68. Tran, F. & Blaha, P. Accurate Band Gaps of Semiconductors and Insulators with a Semilocal Exchange-Correlation Potential. *Phys. Rev. Lett.* **102**, (2009).

69. Gorte, R. J. Ceria in catalysis: From automotive applications to the water–gas shift reaction. *AIChE J.* **56**, 1126–1135 (2010).

70. Mars, P. & van Krevelen, D. W. Oxidations carried out by means of vanadium oxide catalysts. *Chem. Eng. Sci.* **3**, 41–59 (1954).

71. Ganduglia-Pirovano, M. V. Oxygen Defects at Reducible Oxide Surfaces: The Example of Ceria and Vanadia. in *Defects at Oxide Surfaces* (eds. Jupille, J. & Thornton, G.) vol. 58 149–190 (Springer International Publishing, 2015).

72. Li, H.-Y. *et al.* Multiple configurations of the two excess 4 f electrons on defective CeO_2 (111) : Origin and implications. *Phys. Rev. B* **79**, (2009).

73. Murgida, G. E. & Ganduglia-Pirovano, M. V. Evidence for subsurface ordering of oxygen vacancies on the reduced CeO_2 (111) surface using density-functional and statistical calculations. *Phys. Rev. Lett.* **110**, 246101 (2013).

74. Paier, J., Penschke, C. & Sauer, J. Oxygen Defects and Surface Chemistry of Ceria: Quantum Chemical Studies Compared to Experiment. *Chem. Rev.* **113**, 3949–3985 (2013).

75. Burow, A. M., Sierka, M., Döbler, J. & Sauer, J. Point defects in CaF_2 and CeO_2 investigated by the periodic electrostatic embedded cluster method. *J. Chem. Phys.* **130**, 174710 (2009).

76. Haynes, W. M. CRC Handbook of Chemistry and Physics. 2643.

Chapter 4: Enhanced reducibility of CeO_2 (111) by doping with Cu and Ag

4.1 Introduction

One of the simplest ways to alter the functionality of ceria is by replacing cerium with a small concentration of different cations. The modifications depend on the different characteristics of the dopants, such as size, valence, ionization potential, etc[1].

The concentration of the modifier ions largely affects the final properties: if too high, the original lattice of ceria is lost, and mixed phases appear.

The major interest in modified ceria is to modulate the O mobility and the oxygen storage capability; both properties correlated with the material reducibility and the energy of formation of O vacancies (V_O).

The key step in ceria activation is the formation of an active V_O: in order to improve the catalytic activity is necessary to understand how dopant cations (or modifiers) affect the energetic of formation of the V_O[2].

To be effective as an oxidation catalyst, the cost to form the vacancy should be small enough to have the transfer of the O, but not too small, otherwise the formed vacancy would not be reactive enough for the processes of healing, compromising the oxygen buffer activity[3,4].

Another critical aspect is the dynamical modification of the catalyst surface under operative conditions: the mobility of the modifier should be as limited as possible, to avoid particle aggregation, or bulk segregation, with consequent loss of the original activity.

The choice of a suitable dopant also depends on the availability, as well as on the market price and the forecast demand for its use. Platinum and other precious metals are mostly employed for catalytic applications, therefore is advisable in the development of new catalytic materials to minimize the use of these elements, or if possible, substitute them with less precious ones[5].

For instance, coinage metals such as Cu and Ag have shown promising performance when used as dopant with ceria to catalyse the oxidation of CH_4 and H_2[6]. Their effect as catalysts towards the oxidation of H_2 has been recently rationalized by the PBE+U investigation of Righi *et al*[7].

In this chapter it is reported the results of our hybrid DFT investigation on the effects of the Cu and Ag doping of CeO_2(111) on the reducibility of the oxide and the comparison with the experimental findings of Gasperi, Valeri and Luches[8].

4.2 Model and computational details

To model the ceria 111 surface, we have adopted a periodic slab model of the supercell p (2x2), with a thickness corresponding to 2 monolayers (see **Figure 1**). Doping has been achieved by replacing Ce with Cu or Ag.

Both the thickness of the slab and the concentration of the dopants (12.5 % of the cations) have been chosen to reproduce the experimental ones.

In the experimental studies, doped and undoped ceria films have been supported over Pt (111). In order to reduce the computational costs and to avoid the bias of an inaccurate description of the interphase, we neglected the Pt support from our model. In fact, the match of the lattice for the metal and oxide surfaces requires the use of supercells with periodicity 4x4 and 3x3 for Pt (111) and CeO_2 (111), respectively. In addition, the hybrid functionals on the metallic phase are less accurate in describing the metallic phase than the insulant phase[9], due to the erroneous description of the metals by the Hartree-Fock theory.[10]

All calculations have performed with the code CRYSTAL17[11]. The exchange-correlation functional PBE0[12] have been employed in the spin-polarized implementation. Cu has been described by a all-electron GTO basis set considering a (21s13p5d)/[6s5p2d] contraction scheme[13], while for Ag, the $4s^2 4p^6 5s^1 4d^{10}$ electrons have been explicitly treated, considering a (6s5p5d)/[4s3p2d] contraction scheme[14], the remaining core electrons being described by an ECP[15]. For Ce and O the same basis sets identified in chapter 3 as Ce2 and Ce3 and O1 and O2 have been used.

The same computational approach followed for the vacancies studies of chapter 3 has been adopted: geometry optimizations have been performed with the small basis set combination Ce2-O1, while total energies have been computed form single points calculations with the larger basis set combination Ce3-O2.

To model the O vacancies, ghost atoms constituted by the same GTO atoms of the removed O, but without charges, has been adopted. The reciprocal space of the cell has been sampled with a Monkhorst-Pack net with a shrinking factor of 6 along the periodic directions, corresponding to 20 k points in the irreducible Brillouin zone. DFT integration has been performed numerically considering 75 radial points and 974 radial points of the default integration grid.

To evaluate the Coulomb and exchange infinite lattice series, threshold values of 8, 8, 8, 8, 20 for the truncations of the relative integrals has been adopted (see User's manual Crystal17). For all the calculations, a tolerance o 10^{-7} a.u. has been adopted on the convergence of the electronic energies during the self-consistent procedure. The geometry optimization has been considered achieved when all the default convergence thresholds for the maximum and root mean squared atomic forces

and gradients were simultaneously reached. Lattice parameters have been fixed to the optimized ceria bulk values (a=5.402 Å), while all the atomic layers have been relaxed during the geometry optimization.

Mulliken's analysis has been adopted to compute atomic charges and spin populations. Spin density maps have been used to visualize the localization of the unpaired electrons.

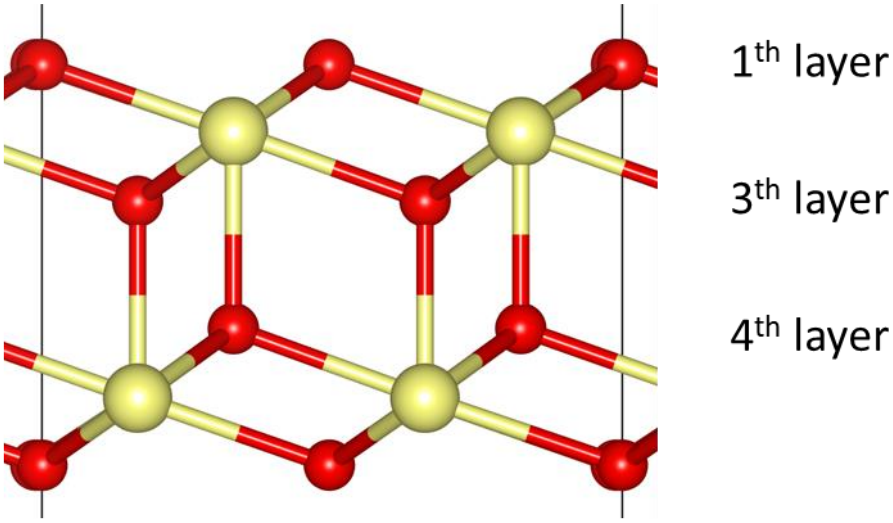

Figure 1. Side view of the clean CeO_2 (111) slab with labelled O layers called in Table 2.

4.3 Results and discussion

4.3.1 Pure CeO_2 surface.

On the pristine ceria surface, the vacancy was modelled in the 1th atomic layer, with an E_{fv} of 2.87 eV. This value is in close agreement with the 2.97 eV obtained on a thicker slab of 3 monolayers. The computed reaction energies are reported

Even if the subsurface V_O (in the 3rd layer) is slightly more stable (see chapter 3) compared to the surface one, the latter is a better reference, being the surface vacancy in the doped surface more stable than the subsurface one. Moreover, it is expected that in a reduction process, the vacancy form at the surface site, and only after it migrates to the subsurface position. For the reduced Ce^{3+} we obtained the NN-NN configuration. Moreover, we consider only the ferromagnetic alignment of the magnetic centres, being quasi-degenerate with the antiferromagnetic one. **Figure 2** reports the spin density map of the defective slab (a), evidencing the magnetic centres Ce^{3+} around the defect site, and the associated density of states (b), where the occupied 4*f* states under the Fermi level are well resolved in between the gap of the oxide.

Table 1. Energy of formation for the first (E_f V1) and second (E_f V2) O vacancy in the surface layer for the pure and modified CeO_2 (111). The values were computed using the PBE0 energy for the isolated O_2 molecule in the triplet state. M3 and M1 are referred to the cell's magnetization with 3 and 1 unpaired electrons, respectively.

System	Ef V1 (eV)	Ef V2 (M3) (eV)	Ef V2 (M1) (eV)
CeO_2	2.87	-	-
$Cu_{0.125}Ce_{0.875}O_2$	-1.40	2.44	2.04
$Ag_{0.125}Ce_{0.875}O_2$	-1.36	2.05	0.56

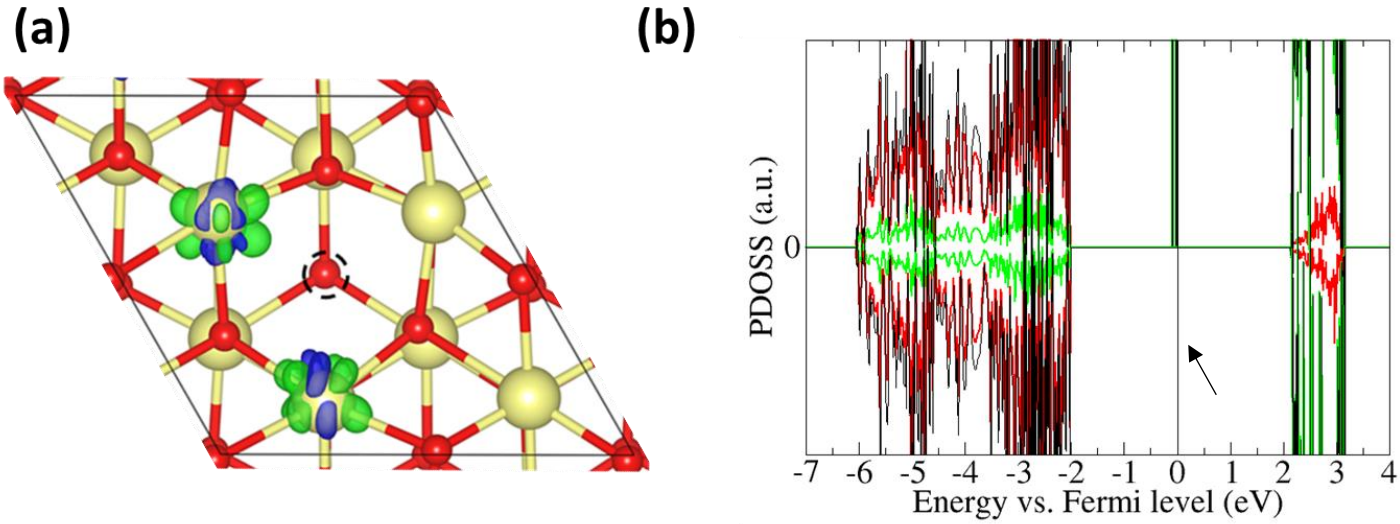

Figure 2. a) Spin density map of CeO_2(111) p(2x2) with a surface oxygen vacancy V_O (black dotted circle). Ce and O atoms are in ivory and red, respectively. The spin density (green and blue isocontour) is localized on the 4*f* states of two Ce^{3+} adjacent to the vacancy. b) Projected density of states for CeO_2(111) p(2x2) with a surface V_O. In red, green and black are respectively the O, the Ce and the total projected states. The arrow points the occupied 4*f* states associated to the two reduced Ce ions.

4.3.2. Cation modified surface.

By replacing one of the Ce in the 2nd atomic layer with the dopant the stoichiometry $X_{0.125}Ce_{0.875}O_2$ is obtained (X= Cu or Ag).

Since both Cu and Ag have an odd number of electrons, their substitution to a Ce forms an open shell system. Moreover, since the dopants have a lower valence (1 or 2) compared to Ce, dangling bonds between the dopants and the neighbouring O form. The density of states for the Cu and Ag modified systems (**Figure 3**, panels a and b) highlights a narrow empty band of O 2*p* character 2 eV above the valence band edge (VBE). The spin density maps (**Figure 4**, panels a and b) enlightened the position of the holes: two lone α electrons localize on the O 2*p* orbitals of two O nearest neighbour of the modifier. These ions are formally $*O^-$ species , with an associated spin population of about 1 μ_B each.

Moreover, they protrude from the surface with respect to the O atoms on the clean surface of 0.26/0.43 Å for Ag and of 0.44/0.42 Å for Cu.

The sum of the spin population on the remaining oxygen coordinated to the dopants and on the dopant itself is close to 1 μ_B, in agreement with the paramagnetic nature of the d^9 ions Ag^{2+} and Cu^{2+}. Overall the modified slabs contain 3 unpaired electrons each.

Structurally, Ag and Cu behave quite differently: **Table 2** reports the computed interatomic distance between the metal centres and the nearest neighbour oxygen atoms. The structures for the modified pristine surface are reported in appendix (**Figure A 4.1**).

Table 2. Metal-oxygen (Me-O) distances in the first-coordination shell of Ce in the pure and cation modified (Ag, Cu) surfaces. V1 and V2 stand for the single and double O vacancy, respectively. M3 and M1 are referred to the cell's magnetization with 3 and 1 unpaired electrons, respectively.

System	Me-O first layer (Å)	Me-O third layer (Å)	Me-O fourth layer (Å)
CeO_2 pristine	2.339; 2.339; 2.339	2.345; 2.345; 2.345	2.266
Ag-modified pristine	2.269; 2.639; 3.284	2.246; 2.281; 2.380	2.590
Ag-modified V1	2.171; 2.899	2.158: 2.313; 2.361	2.593
Ag-modified V2 M1	2.291	2.505; 2.537; 2.237	2.572
Ag-modified V2 M3	2.061	2.322; 2.311; 2.228	2.521
Cu-modified pristine	2.049; 3.609; 3.781	1.936; 1.935 3.128	1.952
Cu-modified V1	2.663; 3.679	1.948; 1933; 3.131	1.962
Cu-modified V2 M1	3.668	1.878; 1.894; 2.952	2.199
Cu-modified V2 M3	3.621	2.196; 1.925; 1.887	1.909

The Ag occupies the Ce lattice position, inducing minor relaxation of the distances Ag-O in the 3rd and in the 4th atomic layers, while the largest displacements are for the two $*O^-$ in the 1st layer. The coordination number of the Ag decreases upon relaxation from 7 to 5.

The Cu, instead, moves towards the 3rd atomic layer, preferring a distorted square planar coordination with an O of the 1st layer, two from the 3rd and 1 from the 4th.

This difference structural behaviour is explained by the different ionic radius of the involved cations: Ag^{2+}, being larger is trapped in the Ce reticular position, while the smaller Cu^{2+} is more mobile. According to previous investigations, the nearest neighbour sites to the modifier are the most favourite sites for the formation of a V_O, which acts as seed for the formation of vacancies. For both the modified slabs, the site selected to form the V_O is the $*O^-$ farther from the dopant, coordinated to only two Ce.

In the DOSS of the two systems the holes associated to the O 2*p* states disappear.

The E_{fv} are in both cases exothermic, -1.40 and -1.36 eV for the Ag and Cu, respectively. The first effect of the doping is to induce the spontaneous formation of a V_O to compensate the different

valence of Ce and the dopants. Similar findings have been obtained in other PW study, which limited the study to the first V_O[3,7].

Being our interest to evaluate the effects of the doping on the formation of an active V_O, a second vacancy at NN position with respect to the dopant, in the 1st layer, has been formed.

Two distinct solutions for both the Ag and Cu doped systems have been found, called here M_1 and M_3, characterized by a different cell magnetization of 1.00 and 3.00 μ_B.

M_3 contains three magnetic centres, two Ce^{3+} and the dopant (**Figure 4**, panels d and h), while in M_1 there is a single Ce^{3+} as magnetic centre (**Figure 4**, panels c and g).

The DOSS of the M_3 solutions are characterized by the presence of two distinct occupied Ce 4*f* bands, absent in the systems with a single vacancy.

For the M_1 solutions, instead, a single occupied narrow Ce 4*f* band appears, while the *d* states of the dopant disappear from the conduction and reappear in a double occupied sharp band (α and β) just above the top of the O 2*p* valence band.

In all cases the cost to form the vacancy is positive and lower than on the clean CeO_2 surface, but the magnitude depends by the oxidation state of the products. In particular the M_1 solutions are favoured with respect to the M_3 ones.

While for the Cu modified surfaces the difference is only by 0.39 eV, for the Ag modified surface it is of 1.48 eV. An easy interpretation of these difference can be given from the ionization energies (IEs) of the involved species: the 2nd IE of Ag (21.490 eV) is 1.3 eV higher than the 3rd IE of Ce (20.198 eV), therefore the solution with 1 Ce^{3+} and Ag^+ is favoured with respect to the one with 2 Ce^{3+} and Ag^{2+}.

Instead the 2nd IE of Cu (20.292 eV) is only 0.1 eV larger than the 3rd IE of Ce, making the oxidation state of Ce and Cu much more sensible to the coordination environment with respect to the Ag-Ce couple.

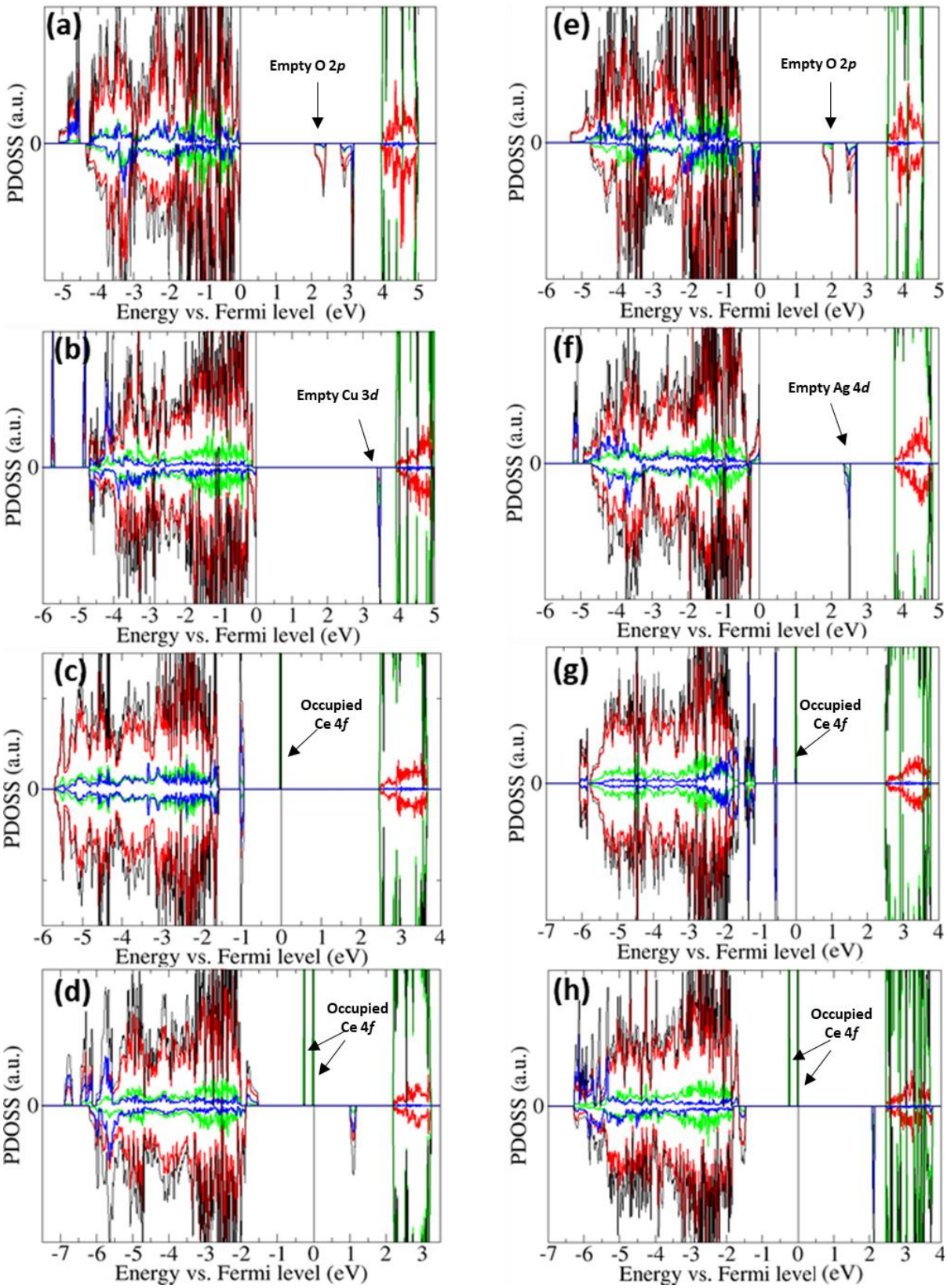

Figure 3. Density of states of (a) pristine Cu-doped CeO_2(111) (b) Cu-doped single vacancy (c) Cu-doped double vacancy (M1) (d) Cu- doped double vacancy (M3) (e) pristine Ag-doped CeO_2(111); (f) Ag- modified, single vacancy; (g) Ag- modified double vacancy (M1); (h) Ag- modified double vacancy (M3). In addition to the color code of Figure 5, here the projected states of the modifier are in blue.

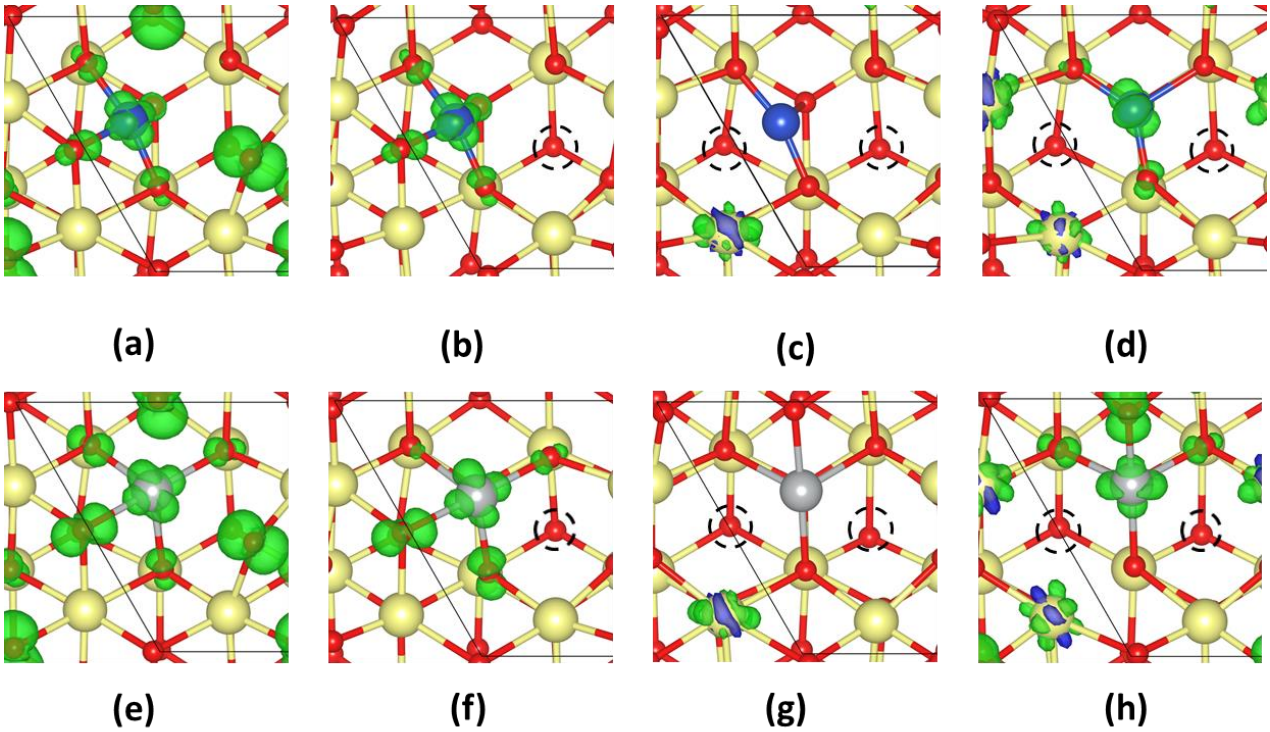

Figure 4. Spin polarization of (a) pristine Cu-modified CeO_2(111) (b) Cu-modified single vacancy (c) Cu-modified double vacancy (M1) (d) Cu-modified double vacancy (M3) (e) pristine Ag-modified CeO_2(111)**;** (f) Ag-modified, single vacancy; (g) Ag-modified double vacancy (M1); (h) Ag-modified double vacancy (M3).

4.3.3 Comparison with the experimental findings

Films of ceria clean and modified with Ag and Cu have been prepared and characterized by Gabriele Gasperi Sergio Valeri and Paola Luches. The films have been grown on a single crystal of Pt (111) by evaporating metallic cerium with a background O_2 pressure. Ag and Cu modified sample have been prepared by evaporating them together with the Ce. The films obtained have a nominal thickness of 2ML.

The purpose in the use of films of sub-nanometric thickness is to obtain relevant concentration of Ce^{3+} ions (higher $Ce^{3+/}Ce^{4+}$ ratio) during the thermal treatment, to facilitate the quantification.

The modified films contained about the 13% in atoms of modifier. Each sample has been subjected to the same redox cycle: first two reduction step at 250 and 500 °C in UHV of 15 minutes each, then a single oxidation step at 500°C in pressure of O_2 (10^{-7} Torr). After each step the samples have been cooled down to RT and subjected to XPS (X-ray photoelectron spectroscopy) and LEED (low energy electron diffraction) measurements in situ. The shift in the 3*d* emission peak measured with XPS were used to distinguish and quantify the Ce^{3+} from Ce^{4+}.

The same approach was used to try to obtain information of the oxidation state of the modifiers, by measuring the Ag 3*d* and the Cu 2*p* XPS spectra.

LEED measurements have been used to investigate the surface evolution during the treatment. No relevant differences were found between the clean and the modified surfaces, indicating the absence of intermediated phases formed by the modifiers. Further details can be found in the related paper[8].
The XPS measurements indicated that the +1 oxidation state for Ag and Cu is dominant also at room temperature (rt), before reducing treatment. This may be explained if the active oxygen vacancies can form also in mild conditions as at rt, or, more probably, by an electron transfer from the Pt (111) support to the dopants. The latter hypothesis is reasonable in view of the XPS results obtained by Gupta *et al*[16] on the powders of Cu-doped ceria, without metallic support: they found the dominance of the +2 oxidation state of Cu for the oxidise samples, while after reduction signals of a mixed valence are observed.
The reducibility, measured as concentration of Ce^{3+}, increases with the T and it is the highest for the Ag modified surface at 500°C, while for the Cu modified surface is the highest at lower T, but considering the error bar the distinction is not sharp (see reference 8).
The concentration of the modifier ions has been revealed to be dynamic, with variation during thermal treatment: the Ag overall concentration does not change, but a mild tendency to segregate towards the surface layer during the re-oxidation step has been observed. Instead, the Cu concentration decreases steadily during the reduction steps, from the 13 % initial to about 5%. The most accredited explanation is the migration of Cu in the deeper layers, with possible formation of an alloy with the Pt support.
Our statistic simulations did not consider thermal effects or ion mobility, but the different tendencies of the Ag and Cu to diffuse towards surface or the bulk, respectively, can be deduced simply by considering the different Me-O bond distance, reported in **Table 2** and by the different ionic radius.

4.4 Conclusions

In the present work, the reducibility of ceria surface (111), clean and modified with Ag and Cu atoms has been investigated. Doping ceria with lower valence cations greatly reduces the cost to form an oxygen vacancy due to the formation of holes states (O 2*p*) on the top of the valence band edge, more easily filled than the Ce 4*f* states[17]. With Cu and Ag doped ceria, the first O vacancy forms spontaneously, without forming any Ce^{3+}, since the electrons left by the leaving O occupy the O 2*p* holes. The E_{fv} for both the doped systems is almost the same, being driven primary by the electronic effect. The second and active Vo forms with a lower cost compared with the undoped ceria, hence the modified surfaces are more reducible. The lower cost is ascribed to the weaker Ag-O and Cu-O bonds compared to Ce-O in the host lattice of ceria.

The poly-valency of the two dopants makes energetically accessible solutions with different oxidation state for Ag/Cu and the Ce. Both dopants preferred the +2-oxidation state in the absence of active oxygen vacancies; instead after reduction, the +1 state is neatly favoured by Ag, while for Cu the preference is much less emphasised, due to the higher mobility and flexibility of the coordination environment.

The comparison with the experimental data on modified ceria surfaces, reduced by means of thermal treatment, indicated a very similar enhancement of the reducibility for both the Ag and Cu modified surfaces with respect to the unmodified ones. The XPS measurements indicated the oxidation state of the dopants to be +1 also before reduction: the difference with our calculations is likely due to the role of electron donor of the Pt support for the ceria films, not considered in our modelling due to an excessive computational complexity for our hybrid DFT approach.

The experimental results suggest a partial depletion of Cu from the surface in mild conditions, while Ag shows a much higher thermal stability up to 500°C.

This last factor is determinant for the design of catalyst operating at intermediate-high temperature, suggesting a possible application of Ag-doped ceria as an electrode component for intermediate temperature solid oxide fuel cells.

4.5 References

1. McFarland, E. W. & Metiu, H. Catalysis by Doped Oxides. *Chem. Rev.* **113**, 4391–4427 (2013).
2. Nolan, M. Enhanced oxygen vacancy formation in ceria (111) and (110) surfaces doped with divalent cations. *J. Mater. Chem.* **21**, 9160 (2011).
3. Shapovalov, V. & Metiu, H. Catalysis by doped oxides: CO oxidation by $Au_xCe_{1-x}O_2$. *J. Catal.* **245**, 205–214 (2007).
4. Nolan, M. Healing of oxygen vacancies on reduced surfaces of gold-doped ceria. *J. Chem. Phys.* **130**, 144702 (2009).
5. Figueroba, A., Kovács, G., Bruix, A. & M. Neyman, K. Towards stable single-atom catalysts: strong binding of atomically dispersed transition metals on the surface of nanostructured ceria. *Catal. Sci. Technol.* **6**, 6806–6813 (2016).
6. Kundakovic, Lj. & Flytzani-Stephanopoulos, M. Cu- and Ag-Modified Cerium Oxide Catalysts for Methane Oxidation. *J. Catal.* **179**, 203–221 (1998).
7. Righi, G., Magri, R. & Selloni, A. H_2 Dissociation on Noble Metal Single Atom Catalysts Adsorbed on and Doped into CeO_2 (111). *J. Phys. Chem. C* **123**, 9875–9883 (2019).
8. Gasperi, G. *et al.* Reducibility of Ag- and Cu-Modified Ultrathin Epitaxial Cerium Oxide Films. *J. Phys. Chem. C* **123**, 13702–13711 (2019).

9. Marsman, M., Paier, J., Stroppa, A. & Kresse, G. Hybrid functionals applied to extended systems. *J. Phys. Condens. Matter* **20**, 064201 (2008).
10. Pisani, C., Apra, E. & Causa, M. Density matrix of crystalline systems. I. Long-range behavior and related computational problems. *Int. J. Quantum Chem.* **38**, 395–417 (1990).
11. Dovesi, R. *et al.* Quantum-mechanical condensed matter simulations with CRYSTAL. *Wiley Interdiscip. Rev. Comput. Mol. Sci.* e1360 (2018) doi:10.1002/wcms.1360.
12. Adamo, C. & Barone, V. Toward reliable density functional methods without adjustable parameters: The PBE0 model. *J. Chem. Phys.* **110**, 6158–6170 (1999).
13. Doll, K. & Harrison, N. M. Chlorine adsorption on the Cu(111) surface. *Chem. Phys. Lett.* **317**, 282–289 (2000).
14. Doll, K. & Harrison, N. M. Theoretical study of chlorine adsorption on the Ag(111) surface. *Phys. Rev. B* **63**, (2001).
15. Andrae, D., Haeussermann, U., Dolg, M., Stoll, H. & Preuss, H. Energy-adjusted ab initio pseudopotentials for the second and third row transition elements: Molecular test for M2 (M= Ag, Au) and MH (M= Ru, Os). *Theor. Chem. Acc. Theory Comput. Model. Theor. Chim. Acta* **78**, 247–266 (1991).
16. Gupta, A., Waghmare, U. V. & Hegde, M. S. Correlation of Oxygen Storage Capacity and Structural Distortion in Transition-Metal-, Noble-Metal-, and Rare-Earth-Ion-Substituted CeO_2 from First Principles Calculation. *Chem. Mater.* **22**, 5184–5198 (2010).
17. Hu, Z. & Metiu, H. Effect of Dopants on the Energy of Oxygen-Vacancy Formation at the Surface of Ceria: Local or Global? *J. Phys. Chem. C* **115**, 17898–17909 (2011).

Chapter 5: H_2 Dissociation and Water Evolution on Silver-Decorated CeO_2(111)

5.1 Introduction

Ceria catalytic activity is related to the exchange of O with substrates; therefore, it is an ideal support for many oxidation reactions. Moreover, it has been found promising also in hydrogenation catalysis. For instance, the stand-alone oxide has been found to exhibit excellent activity for the selective hydrogenation of alkynes and alkenes[1]. Besides, the use of bare ceria as electrocatalyst for the methane oxidation in a solid oxide fuel cell operating at 650 °C has drawn much attention for applications at lower T.[2]

Ceria powders can dissociate H_2 under low partial pressure and low T, with hydroxylation of the surface, while heating treatment leads to the formation of water and vacancies. In the same conditions, regular (extended, flat) surfaces of ceria are less reactive towards the H_2, while the reaction takes places at higher partial pressure.

The reactivity towards H_2 can be enhanced by employing the cerium oxide as active support for transition metal nanoparticles: the formation of the interface between the metal and the oxide modifies the local structure and the electronic properties at the junction, which may catalyse the reaction of interest.

Moreover, this strong-metal support interaction, well documented on ceria-metal materials, is beneficial also to limit the mobility of the particles, preventing coalescence phenomena, thus the loss of catalytic activity.

These features have been exploited to design new catalysts, employing lower amounts of precious noble metals, or by replacing these latter with less noble ones.

In particular, pure silver and copper are much cheaper and less catalytically active than the platinum group metals towards H_2, but they are activated when used on an oxide support.

Temperature programmed reduction (TPR) experiments on Ag and Cu modified nanoceria with CH_4 and H_2, indicate higher activity towards their oxidation, associated to an easier transferability of the undercoordinated oxygen anions, but the nature and role of the modifier metal were not clarified[3]. Experimental results (TPR-H_2 and ECR) have shown for Cu nanoparticles deposed on ceria supports an improved activity and kinetics towards the oxidation of H_2, rationalized by the PBE+U modelling of the reaction taking place kinetically enhanced at the three-phase boundary (TPB) formed by gas-phase H_2, the support of CeO_2 (111) and the metal cluster Cu_{10}[4].

The reactivity of supported Ag on CeO_2 systems towards the oxidation of H_2 has received limited attention, notwithstanding the deposition of Ag nanoparticles on ceria 111 with different stoichiometry has been long investigated[5,6,7].

Applications of core-shell catalyst based on CeO_2/Ag as selective hydrogenation catalysts[8] suggest that the TPB Ag/CeO_2 promoted the heterolytic dissociation of H_2, in contrast to the homolytic dissociation preferred on the metallic phase[9].

Recently, a PBE+U investigation of Righi *et al*.[10] has shown that among coinage metals, Ag provides the lowest activation energy for the H_2 dissociation, as single-atom catalyst (SAC) on CeO_2 (111), indicating a possible application as anode electrocatalyst in proton exchange membrane fuel cell.

In this chapter, we report our investigation on the compared reactivity towards H_2 of a pristine ceria surface and the same surface doped with a silver cluster Ag_{10}. The processes of H_2 adsorption, dissociation and subsequent formation of water are considered. Furthermore, the effects of the formation on the interface Ag-CeO_2 on the electronic structure of the systems and on the oxygen vacancies are discussed.

5.2 Computational details

All calculations have been performed with the global hybrid functional PBE0[11], including spin-polarization, with the CRYSTAL17 code[12]. Dispersion effects have been considered by including the semi-empirical correction D3[13,14], damped with the Becke-Johnson scheme[15].

A slab model of the ceria surface has been obtained by cutting the CeO_2 bulk (PBE0 optimized conventional cell a= 5.402 Å) along the (111) plane and taking a (4 x 4) surface unit cell formed by two tri-layers (O-Ce-O). In all calculations, only the three layers interacting with the adatoms have been allowed to relax, while the bottom three layers have been fixed to emulate the bulk. A hemispherical shaped Ag_{10} cluster, derived by two atomic layers of Ag (111) has been chosen, as used in a previous work[6].

The irreducible Brillouin zone has been sampled with a regular Monkhorst-Pack mesh 2 × 2 × 1, with a total number of 4 k points for all the slab calculations.

Ce and O have been modelled using the same semi-relativistic ECP (Ce only) and GTO basis sets as defined in chapter 2: Ce2 and O1 here composed the BS1, and the larger basis Ce3 and O2, form the BS2. Both BS1 and BS2 share the same basis sets for Ag and H: the inner-core of Ag has been described by the semi-relativistic ECP developed by Dolg and co-workers[16], and the $4s^2 4p^6 5s^1 4d^{10}$ electrons were described by a (6s5p5d)/[4s3p2d] contraction scheme[17], while for H, the POB-TZVP basis set was used[18]. Here, all geometry optimizations and frequencies calculations have been

performed with the BS1. Single points calculations on the optimized structures have been performed with the larger BS2 to evaluate the effects on the energetic. In the following text, all energies reported have been computed with the BS1, including the D3 correction, while effects of the BS2 are discussed apart.

The transition state (TS) search has been performed by employing the distinguished reaction coordinate approach[19,20], by first performing a relaxed scan along with the selected reaction coordinate to approximate the TS, and then by refining the structure following uphill the lowest eigenvector of the Hessian matrix. The located saddle points have been confirmed by frequencies calculations performed at the Γ point, all characterized by a single imaginary frequency. To decrease the high computational cost related to the numerical calculation of the Hessian matrix, this has been built considering only a fragment of the system, corresponding to the adatoms and to their first and second neighbours. Additional tests performed on larger fragments resulted in negligible differences on the computed frequencies.

Basis set superposition error has been considered by adopting the standard counterpoise approach[21].

5.3 Results and discussion

5.3.1 Adsorption of Ag_{10} on CeO_2 (111)

Previous theoretical works investigated Ag clusters on CeO_2 (111), Ag_1, Ag_4, Ag_5, Ag_{10} and Ag_{13}[10, 22,6,23]. In all cases, the Ag depositions reduced the ceria surfaces, with the reduction of one up to three Ce^{4+} to Ce^{3+}, all located in the cationic layer closer to the surface.

The Ag_{10} cluster here adopted, obtained from two atomic layers of the Ag 111 surface, has a singlet closed-shell electronic ground state. No gas-phase relaxation is considered before the adhesion on ceria to preserve the hemispherical shape. Nevertheless, the adsorption energies have been computed with respect to the relaxed gas phase cluster. The initial orientation of the cluster on the slab was selected to maximize the interaction Ag-O.

The deposition of a metal atom or cluster on the oxide occurs with a charge polarization or a net charge transfer: for Ag on CeO_2, the deposition of a single Ag leads to the reduction of a Ce^{4+} to Ce^{3+} and to the oxidation of Ag to Ag^{+1}. With larger clusters, more electrons are transferred: for Ag_5, Ag_{10} and Ag_{13}, from 2 to 3 Ce^{3+} are formed upon reduction of the surface. Different SCF solutions may be obtained, characterized by a different extent of the electron transfer and of the spatial distribution of the Ce^{3+} ions, as in the case investigated by Bruix *et al* on Pt_8/CeO_2[24].

The difference between alpha and beta electrons (N_α-N_β) can be constrained in order to investigate solutions differentiated by the number of transferred electrons[25]. orbitals, but only configurations with energies very close to the local minimum are obtainable with this approach.

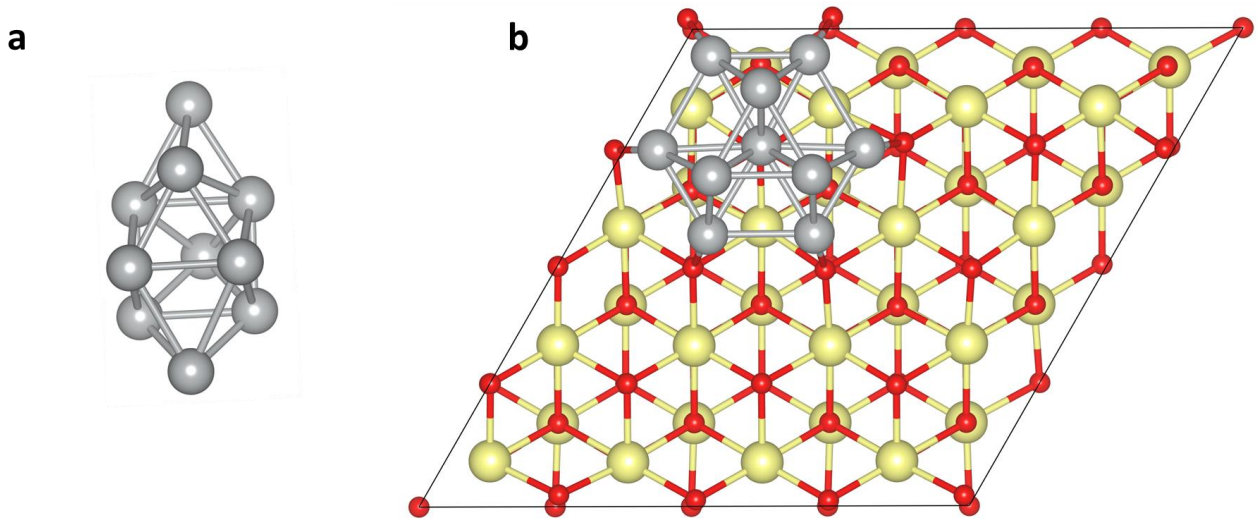

Figure 1. (a) Gas-phase optimized Ag_{10} cluster; (b) $Ag_{10}/CeO_2(111)$ on a p(4x4) cell. Grey, red and ivory spheres correspond to Ag, O and Ce atoms, respectively.

Moreover, the spatial configurations of the Ce^{3+} ions can be investigated by assigning the site occupation of the 4*f*.

Without any constrain on the magnetization or bias of the initial electronic configuration, the found solution contained two Ce^{3+}, with an AFM spin alignment. By constraining the magnetization to 4 μ_B, a more stable solution (FM1) is found with 3 Ce^{3+} and one unpaired electron delocalized over Ag_{10}. With the same unit cell's magnetization but different initial spin assigned to the Ce ions, another FM (FM2) configuration of the 3 Ce^{3+} is found, 0.04 eV higher in energy with respect to the former.

On the FM1 solution, the effects of the spin alignment of the Ce^{3+} ions on the total energy can be evaluated by flipping the spin on the ions to obtain different magnetic configurations. All differences obtained are below 0.01 eV, with a preference for the AFM alignments with respect to the FM one.

Here, we have not performed a systematic search for the most stable Ce^{3+} configurations, since adsorption energies, defect formation energies and H_2 dissociation energies are all significantly larger than the energy differences of the different Ce^{3+} configurations obtained. Therefore, in the following, only the FM1 configuration has been considered. The adsorption energies (E_{ads}) of the cluster on the ceria surface has been calculated according to

$$E_{ads}(Ag_{10}) = E(Ag_{10}/CeO_2(111)) - E(CeO_2(111)) - E(Ag_{10}) \quad (1)$$

and is of -5.55 eV, of which -2.44 eV arises from the dispersion correction. These indicates the significant contributions of the dispersive force in the bonding between cluster and surface, similarly to the results found for Ag adsorbed on ZrO_2 and TiO_2[26].

Figure 2 depicts the structure of the most stable solution obtained and the associated density of states. For a comparison of the other solutions, the interested reader can see the publication related to this work[27].

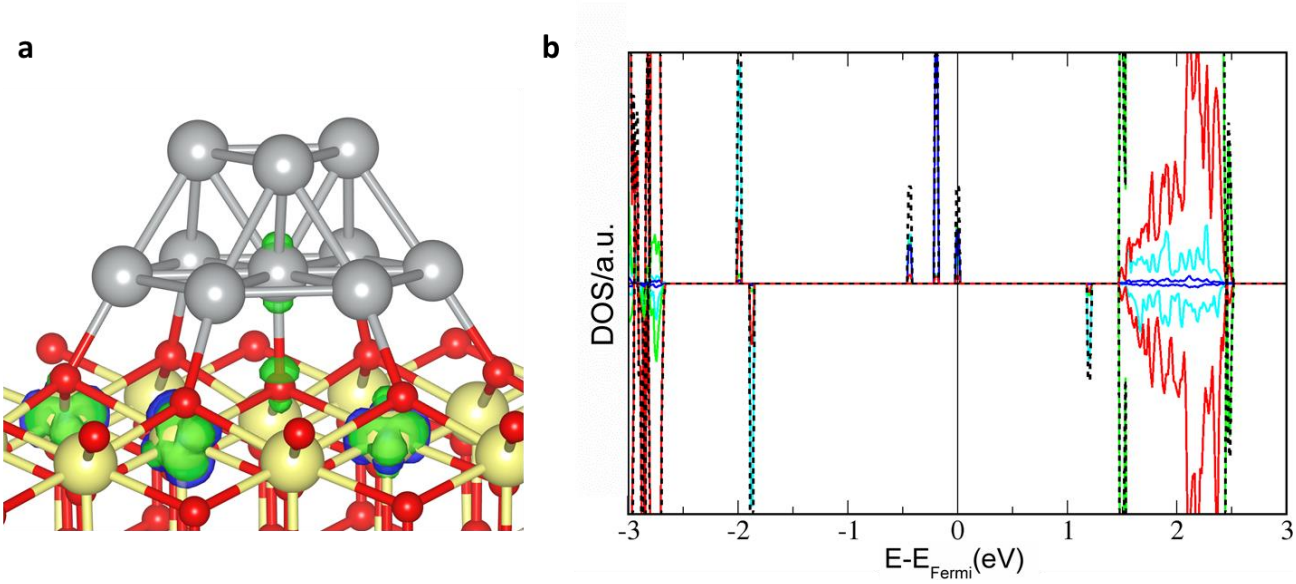

Figure 2. (a): spin density maps (isocontour value: 0.01 atomic unit) for FM1, the most stable configuration of the Ce^{3+} obtained for $Ag_{10}/CeO_2(111)$. Grey, red and ivory spheres correspond to Ag, O and Ce atoms, respectively. Green and blue isosurfaces correspond to positive and negative contributions to the spin density, respectively. (b): total (dotted black lines) and atom-projected contributions to density of states, with O, Ce, Ag and Ce^{3+} contributions in red, green, cyan and blue, respectively.

The adsorbed cluster Ag_{10} acquired a net charge Q of 1.36 $|e^-|$, and a spin polarization M of 1.02 μ_B. The Ag_{10} cluster has a net positive charge Q of 1.36 $|e^-|$ and a magnetization M of $|1.02|$ μ_B, while on the 3 Ce^{3+} the ionic charges decrease by 0.39 $|e^-|$, in average, with respect to the Ce^{4+} of the clean surface. On each of the Ce^{3+}, M is equal to $|0.98|$ μ_B. The computed density of states (see **Figure 2b**) shows three distinct peaks associated with the localized 4*f* states on three Ce^{3+} below the Fermi level (2.51 eV above the top of the O 2*p* band) in a narrow interval of 0.28 eV. Between the O 2*p* and the occupied Ce 4*f* states, peaks associated with the bonding interaction between O 2*p* and Ag 5*s*4*d* states appear (0.59 eV above the top of the O 2*p* band), while an antibonding peak with Ag 5*s*5*p*4*d* character appears 1.27 eV above the Fermi level. The unoccupied Ce 4*f* band lies 1.66 eV above the Fermi level.

5.3.2 Oxygen vacancies formation.

As it has been discussed in the previous chapters, the formation energy of the Vo is used as a descriptor of the catalytic activity of the ceria in processes involving the exchange of oxygen atoms. Even if the dissociation of H_2 does not involve the formation of vacancies, the pairing of H and OH

on the oxide surface forms a water molecule, therefore it is necessary to evaluate how their formation is affected by the cluster.

Besides substitutional doping, the E_{fv} can be modulated by modifying the surface with different substrates which may hinder or facilitate the O extraction: here, the effect of the Ag_{10} cluster on the formation of a V_O is examined for different sites and compared with the clean surface of CeO_2 (111). In **Table 1** are reported the energy formations obtained on clean CeO_2(111) and Ag_{10}/CeO_2 (111), as well other data concerning the number of Ce^{3+} ions, their averaged magnetic momenta and the total charge and magnetization of the cluster**.** The reference for the vacancy on the clean surface is the V_O with the configuration NN-NN of the reduced Ce ions, as previously motivated in chapters 3 and 4.

Being the energies differences between the magnetic configurations FM and AFM of the Ce^{3+} associated to the V_O not larger than 0.05 eV[28,29], we avoided a systematic investigation of all possible magnetic configurations, but we limited to check few representative cases.

Three types of surface O have been chosen to form the vacancy on Ag_{10}/ CeO_2, indicated in **Figure 3**: on the surface of the oxide (O_S), at the Ag_{10}/CeO_2 interface (O_I) and underneath the cluster (O_U). On the O_S sites (S_1 and S_2), the vacancy forms with reduction of 2 Ce in NN positions and with E_{fv} almost equal to the reference case (3.34 eV).

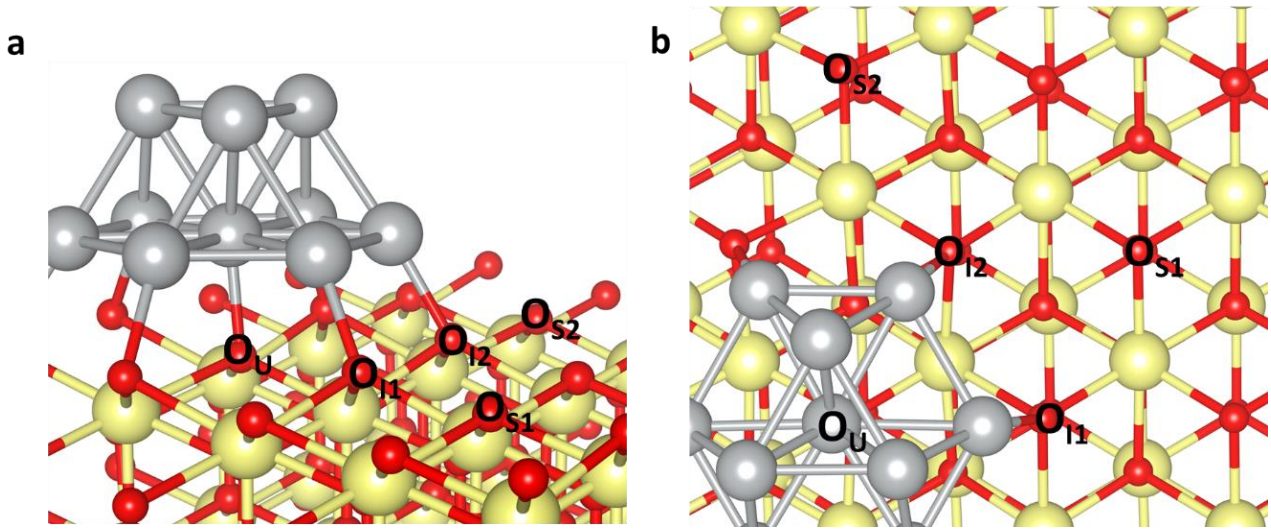

Figure 3. Side (a) and top (b) views of the Ag_{10}/CeO_2(111) system. The sites for the V_O creation are labelled as in Table 2. The same colour code as in Figure 1 is adopted.

For the O_I sites (I_1 and I_2), the formation of the vacancy is followed by the reduction of the Ag cluster and of a single Ce, with E_{fv} higher than the value obtained for the clean surface.

For the O_U site, the cluster and a Ce are reduced when the vacancy forms, but the associated cost is smaller to both the O_S and O_I sites.

These latter results agree with previous computations[6], which found the adsorption of Ag_{10} on the here defined O_U site 0.74 eV more stable than on the ideal CeO_2 (111). The energy difference for the two V_O can be ascribed to the different structural relaxation of the cluster: for the O_I sites case, the silver next to the vacancy, negatively polarized (-0.32 $|e^-|$) is drawn by the vacancy (positively charged), with a consequent small drift of the cluster towards the vacancy direction and structural asymmetric distortion.

For the O_U site, instead, the electron density transferred to the cluster is evenly shared by the atoms of the cluster, and the Ag-O and Ag-Ag bond distances increase homogeneously.

These findings indicate that the silver cluster quenches the V_O formation at the peripherical sites, while O_S sites are unaffected. Similar trends have been reported for the $Cu/CeO_2(111)$[4], $Ni/CeO_2(111)$[30] and $Pd/CeO_2(111)$, which are opposite the findings obtained on other oxides supporting metal particles, as MgO, BaO, TiO_2 and ZnO, where the V_O formation is enhanced at the interface and surface sites compared to the bare surfaces[31].

The different behaviour is related to the direct reduction of the Ce layer closest to the metal particle: the average distance Ce-O increase, being the Ce^{3+} ions larger than the Ce^{4+}, and internal strain builds-up as consequence, which hindered the thermodynamic of further processes of reduction, as the V_O formation, as seen here, or the H_2 oxidation, which will be shown in the following sections.

The lower E_{fv} computed for the V_O at O_S with respect to the O_I suggests for the former an easier cession in a Mars van Krevelen process: in section 5.4 it is shown that while the O_S extraction as water is easier from a thermodynamic point of view, this process is kinetically favoured at O_I sites.

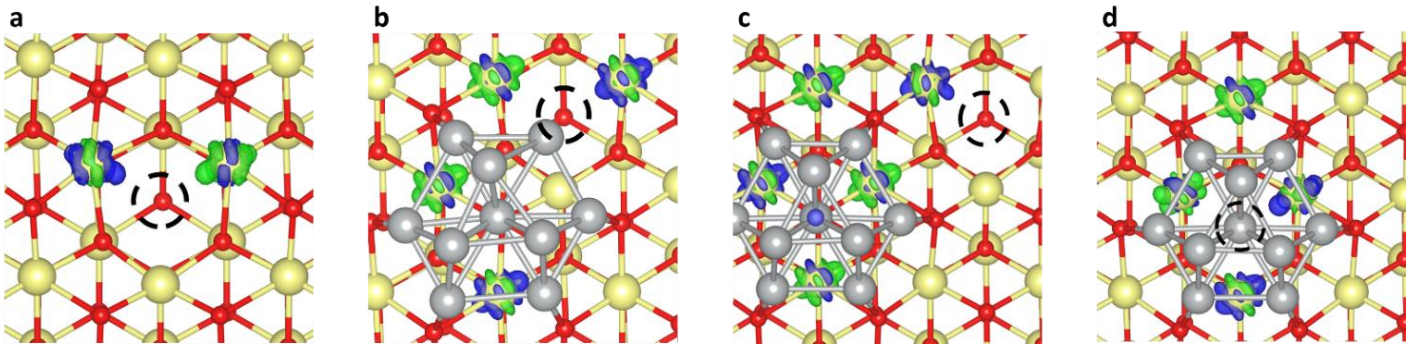

Figure 4: Spin density maps (isocontour value: 0.01 atomic unit) for V_O at: (a) clean $CeO_2(111)$ and at different positions on $Ag_{10}/CeO_2(111)$: (b) O_{I1}, (c) O_{S1}, (d) O_U configurations. The dashed black circle indicates the Vo site. Green and blue isosurfaces correspond to positive and negative contributions to the spin density, respectively.

Table 1. Computed formation energies (E_{fv}, in eV) of surface O vacancies, with respect to 1/2 O_2, for the CeO_2(111) and Ag_{10}/CeO_2(111) systems, along with total charge on the Ag cluster (Q_C, in $|e^-|$), Ce^{3+} spin population (M, in $|\mu_B|$) and number of Ce^{3+} obtained (N_{Ce3+}). The site labels used in the second column are defined in **Figure 3**.

System	Site	N_{Ce3+}	M_{Ce3+}	Q_{Ag10}	M_{Ag10}	E_{fv}
CeO_2	-	2	0.971	-	-	3.34
Ag_{10}/CeO_2	O_{S1}	5	0.979	1.35	0.871	3.30
	O_{S2}	5	0.973	1.34	0.896	3.32
	O_{I1}	4	0.966	0.93	0.049	3.62
	O_{I2}	4	0.969	0.92	0.004	3.81
	O_U	4	0.974	0.98	0.009	2.70

5.3.3 H_2 on CeO_2 (111)

Due to the large technological interest, H_2 and ceria interactions have been long investigated both experimentally and theoretically[1,32-36]. Experiments indicates the inertial character of pristine and reduced flat ceria surfaces at low partial pressure of H_2 and cryogenic temperatures. Increasing the pressure to the mBar regime (magnitude), the CeO_2(111) surface shows dissociative activity[1]. Two possible mechanisms of dissociation, heterolytic and homolytic, have been characterized theoretically, with the former being kinetically favoured[1,35-38]. The presence of V_O on CeO_2 (111) seems not to affect the rate of the dissociation of H_2, at difference with the conversion rates of the alkynes to olefins[39], where the surface O sites are probably involved in the adsorption of the substrates[38,40]. On the hydroxylated surfaces, instead, H_2 dissociation and water formation compete under heating, with the latter process being favoured on the stoichiometric surfaces, but unfavoured at increasing concentration of oxygen vacancies. In the following, the results for the process of H_2 adsorption and dissociation on the clean ceria surfaces are presented, followed by the recombination of the surface hydroxyls to form water. For every structure containing $Ce^{3+,}$ both the FM and the AFM solutions have been investigated: here the results for the AFM solutions are reported and only the difference with the FM ones are discussed. The hydrogen molecule physisorption on the ceria surface can occur with either on-top or side-on orientation (see **Figure 5**), and adsorption energies of -0.19 and -0.16 eV, respectively. The latter is the precursor for the heterolytic dissociation, favoured with respect to the homolytic one, and considered in this work.

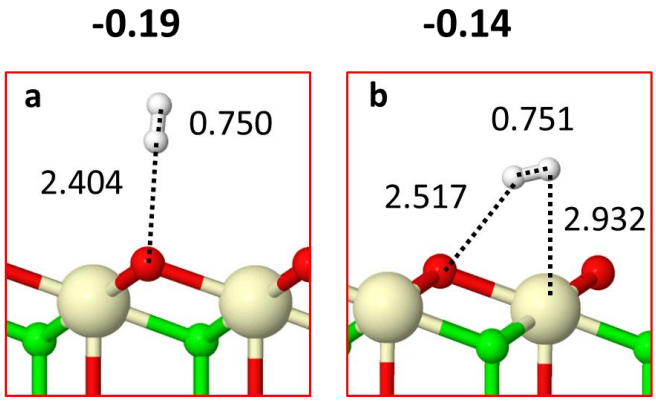

Figure 5. Side views of $H_2/CeO_2(111)$: (a) on top; (b) side-on ($\mathbf{M_1^C}$, **Fig. 6**), showing selected interatomic distances (in Å), and on top of the captions, the adsorption energies (in eV).
Red, green, ivory and white spheres correspond to surface O, subsurface O, Ce and H atoms.

The main structural data and charges associated to the steps of the investigated reaction path are reported in **Table 2**. The reaction profiles are presented in **Figure 6** and the corresponding structures are depicted in **Figure 7** and **Figure 8**.

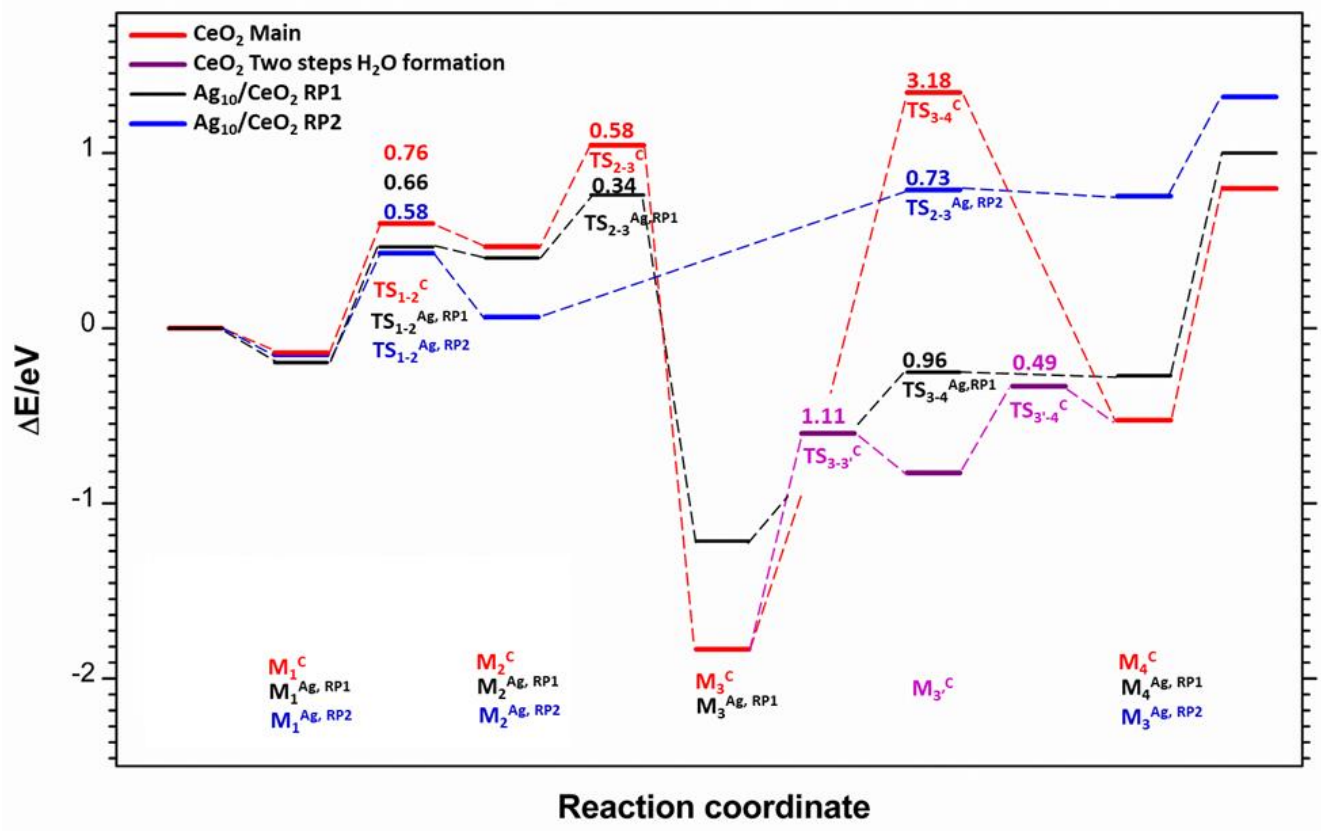

Figure 6. Energy profiles for the H_2 dissociation and H_2O formation on pristine $CeO_2(111)$ (main path in red and the two step H_2O formation in purple) and $Ag_{10}/CeO_2(111)$, along the RP1 (in black) and RP2 (in blue) paths (see text for definitions). Data indicated over the horizontal solid lines correspond to the computed activation energies.

In the side-on structure, hereafter called $\mathbf{M_1^C}$, the H-H bond lies parallel to the O-Ce ionic couple located respectively in the first and second atomic layer of the surface.

The electrostatic interaction with the ionic couple polarized the σ bond of H_2[35], which stretch and dissociated, crossing the transition state $\mathbf{TS_{1\text{-}2}^C}$, to form the heterolytic dissociation product $\mathbf{M_2^C}$, where an O-H and a Ce-H (Ce^{4+}-H^-) bonds are formed.

The dissociation is endothermic (+ 0.56 eV), with an activation energy of 0.76 eV. $\mathbf{M_2^C}$ then evolves to form $\mathbf{M_3^C}$, the product corresponding to the homolytic dissociation, going through the $\mathbf{TS_{2\text{-}3}^C}$ and an associated barrier of 0.58 eV.

This transition state is characterized by the breaking of the ionic pair H^+/H^-, with the transfer of one electron from the hydride to the bound Ce^{4+}, thus reduced to Ce^{3+}, and by the atomic H migrating towards one of the vicinal O to forms the second hydroxyl characteristic of $\mathbf{M_3^C}$, as well a second Ce^{3+}. The whole process of the dissociative adsorption of H_2 is exothermic, with an energy difference between the isolated H_2/surface and $\mathbf{M_3^C}$ of -1.83 eV.

From $\mathbf{M_3^C}$, the adsorbed H atom can migrate to an adjacent surface O, changing the disposition of the hydroxyls, or can migrate from one hydroxyl to the other with the formation of water molecularly adsorbed ($\mathbf{M_4^C}$).

Only the latter case has been considered here, and two possible mechanisms have been characterized: a one-step linear reaction path for the H migration, and a two-steps processes, which involves an intermediate specie. The first process, characterized by the transition state $\mathbf{TS_{3\text{-}4}^C}$, has the larger barrier, corresponding to 3.18 eV.

The two-step process instead, involves a first H transfer from the surface O to a vicinal subsurface O to form $\mathbf{M_{3'}^C}$, and then $\mathbf{M_4^C}$. The related transition states, $\mathbf{TS_{3\text{-}3'}^C}$ and $\mathbf{TS_{3'\text{-}4}^C}$, have been characterized, and the associated barriers are only of 1.11 and 0.49 eV, respectively, making the two-step mechanism clearly favoured compared to the other.

In M_4^C, the water molecule is formed, extracting the O from the lattice, but is tightly bound close to the vacancy site. Up to there, the whole reaction is exothermic (-0.53 eV): the reaction can further evolve in different ways: the water can migrate on other sites of the surface, rotate and dissociated again at the vacancy sites, or desorbs into the gas phase.

Here we consider only the latter process, which occurs endothermically (1.32 eV) and virtually barrierless.

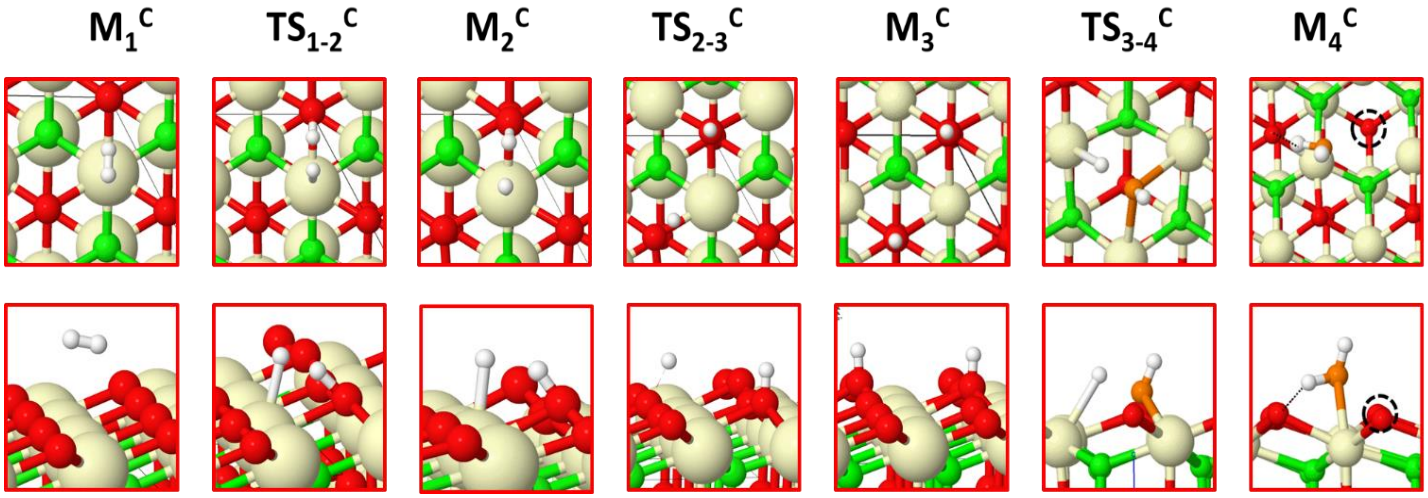

Figure 7. Top (top panel) and side views (bottom panel) of the optimized structures of all species involved in the reaction of H_2 over CeO_2(111). Red, green, orange, ivory and white spheres correspond to surface O, subsurface O, water forming O, Ce and H atoms, respectively. The V_O position is indicated by a black dashed circle. Hydrogen bonds are shown as black dashed lines.

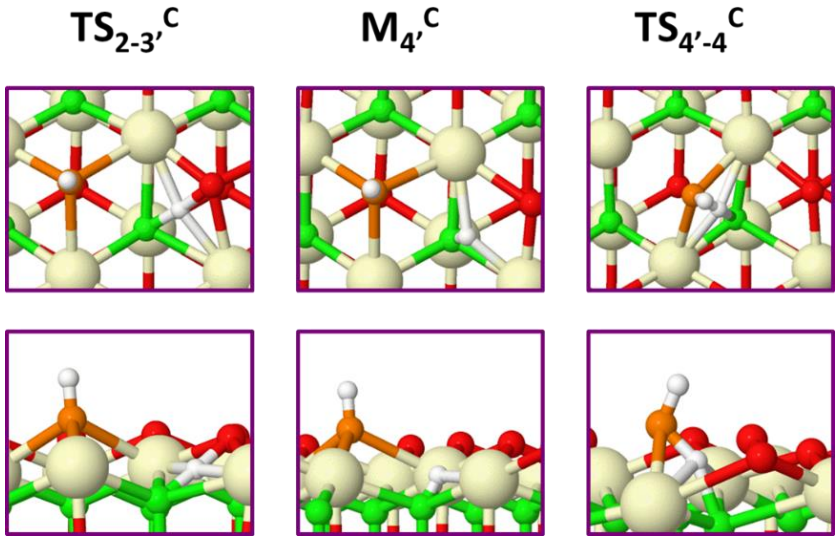

Figure 8. Top (top panel) and side views (bottom panel) of the different optimized structures for the two steps H migration. Precursor and products are depicted in **Figure 7** (see Section 3.3 for further details). The colour code is the same as that of **Figure 7**.

Additional calculations have been performed to evaluate the effects of the basis set quality and of the spin multiplicity on the computed calculations. With the more extended basis set, BS2, an overall increase of the exothermicity has been obtained: the H_2 physisorption is practically unaffected, while the dissociation and the water desorption became respectively 0.41 and 0.18 eV more favourable. Smaller variations have been computed for the barriers associated to **TS$_{1\text{-}2}^{C}$**, **TS$_{2\text{-}3}^{C}$** and **TS$_{3\text{-}3'}^{C}$**, which decrease respectively by 0.06, 0.12 and 0.06 eV, while for **TS$_{3'\text{-}4}^{C}$**, it increases by 0.04 eV. A comparison of the energy profiles obtained with the two basis sets is shown in **Figure B1** in **Appendix B**. These results indicate that the larger variations are associated to the step involving a variation in

the number of Ce^{3+} and in the formation of the vacancy, as we have observed on the energetics of reduction of CeO_2 to Ce_2O_3 discussed in the chapter 3. Since the H_2 dissociation occurs with the formation of a diradical system, we also evaluated the relative stability of the singlet AFM and triplet FM solution on the energy profiles. Starting from the FM geometries (BS1), single points calculations were performed by flipping the spin on a single Ce^{3+} of the system. For most cases, the AFM solutions were more stable by only 0.002-0.007 eV, while for the $\mathbf{TS_{2\text{-}3}^{C}}$ a larger difference of 0.027 eV was found. Only for the $\mathbf{M_3^C}$, the FM solution was found more stable than the AFM one, by 0.010 eV. From the results of these additional calculations the conclusion drawn above still holds.

5.3.4 H_2 on $Ag_{10}/CeO_2(111)$

After the reactivity investigation on the clean oxide, the silver ceria system is considered. Being the energies differences between the FM and AFM solutions computed on the clean ceria no larger than 0.03 eV, on Ag_{10}/CeO_2 we considered only the FM solutions.

Many possible reaction sites exist for the H_2 adsorption: here we limit to considered 4 representative cases, shown in **Figure 9** with the associated adsorption energies.

Since previous works[41,42] already investigated the dissociation of H_2 directly over a silver cluster supported on a metal-oxide, showing that the process is both kinetically and thermodynamically unfavoured if compared with the same process occurring at the interface silver/oxide, we considered the dissociation process only on two sites of the interphase. More precisely, we investigated the reaction paths involving H_2 occurring close to the cluster (RP1) and along the TPB (RP2). The two adsorption sites are shown in **Figure 9** (9a and 9c, respectively), then the other structures identified along the reaction path are depicted in **Figure 10** (RP1) and **Figure 11** (RP2).

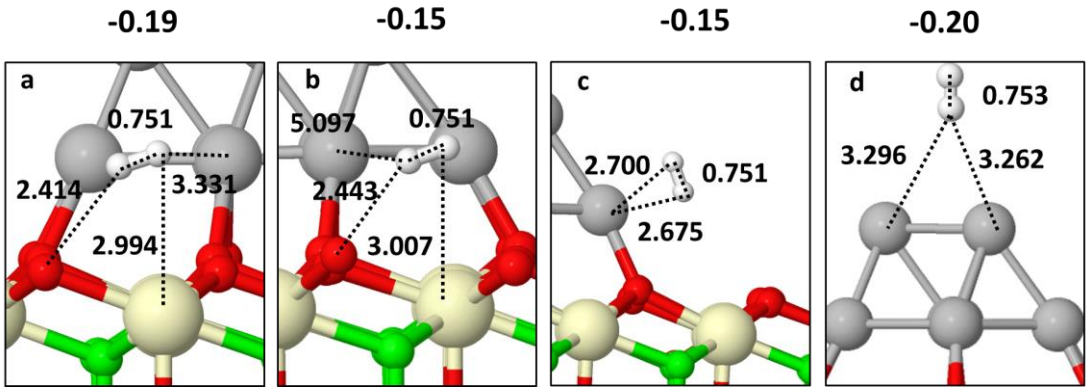

Figure 9. Four different adsorption sites considered for the adsorption of H_2 on $Ag_{10}/CeO_2(111)$: (a) surface site close to Ag_{10} ($\mathbf{M_2^{Ag,\ RP1}}$, see **Figure 10**); (b) surface site far from Ag_{10}; (c) three-phase-boundary ($\mathbf{M_2^{Ag,\ RP2}}$, see **Figure 11**); (d) on top of the cluster, with corresponding computed adsorption energies (in eV) reported on top of the figure and selected interatomic distances (in Å).

The reaction steps here characterized resemble closely the ones obtained on ceria, therefore the discussion will be limited to the main differences.

Reaction path 1: Overall, RP1 is characterized by lower energies changes when compared with the clean surface case. In particular, for the H_2 dissociation, the barriers associated with $\mathbf{TS_{1\text{-}2}^{Ag,\ RP1}}$ and $\mathbf{TS_{2\text{-}3}^{Ag,\ RP1}}$ are respectively 0.10 eV and 0.24 eV lower**.** The analysis of the data reported in table 2 indicated that the stabilization of these transition states might arise by an electrostatic interaction between the ionic pair H^+/H^- and the positively charged cluster for $\mathbf{TS_{1\text{-}2}^{Ag,\ RP1}}$, and to a bonding interaction between H and the closest Ag (d Ag-H=1.849 Å) for $\mathbf{TS_{2\text{-}3}^{Ag,\ RP1}}$. Globally, the dissociative adsorption of H_2 is 0.59 eV less exothermic than on the clean surface, possibly due to the different acid-basis characters of the two surfaces. In reducible oxides, as ceria, the cations have a strong Lewis's acid character, thus are more easily reduced[43,43]. The adsorption on the surface of a Lewis's base may lead to an electron transfer from the base to the acid, with consequent cancellation or decrease of their acid-base character. In the case considered, Ag_{10} and H_2 act both as Lewis's base, reducing the surface in a very exothermic process. The acid character of Ce^{4+} on Ag_{10}/CeO_2 is lowered by the adsorption of the cluster, and a further reduction by means of the H_2 oxidation is therefore less favourable. The decrease of the Lewis's acidity of the other Ce^{4+} ions is a local effect intrinsically related to the lattice strain which build close to the Ce^{3+}, and affect mostly the neighbour Ce^{4+}: sites further from the cluster are expected to have a close reactivity of the metal free surface.

Moreover, the computed atomic charges (see Table 2) indicates a higher charge separation on the H of both TS for Ag_{10}/CeO_2. In addition, the cluster's charge change along the dissociation steps, increasing in $\mathbf{TS_{1\text{-}2}^{Ag,\ RP1}}$ and then decreasing in $\mathbf{TS_{2\text{-}3}^{Ag,\ RP1}}$, suggesting that the H_2 dissociation at O sites close to the silver cluster is kinetically promoted by charge polarization effects which stabilize the TS involved. The subsequent water formation occurs following a single-step H transfer: the saddle point $\mathbf{TS_{3\text{-}4}^{Ag,\ RP1}}$ is characterize by the transferred H at bridge between the O_I site and the O_S-H hydroxyl, at difference with the process on the clean surface, where the single-step H transfer involve a binding of H to Ce. The relative barrier is 0.15 eV lower with respect to the highest of the two-steps mechanism ($\mathbf{TS_{3\text{-}3}^{,C}}$). Water formation ($\mathbf{M_3^{Ag,\ RP1}}$ to $\mathbf{M_4^{Ag,\ RP1}}$) and desorption ($\mathbf{M_4^{Ag,\ RP1}}$ to $\mathbf{M_5^{Ag,\ RP1}}$) are favoured by 0.34 eV and 0.07 eV, respectively.

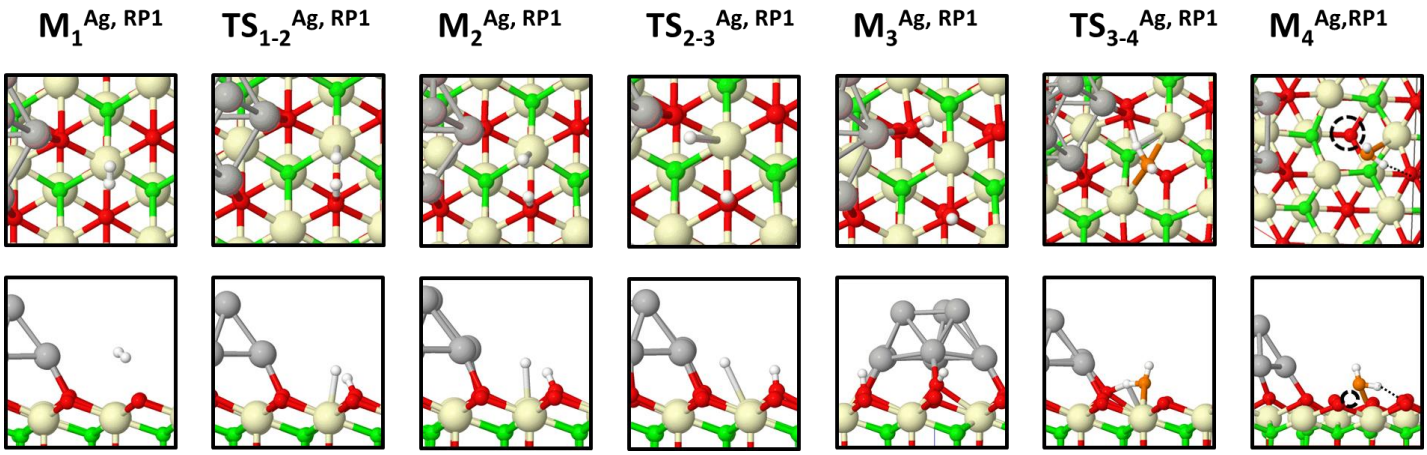

Figure 10. Top (top panel) and side views (bottom panel) of the optimized structures obtained for the RP1 path for $Ag_{10}/CeO_2(111)$. Red, green, orange, ivory and white spheres correspond to surface O, subsurface O, water forming O, Ce and H atoms, respectively.

Table 2. Selected atomic charges (Q, in $|e^-|$) and distances (d, in Å) for structures associated with the H_2 dissociation on clean CeO_2 and on Ag_{10}/CeO_2 along the RP1 path (see Figures. 6, 7 and 11). H^1/H^2 and O^1/O^2 are respectively the H and the O associated with the first and second hydroxyl formed. Ce^1 is that on which the adsorption of H_2 first occurs. The reported H^2-Ag distance is for the closest Ag atom to H^2.

	$Q(H^1/H^2)$	$Q(O^1/O^2)$	$Q(Ce^1)$	$Q(Ag_{10})$	d_{H-H}	$d(O^1-H^1)$	$d(H^2-Ce^1)$	$d(H^2-O^2)$	$d(H^2-Ag)$
M_1^C	0.00/0.00	-1.25/1.25	2.57	-	0.750	2.517	2.9326	3.085	-
TS_{1-2}^C	0.12/-0.39	-1.06/-1.26	2.48	-	1.121	1.127	2.207	2.942	-
M_2^C	0.18/-0.44	-0.96/-1.20	2.45	-	1.470	1.005	2.119	2.866	-
TS_{2-3}^C	0.23/-0.15	-1.00/-1.18	2.18	-	3.236	0.974	2.589	1.709	-
M_3^C	0.23/0.23	-1.00/-1.00	2.16	-	4.246	0.964	3.226	0.964	-
$M_1^{Ag, RP1}$	0.03/-0.01	-1.27/-1.26	2.56	1.35	0.751	2.414	2.994	3.032	3.331
$TS_{1-2}^{Ag, RP1}$	0.20/-0.48	-1.00/-1.26	2.48	1.38	1.118	1.121	2.195	2.878	3.417
$M_2^{Ag, RP1}$	0.17/-0.46	-1.04/-1.25	2.45	1.37	1.438	1.009	2.154	2.810	3.374
$TS_{2-3}^{Ag, RP1}$	0.23/-0.20	-0.99/-1.12	2.17	1.32	2.719	0.964	2.934	1.810	1.849
$M_3^{Ag, RP1}$	0.22/0.21	-1.00/-0.95	2.16	1.29	4.125	0.963	2.860	0.968	2.563

Reaction path 2: for RP2, the adsorption of H_2 proceeds on the TPB to form $M_2^{Ag, RP2}$, which dissociates heterolytically along the O_I-Ag bond to form $M_2^{Ag, RP2}$, where O_I-H and Ag-H bonds are formed along with the reduction of a single Ce^{4+} (see **Figure 11**). The associated transition state $TS_{1-2}^{Ag, RP2}$ lies 0.58 eV above $M_1^{Ag, RP2}$. Starting from this product, the H migration from the cluster to the hydroxyl (H spillover) occurs passing through $TS_{2-3}^{Ag, RP2}$ with a barrier of 0.73 eV. In the $M_2^{Ag, RP2}$ product, the water molecule is still firmly adsorbed to the cluster-oxide interface. Water may then desorb, leaving a V_O at the interface, with an energetic cost of 0.57 eV. Overall, the process is 0.32

eV less favoured compared to RP1, but the associated barriers for H_2 dissociation and water formation are respectively 0.08 and 0.23 eV lower.

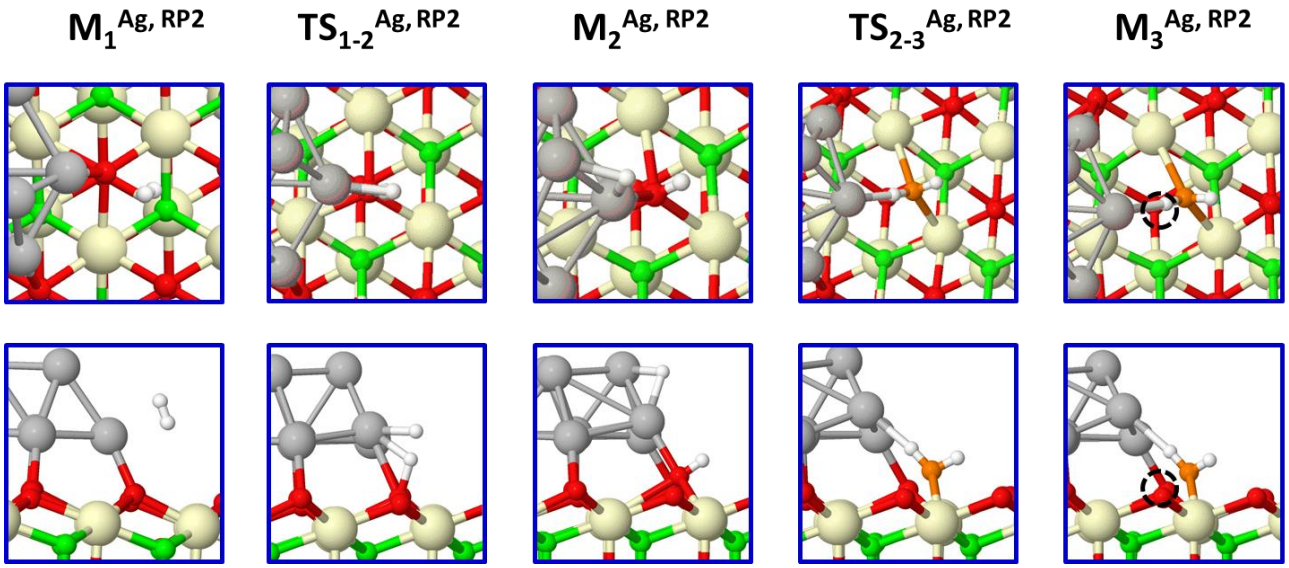

Figure 10. Top (top panel) and side views (bottom panel) of the optimized structures obtained for the RP1 path for $Ag_{10}/CeO_2(111)$. Red, green, orange, ivory and white spheres correspond to surface O, subsurface O, water forming O, Ce and H atoms, respectively.

As for the reaction on the clean surface, the effects of the basis set have been evaluated performing single points calculations with the more extended BS2 on the optimized structures for both RP1 and RP2. The comparisons of the energies profiles computed with the two basis sets is shown in **Figure B2** and **Figure B3** in **Appendix B.** The same shifts of the energies towards more negative values observed for the reaction on the metal free surface has been observed, without change the description of the reactivity at the sites investigated.

According to these results, the kinetic of the dissociation of H_2 over $Ag_{10}/CeO_2(111)$ is promoted compared on the clean ceria surface. In particular, the process at TPB formed by Ag/CeO_2/gas phase is favoured when compared to either the perimetric area of the cluster and the surface of the oxide.

The silver deposition reduces the Ce ions close to the interface: further processes of reduction as the surface hydroxylation are hindered in the proximity of these Ce^{3+} ions, thus facilitating reverse processes, either as H_2 elimination or as transfer of H to a substrate in reductive hydrogenation.

The water formation at the TPB is kinetically favoured as well, but the process is more endothermic if compared with the other sites, in agreement with the trend obtained on energies of formations of the O vacancies.

The investigation of Righi *et al*[10] on a model of single atom catalysts (SACs) supported on ceria indicated Ag as the most promising towards the H_2 oxidation, followed by Au and Cu, on the base

of the decrease of the activation energy for the aforementioned process with compared to the bare ceria. These results are relevant in view of rationalizing the relative activities of these coinage metals, but it should be remarked that the realization of true SACs, stable under working conditions, is still one of the main challenges in the field of catalysis[45].

Single metals atoms are much more mobile than larger cluster[46], and are likely to anchor at defects sites, as kinks of steps edges or at oxygen vacancy[47]. In the latter case, the adatom charge is likely to be negative or neutral,[48,49,50] with a drastically different reactivity with compared to the case investigated by Righi *et al.*

Properties computed on larger clusters are expected to be less sensitive to charge variations, therefore, in absence of experimental evidences of the most active/ representative cluster size, we consider Ag_{10} more appropriate for investigation of these systems.

In absence of experimental evidence of the most representative or catalytic active cluster of silver, Ag_{10} can be considered a suitable model, close to the scalable regime.

5.4 Conclusions

In this chapter, we have reported our study on the reactivity of the ceria surface 111, both metal-free and with an adsorbed silver cluster, towards the dissociation of H_2 and recombination in water. At first, the Ag_{10} deposition has been investigated: the interface cluster/oxide forms with a direct electron transfer from the cluster to the oxide, which reduced 3 Ce^{4+} to 3 Ce^{3+} in the proximity of the interface. The metal-oxide interaction has a short-range effect on the oxygen vacancies formation, which is hindered along the perimeter of the cluster, and almost unaffected on the closest surface sites, confirming the findings for other supported metals as Ni and Cu. For a vacancy underneath the cluster, on the other hand, a lower cost compared with the bare surface has been obtained, confirming the evidence of stronger adhesion of the Ag nanoparticles on partially reduced CeO_2 (111).

Concerning the H_2 dissociation and the H_2O formation we have found that: (i) the oxidative dissociation of H_2 at the TPB and at the periphery of the Ag cluster is kinetically favoured with respect to the clean surface, with the lower barriers obtained at the TPB; (ii) the hydroxylation of the surface is less exothermic in presence of the Ag cluster, indicating a lower affinity of the surface for the H. The lower barrier to transfer the hydrogen and to form water confirms this hypothesis, suggesting a higher turnover of this hypothetical Ag/CeO_2 catalyst; (iii) both water and O vacancies formation are favoured on the oxide surface sites, while the interface enhances the dissociation of H_2 and the H spill-over on the surface.

This study confirms the importance of the metal/oxide support interaction and of the three-phase-boundary in promoting the activation of such reactions, making Ag supported on CeO_2 worth to be

considered as a possible anodic electrocatalyst in solid oxide fuel cells, for instance, or even in the lower temperature working proton-exchange membrane fuel cells.

Starting from these results, the catalytic activity towards the H_2 oxidation of other metals can be considered by adopting the same Me_{10} (7-3) cluster model and limiting the study to the H_2 dissociation.

5.5 References

1. Werner, K. *et al.* Toward an Understanding of Selective Alkyne Hydrogenation on Ceria: On the Impact of O Vacancies on H_2 Interaction with CeO_2 (111). *J. Am. Chem. Soc.* **139**, 17608–17616 (2017).
2. Murray, E. P., Tsai, T. & Barnett, S. A. A direct-methane fuel cell with a ceria-based anode. *Nature* **400**, 649–651 (1999).
3. Kundakovic, Lj. & Flytzani-Stephanopoulos, M. Cu- and Ag-Modified Cerium Oxide Catalysts for Methane Oxidation. *J. Catal.* **179**, 203–221 (1998).
4. Wang, S., Zheng, M., Li, M., Wu, X. & Xia, C. Synergistic effects towards H_2 oxidation on the Cu–CeO_2 electrode: a combination study with DFT calculations and experiments. *J. Mater. Chem. A* **4**, 5745–5754 (2016).
5. Kong, D. *et al.* Growth, Structure, and Stability of Ag on CeO_2 (111): Synchrotron Radiation Photoemission Studies. *J. Phys. Chem. C* **115**, 6715–6725 (2011).
6. Luches, P. *et al.* Nature of Ag Islands and Nanoparticles on the CeO_2 (111) Surface. *J. Phys. Chem. C* **116**, 1122–1132 (2012).
7. Hu, S. *et al.* Ag Nanoparticles on Reducible CeO_2(111) Thin Films: Effect of Thickness and Stoichiometry of Ceria. *J. Phys. Chem. C* **119**, 3579–3588 (2015).
8. Mitsudome, T. *et al.* Design of a Silver-Cerium Dioxide Core-Shell Nanocomposite Catalyst for Chemoselective Reduction Reactions. *Angew. Chem. Int. Ed.* **51**, 136–139 (2012).
9. Zhang, L., Zhou, M., Wang, A. & Zhang, T. Selective Hydrogenation over Supported Metal Catalysts: From Nanoparticles to Single Atoms. *Chem. Rev.* (2019) doi:10.1021/acs.chemrev.9b00230.
10. Righi, G., Magri, R. & Selloni, A. H_2 Dissociation on Noble Metal Single Atom Catalysts Adsorbed on and Doped into CeO_2 (111). *J. Phys. Chem. C* **123**, 9875–9883 (2019).
11. Adamo, C. & Barone, V. Toward reliable density functional methods without adjustable parameters: The PBE0 model. *J. Chem. Phys.* **110**, 6158–6170 (1999).
12. Dovesi, R. *et al.* Quantum-mechanical condensed matter simulations with CRYSTAL. *Wiley Interdiscip. Rev. Comput. Mol. Sci.* e1360 (2018) doi:10.1002/wcms.1360.

13. Grimme, S. Semiempirical GGA-type density functional constructed with a long-range dispersion correction. *J. Comput. Chem.* **27**, 1787–1799 (2006).
14. Grimme, S., Antony, J., Ehrlich, S. & Krieg, H. A consistent and accurate ab initio parametrization of density functional dispersion correction (DFT-D) for the 94 elements H-Pu. *J. Chem. Phys.* **132**, 154104 (2010).
15. Grimme, S., Ehrlich, S. & Goerigk, L. Effect of the damping function in dispersion corrected density functional theory. *J. Comput. Chem.* **32**, 1456–1465 (2011).
16. Dolg, M., Stoll, H. & Preuss, H. Energy-adjusted pseudopotentials for the rare earth elements. *J. Chem. Phys.* **90**, 1730–1734 (1989).
17. Doll, K. & Harrison, N. M. Theoretical study of chlorine adsorption on the Ag(111) surface. *Phys. Rev. B* **63**, (2001).
18. Peintinger, M. F., Oliveira, D. V. & Bredow, T. Consistent Gaussian basis sets of triple-zeta valence with polarization quality for solid-state calculations. *J. Comput. Chem.* **34**, 451–459 (2013).
19. Simons, J. & Nichols, J. Strategies for walking on potential energy surfaces using local quadratic approximations. *Int. J. Quantum Chem.* **38**, 263–276 (1990).
20. Zicovich-Wilson, C. M., San Román, M. L. & Ramírez-Solís, A. Mechanism of F− Elimination from Zeolitic D4R Units: A Periodic B3LYP Study on the Octadecasil Zeolite. *J. Phys. Chem. C* **114**, 2989–2995 (2010).
21. van Duijneveldt, F. B., van Duijneveldt-van de Rijdt, J. G. C. M. & van Lenthe, J. H. State of the Art in Counterpoise Theory. *Chem. Rev.* **94**, 1873–1885 (1994).
22. Piotrowski, M. J., Tereshchuk, P. & Da Silva, J. L. F. Theoretical Investigation of Small Transition-Metal Clusters Supported on the CeO_2(111) Surface. *J. Phys. Chem. C* **118**, 21438–21446 (2014).
23. Tereshchuk, P. *et al.* The role of charge transfer in the oxidation state change of Ce atoms in the TM13–CeO_2(111) systems (TM = Pd, Ag, Pt, Au): a DFT + U investigation. *Phys. Chem. Chem. Phys.* **17**, 13520–13530 (2015).
24. Bruix, A. *et al.* Effects of deposited Pt particles on the reducibility of CeO_2(111). *Phys. Chem. Chem. Phys.* **13**, 11384 (2011).
25. Bruix, A. *et al.* Effects of deposited Pt particles on the reducibility of CeO_2(111). *Phys. Chem. Chem. Phys.* **13**, 11384–11392 (2011).
26. Puigdollers, A. R., Schlexer, P. & Pacchioni, G. Gold and Silver Clusters on TiO_2 and ZrO_2 (101) Surfaces: Role of Dispersion Forces. *J. Phys. Chem. C* **119**, 15381–15389 (2015).

27. Brugnoli, L., Pedone, A., Menziani, M. C., Adamo, C. & Labat, F. H_2 Dissociation and Water Evolution on Silver-Decorated CeO_2(111): A Hybrid Density Functional Theory Investigation. *J. Phys. Chem. C* **123**, 25668–25679 (2019).

28. Ganduglia-Pirovano, M. V., Da Silva, J. L. F. & Sauer, J. Density-Functional Calculations of the Structure of Near-Surface Oxygen Vacancies and Electron Localization on CeO_2 (111). *Phys. Rev. Lett.* **102**, (2009).

29. Penschke, C., Paier, J. & Sauer, J. Oligomeric Vanadium Oxide Species Supported on the CeO_2 (111) Surface: Structure and Reactivity Studied by Density Functional Theory. *J. Phys. Chem. C* **117**, 5274–5285 (2013).

30. Shishkin, M. & Ziegler, T. The Electronic Structure and Chemical Properties of a Ni/CeO_2 Anode in a Solid Oxide Fuel Cell: A DFT + U Study. *J. Phys. Chem. C* **114**, 21411–21416 (2010).

31. Ruiz Puigdollers, A., Schlexer, P., Tosoni, S. & Pacchioni, G. Increasing Oxide Reducibility: The Role of Metal/Oxide Interfaces in the Formation of Oxygen Vacancies. *ACS Catal.* **7**, 6493–6513 (2017).

32. Vicario, G., Balducci, G., Fabris, S., de Gironcoli, S. & Baroni, S. Interaction of Hydrogen with Cerium Oxide Surfaces: a Quantum Mechanical Computational Study. *J. Phys. Chem. B* **110**, 19380–19385 (2006).

33. Watkins, M. B., Foster, A. S. & Shluger, A. L. Hydrogen Cycle on CeO_2 (111) Surfaces: Density Functional Theory Calculations. *J. Phys. Chem. C* **111**, 15337–15341 (2007).

34. Chen, H.-T., Choi, Y. M., Liu, M. & Lin, M. C. A Theoretical Study of Surface Reduction Mechanisms of CeO_2(111) and (110) by H_2. *ChemPhysChem* **8**, 849–855 (2007).

35. García-Melchor, M. & López, N. Homolytic Products from Heterolytic Paths in H_2 Dissociation on Metal Oxides: The Example of CeO_2. *J. Phys. Chem. C* **118**, 10921–10926 (2014).

36. Negreiros, F. R., Camellone, M. F. & Fabris, S. Effects of Thermal Fluctuations on the Hydroxylation and Reduction of Ceria Surfaces by Molecular H_2. *J. Phys. Chem. C* **119**, 21567–21573 (2015).

37. Chafi, Z., Keghouche, N. & Minot, C. Density function theoretical study of interaction of hydrogen with ceria. *Phys. Procedia* **2**, 673–676 (2009).

38. Fernández-Torre, D., Carrasco, J., Ganduglia-Pirovano, M. V. & Pérez, R. Hydrogen activation, diffusion, and clustering on CeO_2 (111): A DFT+ U study. *J. Chem. Phys.* **141**, 014703 (2014).

39. Vilé, G., Bridier, B., Wichert, J. & Pérez-Ramírez, J. Ceria in Hydrogenation Catalysis: High Selectivity in the Conversion of Alkynes to Olefins. *Angew. Chem. Int. Ed.* **51**, 8620–8623.
40. Carrasco, J. *et al.* Molecular-Level Understanding of CeO_2 as a Catalyst for Partial Alkyne Hydrogenation. *J. Phys. Chem. C* **118**, 5352–5360 (2014).
41. Hirunsit, P. *et al.* Cooperative H_2 Activation at Ag Cluster/θ-Al_2O_3 (110) Dual Perimeter Sites: A Density Functional Theory Study. *J. Phys. Chem. C* **118**, 7996–8006 (2014).
42. Klacar, S. & Grönbeck, H. H_2 dissociation over Ag/Al_2O_3: the first step in hydrogen assisted selective catalytic reduction of NOx. *Catal. Sci. Technol.* **3**, 183–190 (2012).
43. Metiu, H., Chrétien, S., Hu, Z., Li, B. & Sun, X. Chemistry of Lewis Acid–Base Pairs on Oxide Surfaces. *J. Phys. Chem. C* **116**, 10439–10450 (2012).
44. van Santen, R. A., Tranca, I. & Hensen, E. J. M. Theory of surface chemistry and reactivity of reducible oxides. *Catal. Today* **244**, 63–84 (2015).
45. Wang, Y. *et al.* Catalysis with Two-Dimensional Materials Confining Single Atoms: Concept, Design, and Applications. *Chem. Rev.* **119**, 1806–1854 (2019).
46. Su, Y.-Q., Liu, J.-X., Filot, I. A. W. & Hensen, E. J. M. Theoretical Study of Ripening Mechanisms of Pd Clusters on Ceria. *Chem. Mater.* **29**, 9456–9462 (2017).
47. Pacchioni, G. Oxygen Vacancy: The Invisible Agent on Oxide Surfaces. *ChemPhysChem* **4**, 1041–1047 (2003).
48. Paier, J., Penschke, C. & Sauer, J. Oxygen Defects and Surface Chemistry of Ceria: Quantum Chemical Studies Compared to Experiment. *Chem. Rev.* **113**, 3949–3985 (2013).
49. Zhang, C., Michaelides, A., King, D. A. & Jenkins, S. J. Structure of gold atoms on stoichiometric and defective ceria surfaces. *J. Chem. Phys.* **129**, 194708 (2008).
50. Preda, G. & Pacchioni, G. Formation of oxygen active species in Ag-modified CeO_2 catalyst for soot oxidation: A DFT study. *Catal. Today* **177**, 31–38 (2011).

Chapter 6: O_2 Activation Over Ag-Decorated CeO_2 (111) and TiO_2(110): a Hybrid DFT Comparative Investigation.

6.1 Introduction

The activation of O_2 is a pivotal step involved in a plethora of oxidative processes[1].
These processes can occur on defective oxide surfaces, on ideal metal surfaces and on metal-metal oxide interfaces. In the case of metal oxides, oxygen vacancies are reaction centres for molecular oxygen, which weakly interacts with the ideal surfaces, but strongly adsorb on the superficial vacancies, where it is reduced to superoxide $*O_2^-$ or peroxide O_2^{2-}.
Upon the reduction, the O-O bond is weakened, facilitating the dissociation. This is a critical step for redox reactions following the Mars van Krevelen mechanism, where, upon the transfer of the O from the lattice to a substrate, the formed O vacancy requires to be regenerated in the catalytic cycle and typically this step involves the uptake of O_2 from the gas phase.
On metals instead, the interaction with O_2 depends highly from the electronic structure. Transition metals exhibit a moderate reactivity, which decreases with the occupation of the valence *d* band.
Due to the interest drawn from catalytic applications, the ceria-dioxygen interactions have been largely investigated[2,3,4,5]. Fully oxidised ceria weakly interacts with O_2, with physisorption occurring at T below 150 K. Reduced ceria samples with large surface area are instead much more reactive, and reduced oxygen species as peroxide ions and paramagnetic superoxide ions are detected with Raman and EPR spectroscopies (only $*O_2^-$). Recently, the different reactivity of the low index surfaces 111, 110 and 100 have been elucidated from a combined experimental/theoretical investigation: O_2 is reduced only on the 110 and 100 surfaces, where the vacancies are localized on the most external layer, instead on the 111, where the vacancy is stabilized on the subsurface layer, O_2 does not react[4]. Indeed, this can be true for regular and extended surfaces, while on shaped nano-particles O_2 reduction also occurs on the facets 111, but only peroxide forms[5,6].
According to the PBE+U calculations, the peroxide product is the most stable when two reduced Ce^{3+} are associated to the vacancy, but the metastable superoxide can form if one of the two Ce^{3+} is far enough from the vacancy to prevent the electron transfer (ET) to the O_2[3].
Describing the O_2 activation at metal, metal oxide or metal-metal oxide surfaces is a starting point to understand the oxygen reduction reaction in fuel cells[1,7]: with this aim, Wang *et al*[8] investigated the interaction between CeO_2 (111)/Ag and O_2, at the PW91 level, finding the reductive dissociation

of O_2 favoured both thermodynamically and kinetically at the three-phase-boundary (TPB) O_2-Ag-CeO_2, in the presence of O vacancies, with compared to regular Ag surfaces.
Ceria modified with silver has shown improved performance towards the soot oxidation, in comparison to ideal ceria, due to the possible increase of reduced oxygen species. Prada and Pacchioni[9] modelled the Ag-CeO_2 (111) by PBE+U calculations, finding that O_2 reduction to peroxide is thermodynamically favoured at the interphase O-vacancy with Ag_1 and Ag_5 clusters, but without evaluating the dissociation process, which has been left for further investigations.
TiO_2 is probably the most investigated metal-oxide[10], both by surface science and computational methods, since its prominent relevance in a wide variety of applications[11], especially in catalysis[12]. Most of the literature about TiO_2 interactions with O_2 concerns photocatalysis, where O_2 act as a scavenger for photogenerated electrons. On the rutile surface 110, the most investigated, O_2 adsorbs on the surficial vacancy at cryotemperature: up to 3 molecules adsorb, and superoxide is produced.[13] The presence of supported gold nanoparticles highly enhances the rate of the CO oxidation, where O_2 plays a key role in the activation process[14]. For the Ag/TiO_2 systems, similar findings have been reported[15].
In this chapter is reported the investigation of the O_2 interacting with ceria (111) and rutile (110) focused, in particular, on the role of the oxide support on the activation of O_2 at the interphase support-silver cluster.

6.2 Model and computational details

All calculations have been performed with spin-polarized DFT, adopting the global hybrid PBE0[16] functional with an atom-centred GTO basis set, as implemented in the code Crystal17[17].
The PBE0 functional well reproduces ceria-based system properties, as shown in the previous chapters, and it has been proven to be accurate for the TiO_2 rutile and anatase phases, both bulk[18] and low-index surfaces[19], for the reduced oxide Ti_2O_3[20,21], for oxygen vacancies in TiO_2 bulk phases[22] and for nanoparticles[23].
Dispersion effects were considered with the semi-empirical D3 correction scheme, as in the previously reported work.
The *p*(4x4) slab model used in the previous study[24] for the CeO_2 (111) and Ag_{10}/CeO_2 (111) systems has been considered in this study too. The model of the surface 110 of TiO_2, a supercell *p*(5x2) of the unit cell, has been cut from the bulk of the rutile (optimized lattice parameters *a* and *b* of 4.582 and 2.956 Å). This supercell size has been chosen to be comparable with the supercell of CeO_2, in order to have similar distances between O vacancies and adatoms species in the periodic images of the cell.

The supercell thickness corresponds to 3 Ti-layers. Each Ti-layer is then composed by 3 planes with the motif O-Ti_2O_2-O (see **Figure 1**). Only add-atoms and the topmost 2 Ti-layers have been allowed to relax, while the atoms in the bottom Ti-layer were frozen to their bulk positions. Similarly, for the CeO_2 systems, only the bottom 3 atomic layers have been kept frozen to simulate the bulk.
The Irreducible Brillouin Zone has been sampled with a regular Monkhorst-Pack grid 2 x 2 x 1 (4 **k** points) in both ceria and rutile systems. A threshold of 10^{-7} a.u. has been used for the convergence of the total energy in the SCF procedure for all the single point energy and geometry optimization calculations, while a tighter value of 10^{-10} a.u. was used for the transition state searches and for the frequency calculations. The Coulomb and the exchange series have been truncated with threshold values of 10^{-8}, 10^{-8}, 10^{-8}, 10^{-8}, and 10^{-20} for the CeO_2 containing systems, while the default threshold values 10^{-7}, 10^{-7}, 10^{-7}, 10^{-7}, and 10^{-14} has been retained accurate enough for the TiO_2 containing systems.
As previously shown for cerium oxide[25], well converged structural properties can be obtained with relatively small basis set, tailored to describe the condensed phase, while energetics associated to the redox process of interests may require a more extended and flexible basis set to obtain converged results.
For the CeO_2 based systems, the basis set 1 (BS1) and 2 (BS2) adopted in the previous chapter has been used, here labelled $BS1_{CeO2}$ and $BS2_{CeO2}$. For the TiO_2 based systems we have employed two distinct basis sets as well, $BS1_{TiO2}$ and $BS2_{TiO2}$, defined as following: in BS1, Ti and O have been described with all-electron basis sets, with contractions schemes (20s12p4d)/[5s4p2d] and (14s6p1d)/[4s3p1d], respectively, with exponents of the outer *s*, *p*, and *d* primitives optimized on the structures of rutile and anatase[19]. For $BS2_{TiO2}$, Ti was described by a larger contraction (20s12p6d3)/[5s4p4d], obtained removing the *f* contraction from the original version[26] and including an additional diffuse primitive *d* (exponent = 0.12) while the basis set of O was the same adopted for $BS2_{CeO2}$.
$BS1_{CeO2}$ and $BS1_{TiO2}$ were used to perform all the geometry optimizations and in the subsequent frequency calculation at the Γ point to verify the found minima or saddle-point. The $BS2_{CeO2}$ and $BS2_{TiO2}$ were used to perform single points calculations on selected structures, preoptimized with BS1.
In the following text, all the reported energies have been computed with the BS1 with the inclusion of the D3 correction, except when stated otherwise.
The transition state search and the characterization of the stationary points of the PES has been performed following the same procedure described in the previous chapter.

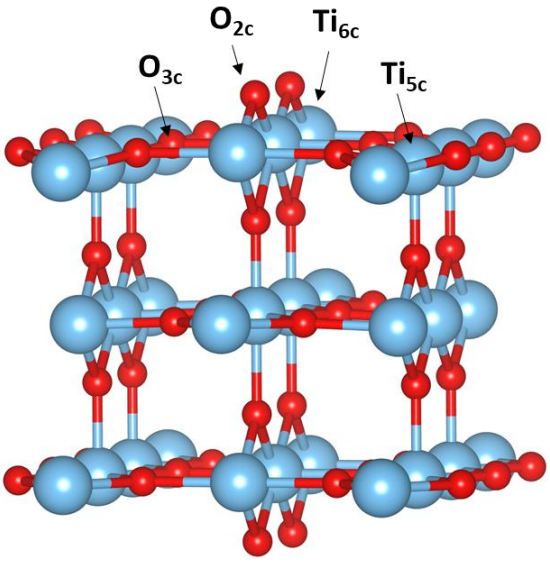

Figure 1: 3 Ti-Layer slab model of the rutile (110) surface. The different coordination of surface O and Ti atoms are indicated by arrows.

6.3 Results and discussion

6.3.1 Ag_{10} on the stoichiometric surfaces.

In this work we consider the adhesion of the Ag_{10} cluster model described in the previous chapter on TiO_2 (110), and the results will be compared with the results obtained on CeO_2 (111). The orientation for the adsorption of the cluster has been selected in order to maximize the interaction between the Ag and the bridge O atoms(O_{2v}) of the surface.

Without magnetizations constrains, a transfer of 3 e^- from the cluster to the oxide occurs: three Ti^{3+} are localized in the second Ti layer. As for the reduction of Ce^{4+} to Ce^{3+}, Ti^{3+} ions are distinguished from Ti^{4+} by a net magnetization, evaluated from the Mulliken's spin population, which ranges between 0.77 and 0.81 μ_B for the reduced ions. After the reduction of the surface, the other Ti^{4+} ions exhibit a small magnetization, no higher than 0.08. The cluster acquires a charge of 1.75 $|e^-|$ and a magnetization of 0.92 μ_B.

This difference with respect to the Ce is ascribed to the larger spatial extension of the occupied 3*d* orbitals of the Ti, compared to the 4*f*. The FM configuration with all the spin aligned and total magnetization of 4 μ_B was found only 0.02 eV more stable than the AFM configuration. **Figure 2** depicts the spin density map (panel a) and the density of states (panel b) associated to the FM solution. The spin density localizes at the Ti^{3+} centres on the 3*d* states, which appear in the main gap of the oxide.

Further calculations with a cell magnetization of 6 μ_B have been performed to evaluated the possibility of a further electrons transfer cluster to slab: the solution obtained, containing 4 Ti^{3+}, was 1.60 eV less stable than the former, therefore we concluded that a transfer of 3e^- from cluster to

oxide was the most favoured for both the oxides here considered. As for the CeO_2 case, there are no other minima close in energy.

The computed adsorption energy is of -2.98 eV. By including the dispersion correction D3, the stability of the adsorbate increases to -5.54 eV. These results are very similar to the ones obtained for Ag_{10} on CeO_2(111), where the adsorption energies are of -3.11 and -5.55 eV for uncorrected and dispersion correction, respectively.

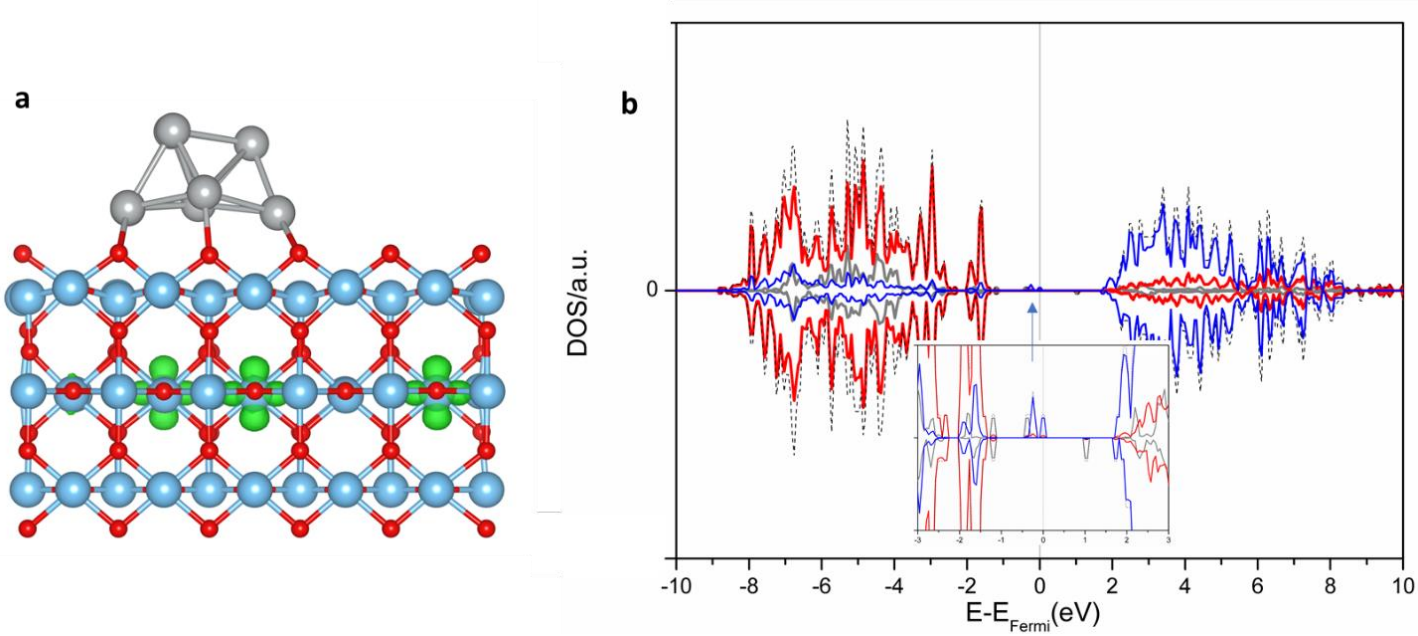

Figure 2: FM solution to the adsorbed Ag_{10} on TiO_2 (110): a) Spin density map (isocontour value 0.01 atomic unit); b) total (dotted black line) and atom-projection contributions to density of states, with O, Ti and Ag contributions in red, blue and grey, respectively.

6.3.2. O vacancies formation.

The computed formation energies of the V_O (E_{fv}) are reported in **Table 1**. For the CeO_2 case, the same Vo reported in the previous chapter are reconsidered.

For the TiO_2 case, we report the two configurations of the Ti^{3+} obtained for the surface Vo (bridge site O_{2v}) at the clean surface, the NN_{1st} -NN_{1st} and the NN_{2nd} -NN_{2nd} (1^{st} and 2^{nd} are the positions with respect to the cationic layer).

In the case of TiO_2(110), the most reactive O is the undercoordinated bridging O_{2v}. An O vacancy forms on this site with the reduction of two Ti^{4+} to Ti^{3+}, that can localize on the first or in the second cationic layer of the surface, in the first or in the second cationic shell with respect to the vacancy. Without imposing constrains of magnetizations, the most stable solution was found, with both the Ti^{3+} in the second Ti layer (see **Figure 2**, panel a), in the second coordination shell with respect to the V_O (NNN_{2nd} -NNN_{2nd}), in agreement with previous results[27] .The other configuration stabilized was the NN_{1st} -NN_{1st} , here not depicted, with both the Ti^{3+} in the first coordination shell of the Vo, characterized by a much higher energy of formation (5.65 eV) respect the NNN_{2nd} -

NNN_{2nd}. The defect states appear in the DOS (see **Figure 3**, panel b), as sharp peak above the top of the O 2*p* valence band.

The V_O formation on Ag_{10}/TiO_2 at a surface site (O_S), occurs with the formation of a single Ti^{3+} in the nearest neighbour shell (NN_{1st}), while the residual electron is transferred to the cluster, as observed by the total charge decrease from 1.75 to 1.16 |e-|. Similarly, the V_O at an interphase site (O_I) forms followed by a single additional Ti^{3+}, but in the next nearest neighbour shell (NNN_{1st}), and a similar reduction of the cluster charge (1.14 |e-|). For both sites, the E_{fv} is higher than on the clean TiO_2 surface, likely due to the high concentration of Ti^{3+} in the second Ti-layer, which prevent a further reduction of the Ti^{4+} in the same layer. The formation of the V_O at the interphase site resulted favoured, at difference with the same type of V_O on Ag_{10}/CeO_2. In this case, the Ag atom at the edge of the cluster is not drawn into the vacancy site, but it relaxed upward, and the reduced Ti is in NNN-NNN position with respect to the V_O, and both factors stabilize the obtained solution. This behaviour agree with the vast majority of the metal-metal oxide supported interfaces investigated[28], with only CeO_2 which stand-out, independently by the supported metal.

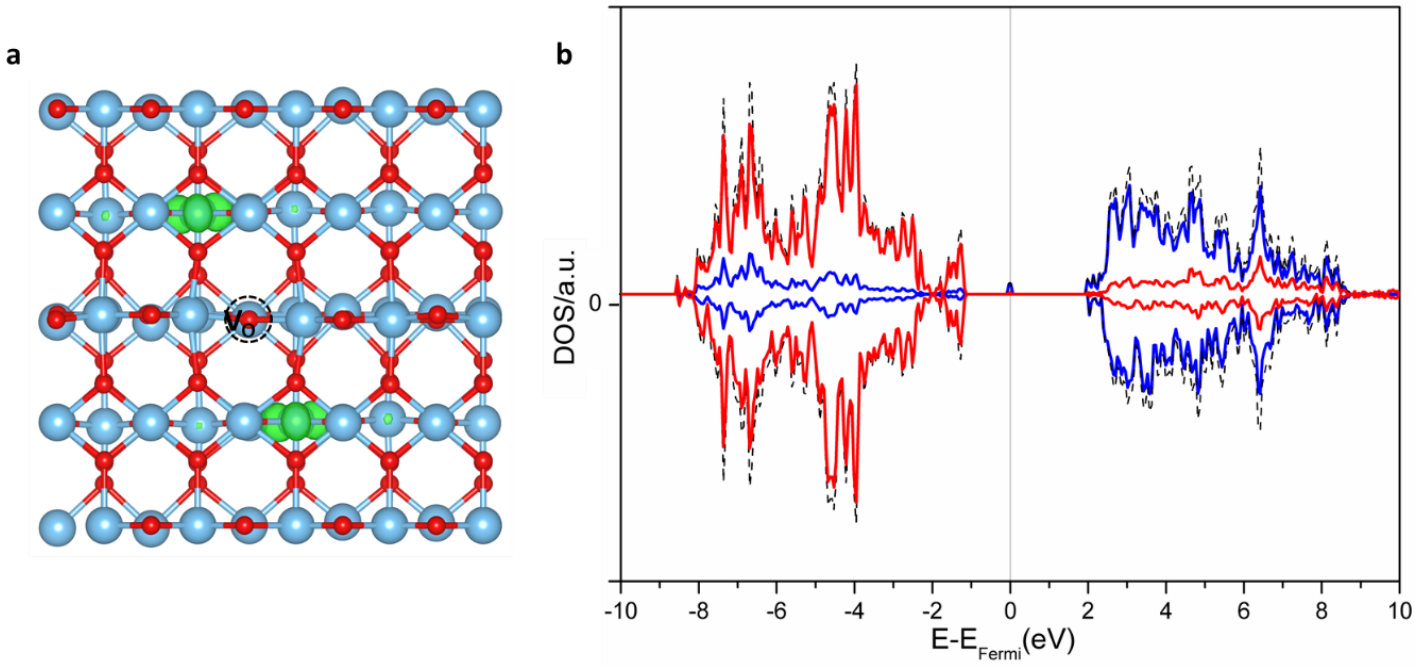

Figure 3: FM solution for the V_O at surface site O_{2c} TiO_2 (110), with NNN_{2nd}-NNN_{2nd} configuration of the localized Ti^{3+} centres: a) Spin density map (isocontour value 0.01 atomic unit); b) total (dotted black line) and atom-projection contributions to the density of states.

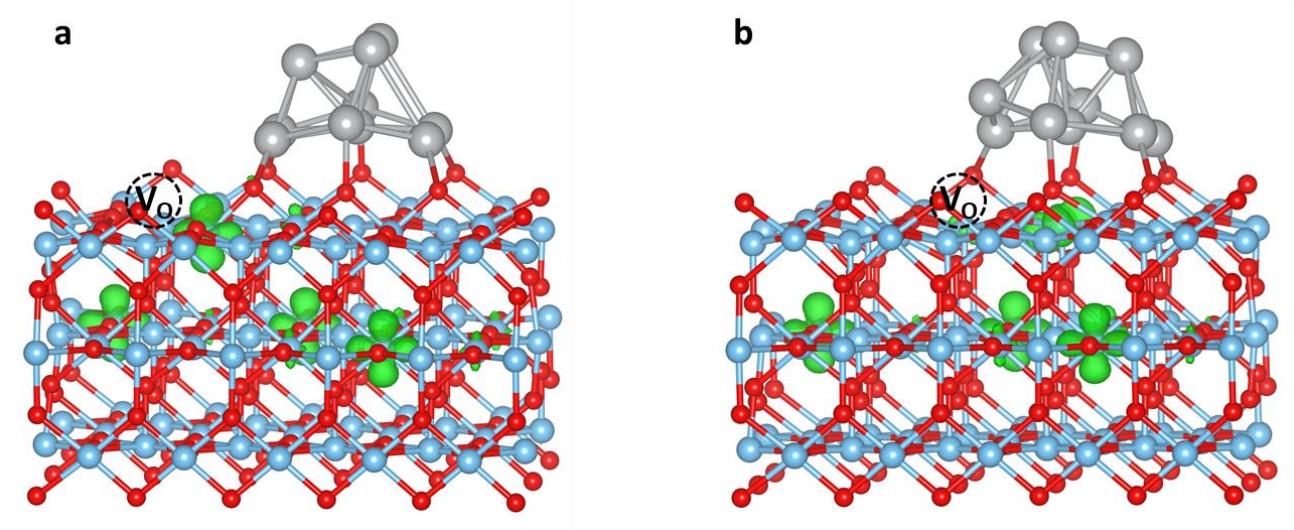

Figure 4: Spin density map of the FM solutions for the V_O at surface site O_S (a) and at interphase site O_I (b).

Table 1. Computed formation energies (E_{fv}, in eV) of the surface V_O with respect to ½ O_2 at different sites for the CeO_2(111), Ag_{10}/CeO_2 (111), TiO_2 (110) and Ag_{10}/TiO_2(110) systems, along with the number of Me^{3+} obtained (N Me^{3+}, Me=Ce/Ti), the average spin population of the Me^{3+} ions (M, in $|\mu_B|$), and the total charge associated to the metal cluster (Q_C, in $|e^-|$).

System	Site/configuration	N Me^{3+}	M	Q_C	E_{fv}
CeO_2	O_S	2	0.971	-	3.34
Ag_{10}/CeO_2	O_S	5	0.979	1.35	3.30
Ag_{10}/CeO_2	O_I	4	0.966	0.93	3.62
TiO_2	(NN_{1st} -NN_{1st})	2	0.845	-	5.55
TiO_2	(NNN_{2nd} -NNN_{2nd})	2	0.751	-	2.31
Ag_{10}/TiO_2	O_S/ NN_{1st}	4	0.843	1.16	3.61
Ag_{10}/TiO_2	O_I/NNN_{1st}	4	0.892	1.19	2.95

6.3.3 O_2 on the stoichiometric surfaces.

The first step in the O_2 activation is the mechanism of interaction between the gas phase O_2 and the oxide surface. On the clean surfaces, O_2 adsorbs physically at cryogenic temperature, below 150 and 100 K for CeO_2 (111) and TiO_2 (110), respectively. Without dispersion correction the adsorption energies are negligible, respectively -0.02 and 0.01 eV, in close agreement with

previous works.[29,30] The inclusion of the dispersion correction increases the stability of the adsorbates to -0.15 and -0.18 eV.

6.3.4 O_2 on the defective surfaces.

Defect centres on oxide surfaces are among the most reactive sites for many reactions; in the case of oxygen vacancies (V_O), the affinity for the oxygen is exceptionally high. The positive potential of the vacancy draws-in the highly electronegative O_2 which refills the vacancy.

The process is accompanied by the reduction of the molecule, which involves electron transfer from the reduced cations Ce^{3+}/Ti^{3+} to the semi-occupied π^* orbitals of dioxygen, with the formation of superoxide ($*O_2^-$) or peroxide (O_2^{2-}), depending on the number of transferred electrons.

As consequence, the O-O bond is elongated and weakened: while one O restore the vacancy, the other can be transferred to a substrate or migrate on the surface.

On polycrystalline samples, as well as on single crystals exposing the surfaces 110 and 100 of reduced CeO_2, the exposition to O_2 produces both the reduced species. On single-crystal CeO_2 (111), neither superoxo or peroxo species are observed, being the surface vacancies concentrated in the subsurface layer and not accessible to the O_2, which instead weakly adsorbs on the surface, without the occurrence of an electron transfer. On shaped nanoparticles exposing preferentially the 111 facets, instead, peroxide species are observed, being probably available the surface vacancy sites. No superoxide species form at defects on CeO_2 (111), except for at vacancies associated to a trivalent dopant, and consequently, to a single Ce^{3+}. On the other defective low index facets, 110 and 100, superoxide forms being available, deep under the surface, stable Ce^{3+} configurations further from the vacancy site, therefore is likely that the ET from Ce^{3+} to $*O_2^-$ is hindered by a higher barrier.

In O defective rutile (110), the O_2 interacts strongly with the surface vacancy and may form superoxo, peroxo or dissociated oxide ions (O^{2-}).[31] While the latter process seems thermodynamically more favourable, according to calculations and in agreement with the STM results[32], for the other two species, there is no experimental evidence for a preference. In a DFT investigation at the PBE level, Chrétien and Metiu[33] took into account the spin-conservation rule[33] to exclude if the favoured reaction path is characterized by a singlet or triplet state, differentiated for the formation of peroxide and superoxide. They accounted for the adsorption, migration, reduction and dissociation of O_2: all the stationary points along the singlet path lie lower in energy, but all the activation energies are smaller by 0.3 eV or more in the triplet path, which resulted also energetically favoured.

The authors concluded that the calculated small barrier for the dissociation of the superoxide is more in agreement with experiments, in comparison with the results on the peroxide. However, in these conclusions, they did not consider the experimental evidence of multiple dioxygen molecules interacting on a single vacancy site, even at cryotemperature[10], which are likely to react with a different mechanism.

At difference from the case of the ceria, on rutile, the O_2 molecule is reduced without being directly bound to the vacancy, which leads to a number of possible adsorption sites near the vacancy[34] and successive migration of the molecule on the oxide towards the vacancy. Here only direct adsorption at the vacancy is considered since it is energetically more favoured with respect to any other sites.

6.3.4.1 CeO_2

In the case of CeO_2 (111) the adsorption of the molecule occurs with one of the two O filling the surface vacancy and the other tilted with respect to the surface plane. In the process of adsorption, an electron transfer from Ce^{3+} to O_2 occurs reducing the molecule.

Previous DFT investigations[4] have found the ET occurs only if the O_2 adsorbs directly into the vacancy: any other adsorption site (on top of Ce^{3+} or Ce^{4+}, nearest neighbour or next nearest neighbour to the vacancy resulted in weak physisorption, with only a small charge polarization of the molecule.

The adsorption of O_2 at the vacancy with two nearest-neighbour Ce^{3+} results in a double ET to the O_2, reduced to peroxide, with the system becoming closed-shell after pairing of all the radical centres. Constraining the magnetization to 2 μB, instead, leads to a single ET and the reduction of the O_2 to superoxide, a solution 1.03 eV less stable than the previous one.

The observation of both reduced O_2 species can be explained if the adsorption occurs at different O vacancy sites, characterized by different spatial distributions of the Ce^{3+} ions, and provides preferentially one or other species. In the case of the NN-NN configuration, the unconstrained calculation provides the peroxide, while in the case of a NN-NNN and a NNN-NNN configuration, only a single ET occurs, providing the superoxide. These results suggest that the second ET has an associated barrier, affected by the distance donor-acceptor. The first ET, instead, occurs regardless of the position of the donor Ce^{3+}, but it requires the interaction of the O_2 with the vacancy, suggesting that this process is associated with a very small barrier. At finite temperature, Ce^{3+}configurations can change due to polaron hopping, with an associated barrier of about 0.2-0.4 eV[35,36,37], leading eventually to the electron donor Ce^{3+} in NN position with respect to the adsorbed superoxide, and to the final reduction to peroxide. Stable superoxide species are predicted to form

from the interaction of O_2 with undercoordinated and isolated Ce^{3+} ions, as computed on irregular surfaces as ceria nanoparticles[38] or with vacancies associated to trivalent cations dopants[3].
Here we limit to consider the dissociation of the peroxide.
After the reduction, the process of the O-O dissociation and migration of O is accounted for. The surface O moves towards one of the three neighbouring Ce and then is transferred over another surface O to form a peroxo species, identical to the starting configuration. The process necessitates thermal activation to overcome the high barrier (1.82 eV).

6.3.4.2 TiO_2

On r-TiO_{2-x} (110), the O_2 adsorbs on the bridge O_{2c} surface V_O with a parallel orientation with respect to the surface, in the most stable orientation[30,33,39]. Unconstrained calculations provided the product of the double ET, with the oxidation of the two Ti^{3+} centres and formation of peroxide (see **Figure 5**, 2nd bottom panel).
The single ET which provides the adsorbed superoxide is obtained constraining the magnetization to 2 μ_B to prevent the pairing of the radicals localized on Ti^{3+} and on O_2^-. Similarly, to the CeO_2 case, the resulting superoxide is much more unstable than the peroxide, 1.28 eV higher in energy.
Here the dissociation of the O_2 in the most stable form, the peroxide, is considered. The process occurs with one of the two O replacing the $O_{2v,}$ while the other migrate towards the $Ti_{5v.}$ The process occurs with a barrier of 2.06 eV, with the dissociation product more stable with respect to the adsorbed form by -0.20 eV.

Table 2. The computed energy of formation of the V_O E_{fv} (eV), the energy of adsorption of the O_2 molecule E_{ads} (eV), the charge acquired by O_2 Q (|e^-|) and the interatomic distance d O-O (Å).

System	E_{fv}	E_{ads}	Q O_2	d O-O
CeO_2	3.45	-3.42	-1.19	1.465
Ag_{10}/CeO_2 O_I	3.76	-3.89	-1.27	1.496
TiO_2	2.39	-1.58	-0.94	1.418
Ag_{10}/TiO_2 O_I	3.08	-2.57	-1.03	1.443

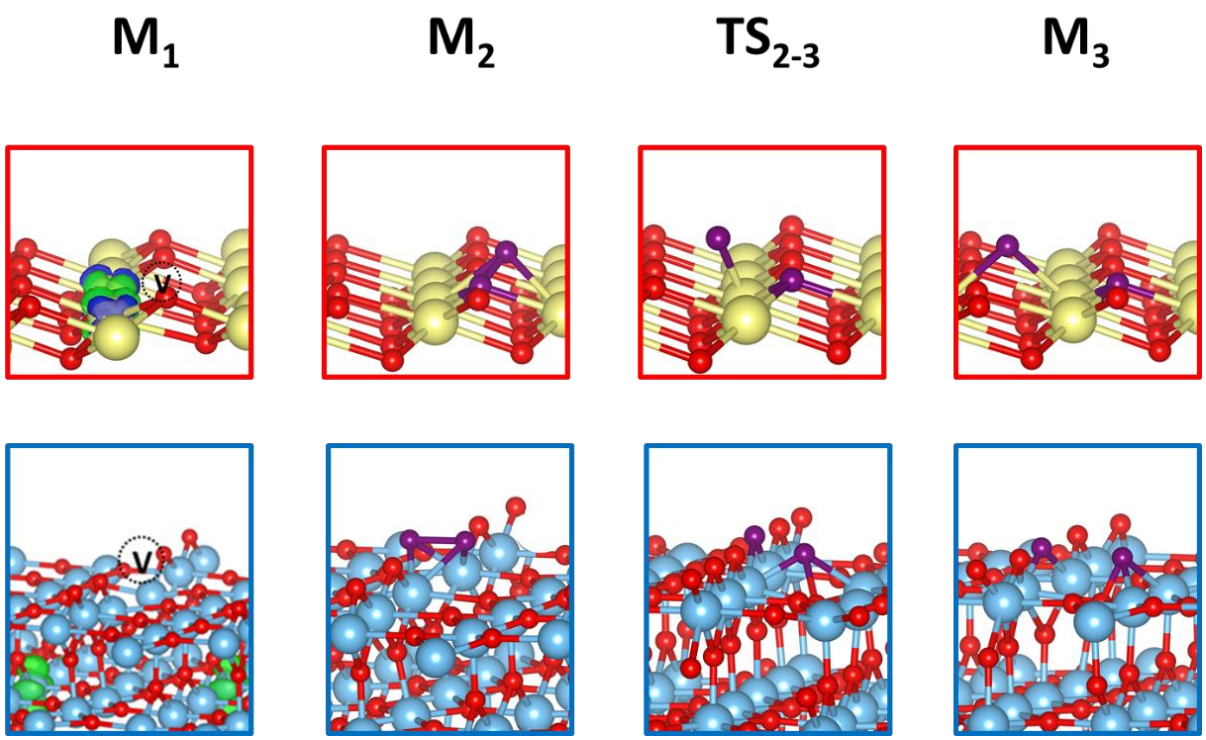

Figure 5: Side view of the optimized structures associated to the adsorption and dissociation of O_2 at an oxygen vacancy on (top panels) CeO_2 (111) and (bottom panels) TiO_2 (110). In green/blue the positive/negative spin densities (isocontour values of 0.01 a.u.).

6.3.5 O_2 interaction with reduced Ag_{10}/CeO_2 and Ag_{10}/TiO_2.

After investigating the O_2 adsorption and reduction on the unmodified surfaces, the interaction with the silver decorated surfaces is considered. This investigation is limited to the case of a V_O peripherical at the metal-oxide interphase, specifically the reaction site is the interphase vacancy itself. This choice is justified by the higher affinity of the V_O for the O_2, as shown in other works of metal clusters supported on oxide which considered several adsorption sites. In particular, Preda and Pacchioni[9] investigated the adsorption of O_2 on Ag_1/CeO_2, Ag_1/CeO_{2-x} and Ag_5/CeO_{2-x}, finding that the presence of the defect is necessary to obtain the reduction of the O_2.[9] Similarly, for the Ag_8/TiO_2 system, the O_2 adsorption and dissociation are thermodynamically favoured at V_O in positions O_I and O_S, compared to the process at the cluster surface or TPB in the absence of V_O[40]. Unfortunately, the work did not consider spin polarization, making the trends obtained from the computed barriers much less reliable than the corresponding reaction energies.

On both the considered Ag-oxide system, the O_2 adsorption occurs readily at the vacancy site with an end-on orientation of the molecule. Differently from the results of Preda and Pacchioni for the smaller cluster Ag_5 on defective ceria, the O_2 adsorbed without displacement of the cluster from the initial position and consequently, the adsorbed O_2 is exposed at the TPB. The reason is likely due to

the stronger adhesion of the larger cluster here considered. This description does not change if dispersion correction is not included, as in the compared work.

The reduction provided in both cases two adsorbed peroxide molecule, which formally receives an electron from the cluster and the other from one Me^{3+}; in the case of TiO_2 the Ti^{3+} donor is the one closer to the surface. Both adsorption processes are much favoured with respect to the V_O formation, at difference from the adsorption on unmodified surfaces vacancies, which recover the vacancy formation cost. Therefore, the adsorption of atomic O is favoured in the presence of Ag.

The same approach used to search the single ET Me^{3+} to O_2 on the unmodified surface has been attempted in the presence of the cluster. Despite many computational settings tried, no solution was found with the O_2 reduced to superoxide at the interphase oxide-cluster: the O_2 was always in peroxide form, while the variation of the magnetization affects only the ET cluster to oxide.

The dissociation of the O_2 molecule involves the transfer of the upper O to the surface of the cluster: to find the preferential site of adsorption on the cluster, a relaxed scan along the O-O bond distance was performed, to approximate the reaction path. The dissociated O bind in both cases to a threefold site of the cluster, but with much more structure reorganization on the TiO_2 system.

In **Figure 6** are depicted the structures of the located minima and transition states for the reaction paths considered.

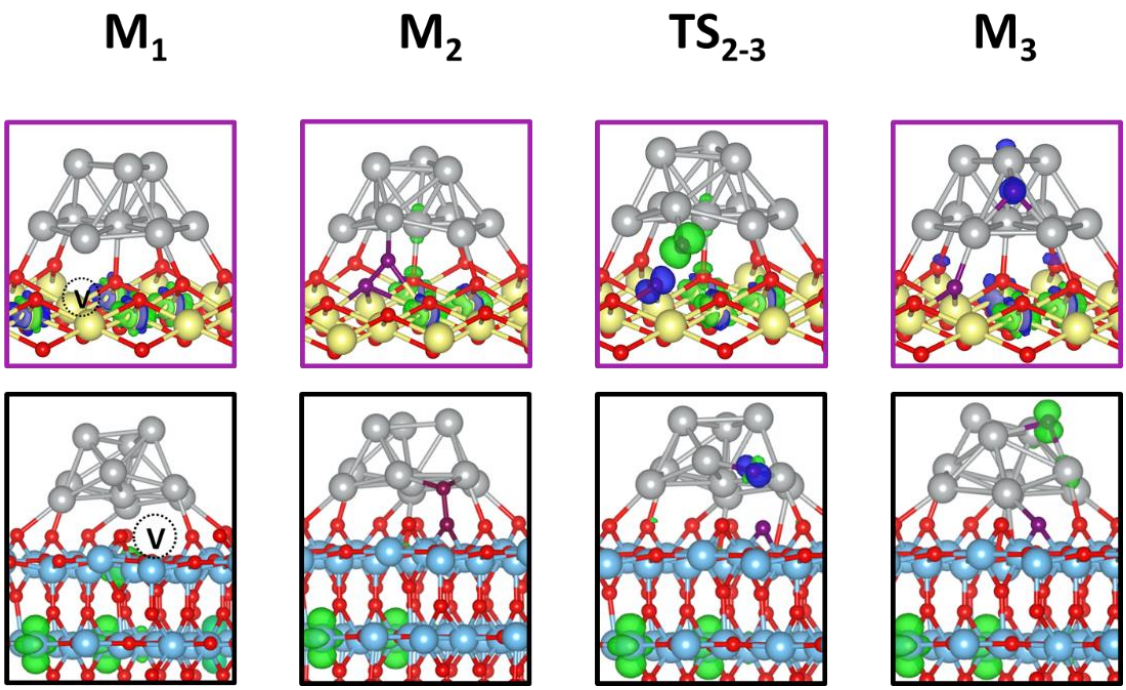

Figure 6: Views of the optimized structures associated to the adsorption and dissociation of O_2 at the interphase oxygen vacancy on (top panels) Ag_{10}/CeO_2 (111) and (bottom panels) Ag_{10}/TiO_2 (110). In green/blue the positive/negative spin densities (isocontour values of 0.01 a.u.)

The optimized TS structures were confirmed by the computed imaginary frequency related to the O transfer, with associated dissociation barriers of 0.95 and 1.59 eV for the CeO_2 and TiO_2 systems respectively, while the processes result more exothermic on the TiO_2 support: -1.73 eV, with respect to -0.90 eV on the CeO_2 support. The **Figure 7** compares the computed reaction profiles.

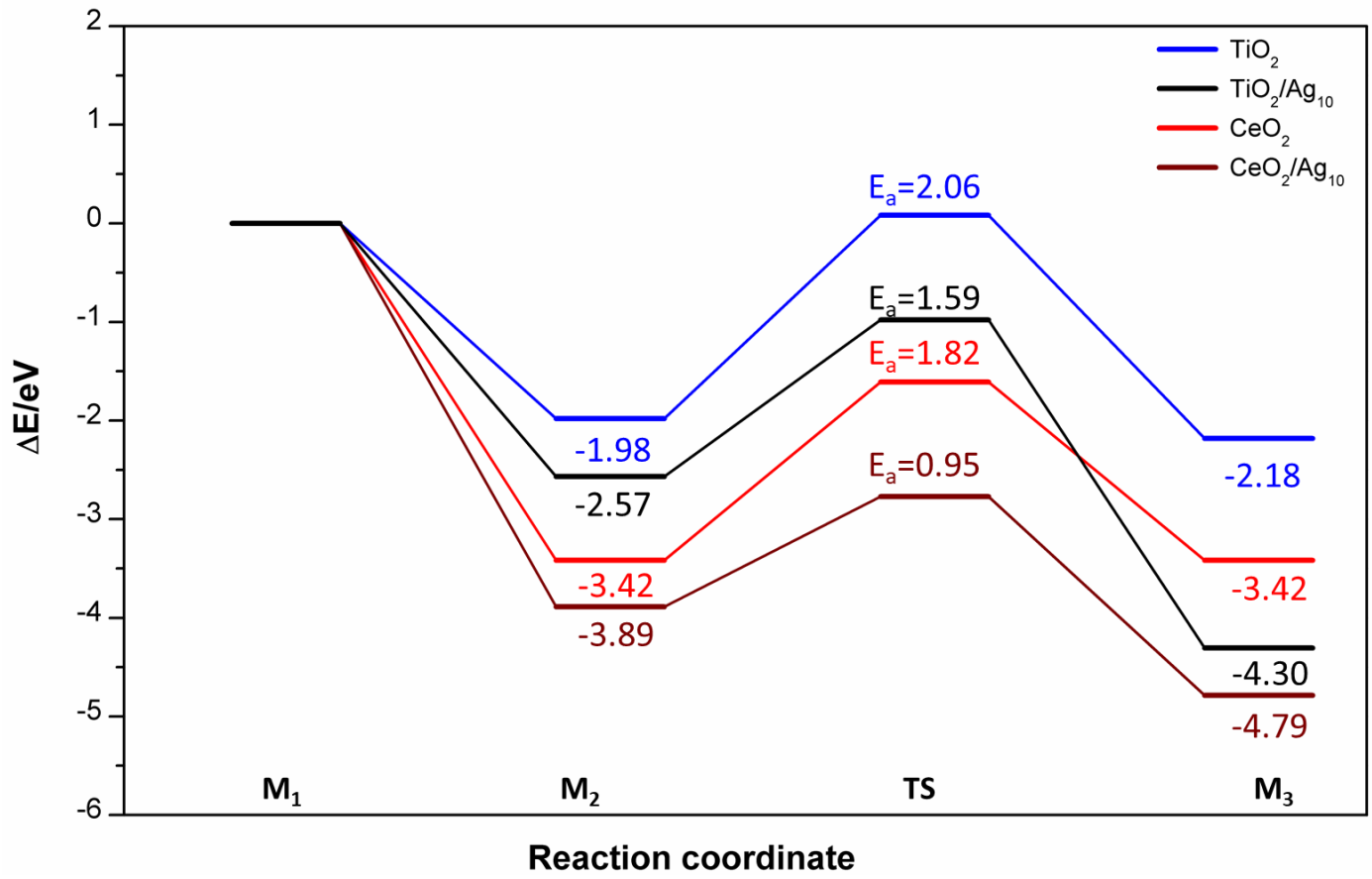

Figure 7: Energies profiles for the reaction paths of O_2 adsorption and dissociation at O vacancies sites on the systems CeO_2, TiO_2, Ag_{10}/CeO_2 and Ag_{10}/TiO_2.

The explanation for these differences relies on the intrinsic properties of the surface morphology and electronic structures. First, the V_O vacancy in ceria is a stronger reductant: the O_2 reductive adsorption is favoured on the ceria support, where the adsorption energy almost recovers the cost to form the vacancy. Moreover, according to the computed charges (see **Table 2**), the O_2 is reduced to a higher degree on the ceria support. This aspect is correlated with the longer O-O bond, suggesting a weaker bond with respect to the rutile case. The presence of the cluster favours in both the cases the reduction of O_2 at a higher extent. These trends are confirmed in the TS structures on the silver supporting surfaces (the case of the clean surfaces is not considered, being the morphology different) where the O-O distance is 0.21 Å longer in the CeO_2/Ag_{10} case.

The higher exothermicity for the O_2 dissociation on Ag_{10}/TiO_2 is instead a consequence of the structural rearrangement of the cluster after the uptake of the dissociated O atom, which occurs with the loss of the former rigid hemispherical shape. The flexibility of the cluster is indeed pivotal in characterizing its reactivity, as was reported by Negreiros and Fabris[41] for Pt clusters supported on ceria (111). Different supports and topologies of the surface, as the case here considered, are likely to stabilize the cluster morphology differently. Nevertheless, global optimization of all the structures here considered was beyond our calculation possibility, at the level of theory adopted. On both supports, the silver enhanced the reaction which were to elucidate the effects of the electronic structure of the junction silver-oxide on the reactivity.

6.4 Conclusions

In this chapter, the O_2 adsorption, reduction and dissociation at oxygen vacancy sites have been considered on CeO_2 (111) and TiO_2 (110), both with and without a supported Ag_{10} cluster.
The adsorption of O_2 on the ceria systems resulted favoured compared to the TiO_2 systems, with a higher degree of reduction of the O_2 molecule on ceria, and consequently, a weaker O-O bond. This has been confirmed by the smaller activation energies for the dissociation of O_2 on the ceria systems.
The silver cluster favours the dissociation at the interphase vacancy, the most reactive site, with compared to the surface, and stabilizes the dissociated atomic O, which, possessing a radical character, is expected to be more easily transferred.
The same supported cluster of hemispherical shape has been used in order to elucidate the effects on the reactivity as a function of the electronic structure only. However, the flexibility of the structure influences the reactivity, and the support affects this property. The account of this aspect is at present too computational demanding at the level of theory here adopted, but a multi-layered theoretical approach could be adopted to make the problem tractable. The adsorption energy of O_2 on the vacancies sites is inversely correlated with the dissociation barrier, which would make it a predictive descriptor for the reactivity, but further investigations are required to with more oxides surfaces.

6.5 References

1. Montemore, M. M., van Spronsen, M. A., Madix, R. J. & Friend, C. M. O_2 Activation by Metal Surfaces: Implications for Bonding and Reactivity on Heterogeneous Catalysts. *Chem. Rev.* **118**, 2816–2862 (2018).

2. Choi, Y. M., Abernathy, H., Chen, H.-T., Lin, M. C. & Liu, M. Characterization of O_2–CeO_2 Interactions Using In Situ Raman Spectroscopy and First-Principle Calculations. *ChemPhysChem* **7**, 1957–1963 (2006).

3. Conesa, J. C. Surface anion vacancies on ceria: Quantum modelling of mutual interactions and oxygen adsorption. *Catal. Today* **143**, 315–325 (2009).

4. Yang, C. *et al.* O_2 Activation on Ceria Catalysts—The Importance of Substrate Crystallographic Orientation. *Angew. Chem. Int. Ed.* **56**, 16399–16404 (2017).

6. Wu, Z., Li, M., Howe, J., Meyer, H. M. & Overbury, S. H. Probing Defect Sites on CeO2 Nanocrystals with Well-Defined Surface Planes by Raman Spectroscopy and O2 Adsorption. *Langmuir* **26**, 16595–16606 (2010).

6. Schilling, C., Ganduglia-Pirovano, M. V. & Hess, C. Experimental and Theoretical Study on the Nature of Adsorbed Oxygen Species on Shaped Ceria Nanoparticles. *J. Phys. Chem. Lett.* **9**, 6593–6598 (2018).

7. Choi, Y., Mebane, D. S., Wang, J.-H. & Liu, M. Continuum and Quantum-Chemical Modeling of Oxygen Reduction on the Cathode in a Solid Oxide Fuel Cell. *Top. Catal.* **46**, 386–401 (2007).

8. Wang, J.-H., Liu, M. & Lin, M. C. Oxygen reduction reactions in the SOFC cathode of Ag/CeO_2. *Solid State Ion.* **177**, 939–947 (2006).

9. Preda, G. & Pacchioni, G. Formation of oxygen active species in Ag-modified CeO_2 catalyst for soot oxidation: A DFT study. *Catal. Today* **177**, 31–38 (2011).

10. Diebold, U. The surface science of titanium dioxide. *Surf. Sci. Rep.* **48**, 53–229 (2003).

11. Dahl, M., Liu, Y. & Yin, Y. Composite Titanium Dioxide Nanomaterials. *Chem. Rev.* **114**, 9853–9889 (2014).

12. Bagheri, S., Muhd Julkapli, N. & Bee Abd Hamid, S. Titanium Dioxide as a Catalyst Support in Heterogeneous Catalysis. *Sci. World J.* **2014**, (2014).

13. Henderson, M. A., Epling, W. S., Perkins, C. L., Peden, C. H. F. & Diebold, U. Interaction of Molecular Oxygen with the Vacuum-Annealed TiO_2(110) Surface: Molecular and Dissociative Channels. *J. Phys. Chem. B* **103**, 5328–5337 (1999).

14. Teng, B.-T. *et al.* O_2 Adsorption and Oxidative Activity on Gold-Based Catalysts with and without a Ceria Support. *J. Phys. Chem. C* **117**, 18986–18993 (2013).

15. Frey, K., Iablokov, V., Melaet, G., Guczi, L. & Kruse, N. CO Oxidation Activity of Ag/TiO_2 Catalysts Prepared via Oxalate Co-precipitation. *Catal. Lett.* **124**, 74–79 (2008).

16. Adamo, C. & Barone, V. Toward reliable density functional methods without adjustable parameters: The PBE0 model. *J. Chem. Phys.* **110**, 6158–6170 (1999).

17. Dovesi, R. *et al.* Quantum-mechanical condensed matter simulations with CRYSTAL. *Wiley Interdiscip. Rev. Comput. Mol. Sci.* e1360 (2018) doi:10.1002/wcms.1360.
18. Labat, F., Baranek, P., Domain, C., Minot, C. & Adamo, C. Density functional theory analysis of the structural and electronic properties of TiO_2 rutile and anatase polytypes: Performances of different exchange-correlation functionals. *J. Chem. Phys.* **126**, 154703 (2007).
19. Labat, F., Baranek, P. & Adamo, C. Structural and Electronic Properties of Selected Rutile and Anatase TiO_2 Surfaces: An ab Initio Investigation. *J. Chem. Theory Comput.* **4**, 341–352 (2008).
20. Hu, Z. & Metiu, H. Choice of U for DFT+U Calculations for Titanium Oxides. *J. Phys. Chem. C* **115**, 5841–5845 (2011).
21. Gerosa, M. *et al.* Electronic structure and phase stability of oxide semiconductors: Performance of dielectric-dependent hybrid functional DFT, benchmarked against G W band structure calculations and experiments. *Phys. Rev. B* **91**, (2015).
22. Spreafico, C. & VandeVondele, J. The nature of excess electrons in anatase and rutile from hybrid DFT and RPA. *Phys Chem Chem Phys* **16**, 26144–26152 (2014).
23. Morales-García, Á., Lamiel-García, O., Valero, R. & Illas, F. Properties of Single Oxygen Vacancies on a Realistic $(TiO_2)84$ Nanoparticle: A Challenge for Density Functionals. *J. Phys. Chem. C* **122**, 2413–2421 (2018).
24. Brugnoli, L., Pedone, A., Menziani, M. C., Adamo, C. & Labat, F. H_2 Dissociation and Water Evolution on Silver-Decorated $CeO_2(111)$: A Hybrid Density Functional Theory Investigation. *J. Phys. Chem. C* **123**, 25668–25679 (2019).
25. Brugnoli, L., Ferrari, A. M., Civalleri, B., Pedone, A. & Menziani, M. C. Assessment of Density Functional Approximations for Highly Correlated Oxides: The Case of CeO_2 and Ce_2O_3. *J. Chem. Theory Comput.* **14**, 4914–4927 (2018).
26. Erba, A., El-Kelany, Kh. E., Ferrero, M., Baraille, I. & Rérat, M. Piezoelectricity of $SrTiO_3$: An *ab initio* description. *Phys. Rev. B* **88**, (2013).
27. Shibuya, T., Yasuoka, K., Mirbt, S. & Sanyal, B. Bipolaron Formation Induced by Oxygen Vacancy at Rutile TiO_2 (110) Surfaces. *J. Phys. Chem. C* **118**, 9429–9435 (2014).
28. Ruiz Puigdollers, A., Schlexer, P., Tosoni, S. & Pacchioni, G. Increasing Oxide Reducibility: The Role of Metal/Oxide Interfaces in the Formation of Oxygen Vacancies. *ACS Catal.* **7**, 6493–6513 (2017).
29. Huang, M. & Fabris, S. Role of surface peroxo and superoxo species in the low-temperature oxygen buffering of ceria: Density functional theory calculations. *Phys. Rev. B* **75**, (2007).

30. Rasmussen, M. D., Molina, L. M. & Hammer, B. Adsorption, diffusion, and dissociation of molecular oxygen at defected TiO_2(110): A density functional theory study. *J. Chem. Phys.* **120**, 988–997 (2004).

31. Yin, W.-J., Wen, B., Zhou, C., Selloni, A. & Liu, L.-M. Excess electrons in reduced rutile and anatase TiO_2. *Surf. Sci. Rep.* **73**, 58–82 (2018).

32. Tan, S. *et al.* Molecular Oxygen Adsorption Behaviors on the Rutile TiO_2(110)-1×1 Surface: An in Situ Study with Low-Temperature Scanning Tunneling Microscopy. *J. Am. Chem. Soc.* **133**, 2002–2009 (2011).

33. Chrétien, S. & Metiu, H. O_2 evolution on a clean partially reduced rutile TiO_2(110) surface and on the same surface precovered with Au1 and Au2: The importance of spin conservation. *J. Chem. Phys.* **129**, 074705 (2008).

34. Tilocca, A. & Selloni, A. O_2 and Vacancy Diffusion on Rutile(110): Pathways and Electronic Properties. *ChemPhysChem* **6**, 1911–1916 (2005).

35. Naik, I. K. & Tien, T. Y. Small-polaron mobility in nonstoichiometric cerium dioxide. *J. Phys. Chem. Solids* **39**, 311–315 (1978).

36. Tuller, H. L. & Nowick, A. S. Defect Structure and Electrical Properties of Nonstoichiometric CeO_2 Single Crystals. *J. Electrochem. Soc.* **126**, 209–217 (1979).

37. Plata, J. J., Márquez, A. M. & Sanz, J. Fdez. Electron Mobility via Polaron Hopping in Bulk Ceria: A First-Principles Study. *J. Phys. Chem. C* **117**, 14502–14509 (2013).

38. Preda, G. *et al.* Formation of Superoxide Anions on Ceria Nanoparticles by Interaction of Molecular Oxygen with Ce^{3+} Sites. *J. Phys. Chem. C* **115**, 5817–5822 (2011).

39. Wendt, S. *et al.* Oxygen vacancies on TiO_2(110) and their interaction with H_2O and O_2: A combined high-resolution STM and DFT study. *Surf. Sci.* **598**, 226–245 (2005).

40. Jia, C., Zhang, G., Zhong, W. & Jiang, J. A First-Principle Study of Synergized O_2 Activation and CO Oxidation by Ag Nanoparticles on TiO_2(101) Support. *ACS Appl. Mater. Interfaces* **8**, 10315–10323 (2016).

41. Negreiros, F. R. & Fabris, S. Role of Cluster Morphology in the Dynamics and Reactivity of Subnanometer Pt Clusters Supported on Ceria Surfaces. *J. Phys. Chem. C* **118**, 21014–21020 (2014).

Chapter 7: Conclusions and future developments

The aim of this thesis was the development of a sound computational protocol to model the reactivity of ceria-based materials, based on the use of hybrid density functional theory and a wavefunction expansion in term of a gaussian-type orbitals basis set.

This approach was first assessed on the principal bulk properties of the cerium oxides CeO_2 and Ce_2O_3, and then on the modelling of the oxygen vacancy on the clean surface 111.

The results obtained are in close agreement with the published plane-wave results, though the latter method is less computationally demanding.

All the investigated properties are well or satisfactorily reproduced a part the energetic related to the reduction of ceria that seems out of reach for the hybrid methods tested, with the error increasing with the amount of exact exchange incorporate into the functional. In addition, the optimal amount of exact exchange to describe the bulk phases, 16 %, is not enough to well describe the properties of the vacancy, especially the localization of the occupied 4*f* states.

The incapability to simultaneously reproduce structural properties, localization features of the 4*f* states and energetics related to the interconversion Ce^{4+}/Ce^{3+} is an unsatisfying feature shared by all functional families. Similar issues have also been found for other rare-earth and actinide compounds and seem related to the difficult description of the *f* electrons in bonding.

This leaves an open question about the origin of this limitation: is DFT theory at fault with these systems or there is something wrong with the other approximations adopted?

To the best of my knowledge, a systematic assessment of the relativistic effects and of electron correlations with post-Hartree-Fock methods have been not performed yet on ceria or other rare-earth compounds with similar redox chemistry. Therefore, it would be interesting to explore this issue in future research.

The computational protocol used in this thesis has been firstly tested on the modelling of the substitutional doping with Cu and Ag of CeO_2 (111). Spontaneous formation of oxygen vacancies to compensate for the valence difference between Ce and dopants has been found.

Moreover, lower formation energies for active O vacancies at sites close to the dopant than on the undoped ceria has been found, confirming the general trends obtained in previously published plane-wave investigations. The results of experiments highlight very similar reducibility for the two different doped systems, while my results on the formation energies for the O vacancies indicate much higher reducibility for Ag-doped ceria. These differences can be ascribed to the limit of the simple model adopted for the doped surface, which, besides neglecting the mobility of the

ions, does not consider the formation of small dopant aggregates. Moreover, the Pt surface used to support the thin oxide films is likely to affect the redox chemistry within the ceria slab.
While ion's mobility and dopant clustering effects can be evaluated by considering larger supercells with multiple dopant atoms, modelling the metal-ceria interphase may result challenging. Besides requiring larger supercell to consider the lattice mismatch of Pt (111) and CeO_2 (111), troublesome convergence issues are expected when dealing also with doped and O defective systems.

A model of a supported silver cluster on ceria has been considered as a possible catalyst for the reactions of oxidation of H_2 and reduction of O_2, in virtue of the technological interest of these materials in applications in the fuel cells field, as a possible cheaper alternative to Pt-based electrocatalysts. The dissociation of these diatomic molecules occurs easier in the presence of the silver particle than on the bare ceria surface, especially at the three-phase-boundaries formed by the silver-oxide junction and the gas phase.
For the dissociation of O_2, the role of the support has been examined considering also the rutile, which has revealed to be less active with compared to ceria, due to an intrinsic lower ionicity.

The work done in this thesis is far to be enough to characterize a possible electrocatalyst based on ceria and Ag. Still, the results enlightened the role of the supported metal particle in modifying the reactivity in its proximity in comparison to the metal-free ceria, in particular facilitating the kinetic of key reaction-steps along the reaction mechanism elucidated.
Future works along this research route should investigate other different supported metals particles: the inclusion of Pt is mandatory, in order to elucidate the activity of the most active metal towards the reactions of interest in the PEFCs applications. Moreover, Ni and Pd which are more relevant for the SOFCs typology.
In the absence of experimental evidence of the most representative small cluster supported on ceria, I believe that the Me_{10} (7-3) cluster adopted in these investigations can also be used to study different supported metals.
This choice would reduce the variability of the results associated with the different sizes/shapes of the clusters, highlighting the role of the electronics effects, and it would help to extract electronic-based reactivity descriptors for the process at the TPB, similarly to the ones developed so far for reactions at oxides or metal surfaces.
Nevertheless, an evaluation of the effects of the size and shape of the cluster on the reactivity cannot be avoided, but the use of the Brønsted–Evans–Polanyi relation could prevent the

tremendous computational cost associated with the characterization of each transition state, by limiting the optimization of reagents and products of the critical reaction steps.

An exciting development for this line of research is the use of the *ab-initio* results obtained on the ceria for the re-parametrization of the available Reactive Force Field for cerium oxide, which has been found to suffers from many issues. This method would enable the investigation of the reactivity on larger and more morphologically complexes surfaces, made up to tens of thousands of atoms and including temperature and pressure effects, approaching the experimental conditions. However, the use of a force field, even if a reactive one, could prevent to grasp chemical process related to the interconversion Ce^{4+}/Ce^{3+} characterizing this unique material.

Appendix A

Table A1: list of the xc functionals employed in this work, with the most important parameters tabulated. c_{SR}, c_{MR}, c_{LR} indicate the fraction of Exact Exchange incorporated at Short, Medium and Long Range, respectively. The ω parameters define the length scale of the separation for the different RSHs.

Method	Name	Exchange	c_{SR}	c_{MR}	c_{LR}	ω_{SR}	ω_{LR}	Correlation
GGA	**PBE**	PBE						PBE
mGGA	**M06-L**	M06-L						M06-L
GH-mGGa	**M05**	M05	0.26	0.26	0.26	0	0	M05
	M05-2x	M05-2x	0.52	0.52	0.52	0	0	M05-2x
	M06	M06	0.27	0.27	0.27	0	0	M06
	M06-2x	M06-2x	0.54	0.54	0.54	0	0	M06-2x
	M06-HF	M06HF	1	1	1	0	0	M06HF
GH-GGA	**B3LYP**	B88	0.2	0.2	0.2	0	0	LYP
	B3PW91	B88	0.20	0.20	0.20	0	0	PWGGA
	PBE0	PBE	0.25	0.25	0.25	0	0	PBE
	PBE0-13	PBE	0.33	0.33	0.33	0	0	PBE
	PBEsol0	PBEsol	0.25	0.25	0.25	0	0	PBEsol
	PW1PW91	PWGGA	0.20	0.20	0.20	0	0	PWGGA
	WC1LYP	WCGGA	0.16	0.16	0.16	0	0	LYP
	B97H	B97	0.21	0.21	0.21	0	0	B97
	B1WC	WCGGA	0.16	0.16	0.16	0	0	PWGGA
SC-RSH	**HSE06**	PBE	0.25	0	0	0.11	0.11	PBE
	HSEsol	PBEsol	0.25	0	0	0.11	0.11	PBEsol
MC-RSH	**HISS**	PBE	0	0.6	0	0.84	0.2	PBE
LC-RSH	**LC-ωPBE**	PBE	0	0	1	0.4	0.4	PBE
	LC-ωPBEsol	PBEsol	0	0	1	0.6	0.6	PBEsol
	LC-ωBLYP	B88	0	0	1	0.6	0.6	LYP
	RSHXLDA	S	0	0	1	0.4	0.4	VWN
	ωB97	B97	0	0	1	0.4	0.4	B97
	ωB97X	B97	0.157706	0	1	0.3	0.3	B97
	CAM-B3LYP	B88	0.157706	0	1	0.33	0.33	LYP

Table A2. Computed cell parameter, bulk modulus and independent elastic tensor components for CeO_2.

Method	a(Å)	B_0 (GPa)	c11(GPa)	c21(GPa)	c44(GPa)
Experimental	5.411, 5.406, 5.390	204,220,230,236	403	105	60
LC-ωBLYP	5.445	212.3	417.3	109.8	52.6
LC-ωPBE	5.384	226.3	438.2	120.3	59.7
LC-ωPBEsol	5.354	248.5	482.0	131.8	78.4
RSHXLDA	5.399	220.2	432.2	114.2	59.5
CAM-B3LYP	5.431	214.4	417.8	112.7	59.7
ωB97X	5.450	211.6	418.6	108.1	48.6
ωB97	5.456	207.8	418.0	102.7	41.1
HISS	5.387	225.4	436.7	119.8	66.6
HSEsol	5.368	224.5	426.4	123.5	68.9
HSE06	5.408	211.2	408.0	112.8	61.2
PBE0	5.407	212.6	411.3	113.3	61.7
PBEsol0	5.368	225.7	429.4	123.8	69.3
PBE0-13	5.392	222.7	432.3	117.8	65.8
B97H	5.458	196.2	377.7	105.5	56.8
B3PW91	5.424	209.5	405.5	111.5	60.5
PW1PW91	5.417	207.1	398.6	111.4	59.7
B3LYP	5.473	193.5	378.8	100.8	53.0
B1WC	5.388	214.6	404.9	119.4	65.5
WC1LYP	5.449	200.3	383.0	108.9	59.0
M06	5.448	206.1	397.3	110.5	42.9
M05	5.494	190.2	375.8	97.4	36.0
M06-2x	5.423	229.8	439.9	124.8	62.8
M05-2x	5.402	241.1	457.5	132.9	87.3
M06-HF	5.377	267.8	497.5	153.0	117.9
M06L	5.503	177.8	343.8	94.8	45.1
PBE	5.471	176.9	337.3	96.7	51.0
HF	5.470	228.2	469.2	107.7	83.7

Table A3. Computed cell parameter, bulk modulus and independents elastic tensor component for Ce_2O_3

Method	a(Å)	c(Å)	c/a	$B_{0\,(H)}$ (GPa)	C_{11} (GPa)	C_{12} (GPa)	C_{13} (GPa)	C_{33} (GPa)	C_{44} (GPa)
Experimental	3.891	6.059	1.56	111					
LC-ωBLYP	3.896	6.192	1.589	132.4	231.7	130.7	89.5	154.8	73.0
LC-ωPBE	3.866	6.034	1.561	139.4	247.1	139.4	96.9	155.3	80.8
LC-ωPBEsol	3.854	5.993	1.555	147.4	264.3	148.4	102.5	161.7	88.1
RSHXLDA	3.868	6.119	1.582	134.9	239.6	134.1	90.1	157.2	74.5
ωB97X	3.895	6.209	1.594	135.4	230.6	136.1	92.5	159.1	72.9
ωB97	3.901	6.231	1.585	133.5	224.1	134.2	89.7	161.4	70.6
CAM-B3LYP	3.883	6.143	1.582	135.6	236.4	135.4	92.1	157.2	72.5
HISS	3.864	6.042	1.563	140.1	248.4	141.4	97.1	155.1	77.2
HSEsol	3.847	5.955	1.548	143.4	251.5	146.4	101.4	156.2	78.3
HSE06	3.870	6.055	1.565	135.8	237.5	137.4	94.4	151.4	72.1
PBE0	3.869	6.055	1.565	136.1	237.9	137.8	94.4	152.0	72.8
PBEsol0	3.847	5.956	1.548	143.9	252.2	146.8	101.7	157.0	79.1
PBE0-13	3.865	6.044	1.564	138.8	243.4	140.8	96.1	154.8	75.4
B97H	3.896	6.135	1.575	131.1	226.8	124.3	89.8	155.9	72.0
B3PW	3.874	6.078	1.569	133.8	232.9	135.0	92.2	151.2	70.5
PW1PW91	3.871	6.056	1.564	135.7	236.1	137.2	94.3	152.1	71.8
B3LYP	3.897	6.200	1.591	131.7	234.4	135.4	95.2	156.3	74.5
B1WC	3.852	5.963	1.548	141.4	245.6	144.2	100.0	155.1	76.5
WC1LYP	3.883	6.108	1.573	134.1	231.3	135.1	92.3	153.6	69.5
M06	3.870	6.172	1.595	145.5	237.7	143.0	102.3	173.5	75.9
M05	3.906	6.249	1.600	127.6	220.4	118.9	84.7	155.0	67.4
M06-2x	3.887	6.088	1.566	142.5	243.8	146.1	105.7	150.1	81.1
M05-2x	3.889	6.046	1.555	140.2	246.6	147.7	98.7	149.7	81.6
M06-HF	3.866	5.987	1.548	155.3	274.1	163.4	109.9	165.9	93.7
M06L	3.930	5.970	1.519	122.2	221.2	132.4	91.8	116.6	69.3
PBE	3.879	6.059	1.562	108.6	201.3	104.6	74.9	114.8	57.8
HF	3.930	6.256	1.592	131.5	241.7	126.7	86.4	153.5	73.2

Table A4. Harmonic vibrational frequencies calculated at the Γ point for CeO_2 and Ce_2O_3.

	CeO_2		Ce_2O_3							
Method	T_{1u}	T_{2g}	E_g	A_{1g}	E_g	A_{1g}	E_u	A_{2u}	E_u	A_{2u}
Experimental	272[19]-276[20]	465[79,83,84]	103[67]	189[67]	409[67]	409[67]	-	-	-	-
LC-ωBLYP	283	460	102	189	421	432	169	209	389	473
LC-ωPBE	298	472	110	197	432	437	220	230	396	479
LC-ωPBEsol	314	505	116	207	453	452	235	247	418	494
RSHXLDA	288	468	107	194	427	438	201	218	388	478
ωB97X	249	461	103	193	429	441	201	213	388	475
ωB97	245	446	102	194	419	446	197	218	377	475
CAM-B3LYP	288	465	106	193	424	431	200	214	386	473
HISS	297	474	110	198	433	434	213	228	398	479
HSEsol	304	473	108	205	427	430	211	221	392	462
HSE06	288	461	107	193	423	424	205	218	387	467
PBE0	290	463	107	192	423	425	202	219	388	467
PBEsol0	303	474	112	201	435	432	224	236	399	473
PBE0-13	294	476	108	199	433	450	205	212	399	501
B97H	164	444	105	195	396	424	202	224	367	478
B3PW	285	454	105	190	418	422	193	214	382	464
PW1PW	288	457	106	192	421	422	204	218	384	464
B3LYP	270	443	100	183	410	418	179	195	372	458
B1WC	301	462	110	198	429	425	221	232	393	466
WC1LYP	285	449	105	191	418	421	212	213	378	461
M06	246	446	102	193	412	423	204	197	376	480
M05	178	431	97	191	384	429	180	216	349	474
M06-2x	324	472	111	195	434	436	236	223	401	484
M05-2x	378	499	107	199	469	428	227	212	437	475
M06-HF	446	548	119	207	487	433	276	218	444	511
M06L	256	425	109	191	390	423	218	235	373	424
PBE	272	424	103	182	399	400	199	205	363	421
HF	280	517	106	191	440	443	201	203	413	479

Table A5. Band gaps for CeO_2: the band gaps are extracted from the DOSS with a 12x12x12 k-point mesh. The gap 2*p* – 4*f* is between the valence edge composed by the filled O 2*p* and the bottom of the 4*f* band. The gap 2*p* - 5*d* is between the the valence edge composed by the filled O 2*p* and the bottom of the 5*d* band (conduction band).

Methods	**2*p* - 4*f* (eV)**	**2*p* - 5*d* (eV)**	**4*f* – 5*d* (eV)**
Experimental	2.6-3.9[9]	5.5 - 8.4[9]	
LC-ωBLYP	8.21	13.04	3.64
Lc-ωPBE	8.32	13.06	3.32
Lc-ωPBEsol	10.13	14.04	2.57
RSHXLDA	8.34	13.04	3.44
ωB97-X	8.12	12.51	3.16
ωB97	8.09	13.03	3.68
CAM-B3LYP	6.41	10.59	3.03
HISS	4.27	8.17	2.81
HSEsol	3.75	7.42	2.50
HSE06	3.67	7.42	2.62
PBE0	4.35	8.18	2.76
PBEsol0	4.40	8.12	2.55
PBE0-13	5.27	8.79	2.42
B97H	3.43	7.42	2.82
B3PW	3.27	7.51	3.12
PW1PW91	3.80	7.88	3.04
B3LYP	3.77	7.79	2.95
B1WC	3.83	7.78	2.91
WC1LYP	3.68	7.82	3.19
M05	3.86	8.35	3.48
M052x	7.45	10.63	2.05
M06	3.95	8.27	3.31
M06-2x	6.78	10.67	2.73
M06-HF	12.65	14.14	0.13
M06L	1.98	6.73	3.63
PBE	1.90	6.28	3.22
HF	14.47	16.00	0

Table A6. Band gaps Ce_2O_3: band gaps obtained from DOSS with shrink 12x12x12. The fundamental gap, 4*f* - 5*d*, is between the valence edge composed by filled 4*f* states and the conduction bottom made of a combination of 4*f* and 5*d* empty states. Empty slots for HF and M06-HF results are due to mixing of the O 2*p* and Ce 4*f* valence bands.

Method	4*f* - 4*f*/5*d* (eV)	2*p* - 4*f* (eV)	2*p* - 4*f*/5*d* (eV)
Experiments	2.40 (optical gap)[16]	≈2	≈ 6
LC-ωBLYP	9.28	1.09	11.32
Lc-ωPBE	8.83	1.47	11.23
Lc-ωPBEsol	10.56	0.87	12.55
RSHXLDA	8.61	1.80	11.28
ωB97-X	8.73	1.26	10.9
ωB97	9.22	1.10	11.22
CAM-B3LYP	6.76	1.53	8.99
HISS	4.42	1.47	6.71
HSEsol	2.67	2.45	5.78
HSE06	3.08	2.24	5.84
PBE0	3.82	2.07	6.54
PBEsol0	3.36	2.36	6.47
PBE0-13	4.94	1.74	7.41
B97H	3.59	1.96	6.2
B3PW	3.20	2.25	6.1
PW1PW91	3.06	2.32	5.99
B3LYP	3.45	2.07	6.07
B1WC	2.30	2.9	5.74
WC1LYP	2.58	2.51	5.63
M05	5.02	0.98	6.71
M052x	8.34	0.10	8.93
M06	3.98	1.80	6.38
M06-2x	7.60	0.40	9.10
M06-HF	11.90	-	-
M06L	0.60	3.10	4.14
PBE	0.00	3.30	3.88
HF	13.00	-	-

Table A7: Cohesive Energies for the primitive cells of CeO_2 and Ce_2O_3

Method	E_{coh} CeO_2(eV)	E_{coh} Ce_2O_3(eV)
Exp (Tabulated)	-20.74	-34.99
CAM-B3LYP	-19.02	-33.28
Lc-ωBLYP	-18.24	-32.75
Lc-ωPBE	-19.16	-34.00
Lc-ωPBEsol	-19.53	-35.19
RSHXLDA	-19.96	-34.93
HISS	-18.84	-33.29
ωWB97X	-18.96	-33.61
ωB97	-18.64	-33.56
HSEsol	-20.69	-35.12
HSE06	-19.42	-33.37
PBE0	-19.37	-33.36
PBEsol0	-20.64	-35.10
PBE0-13	-19.13	-33.25
B1WC	-20.79	-35.07
WC1LYP	-20.20	-34.18
B97H	-19.29	-33.34
B3PW	-19.18	-32.90
PW1PW91	-18.62	-33.65
B3LYP	-18.76	-32.25
M06L	-20.76	-35.07
M06	-19.20	-33.46
M06-2x	-18.61	-33.90
M06-HF	-20.09	-36.31
M05	-17.73	-31.59
M05-2x	-18.97	-34.37
PBE	-20.79	-34.39
HF	-25.50	-43.04

Table A8: Energy for the reactions of reduction R1 and R2. Results were reported for BS Ce2/O1 optimized structures of the oxides and for single points energy calculations with BS Ce3/O2 on the structures previously optimized with basis set Ce2/O1. For R1 we compare the results obtained with two different reference for O_2: Columns 2 and 4 are respect ½ O_2 (triplet state), columns 3 and 5 are respect the sum of the electronic energy of O(triplet state) and half experimental binding energy for O_2 (2.58 eV).

Method	ΔU R1 (½ O_2) (eV) BS Ce2/O1	ΔU R1 (O +½ O_2 exp. binding) (eV) BS Ce2/O1	ΔU R1 (½ O_2) (eV) BS Ce3/O3	ΔU R1 (O +1/2 O_2 exp. binding) (eV) BS Ce3/O2	ΔU R2 (eV) BS Ce3/O2
Experiments	4.03				1.54
CAM-B3LYP	2.92	2.57	2.08	2.17	-0.44
LC-ωBLYP	1.95	1.57	1.08	1.13	-1.38
Lc-ωPBE	2.40	2.14	1.53	1.73	-0.99
Lc-ωPBEsol	2.23	1.70	1.26	1.29	-1.50
RSHXLDA	2.85	2.87	1.91	2.40	-0.70
HISS	2.66	2.11	1.84	1.79	-0.83
ωB97X	2.49	2.15	1.61	1.72	-0.89
ωB97	1.90	1.58	1.00	1.14	-1.45
HSEsol	4.17	4.01	3.37	3.67	0.76
HSE06	3.62	3.28	2.78	2.88	0.26
PBE0	3.54	3.19	2.69	2.80	0.17
PBEsol0	4.09	3.93	3.29	3.59	0.67
PBE0-13	3.32	2.81	2.46	2.42	-0.10
B1WC	4.29	4.23	3.56	3.93	1.00
WC1LYP	4.06	3.97	3.32	3.63	0.80
B97H	3.27	3.03	2.49	2.66	0.00
B3PW	3.54	3.23	2.76	2.87	0.29
PW1PW	3.73	3.47	3.09	3.25	0.41
B3LYP	3.37	3.03	2.61	2.67	0.17
M06L	4.47	4.17	3.78	3.87	1.39
M06	3.16	2.73	2.35	2.35	-0.26
M06-2x	1.66	1.22	0.69	0.73	-1.88
M06-HF	2.50	1.81	1.41	1.27	-1.29
M05	2.04	1.63	1.25	1.28	-1.27
M052x	2.29	1.80	0.98	0.98	-1.66
PBE	4.81	4.98	4.08	4.60	1.69
HF	7.55	5.98	6.28	5.37	-0.54

Appendix B

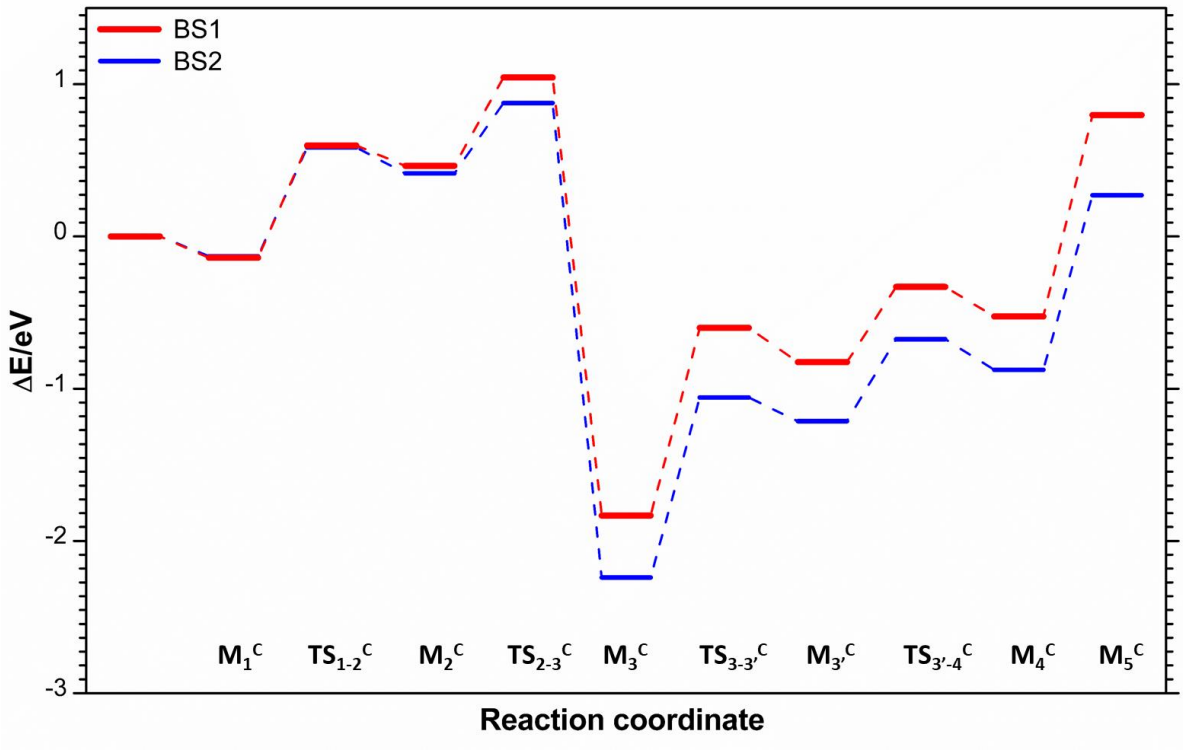

Figure B1: Energy profiles for the H_2 dissociation and H_2O formation along the most energetically-favoured path on pristine CeO_2 (111) computed with both BS1 and BS2 basis sets.

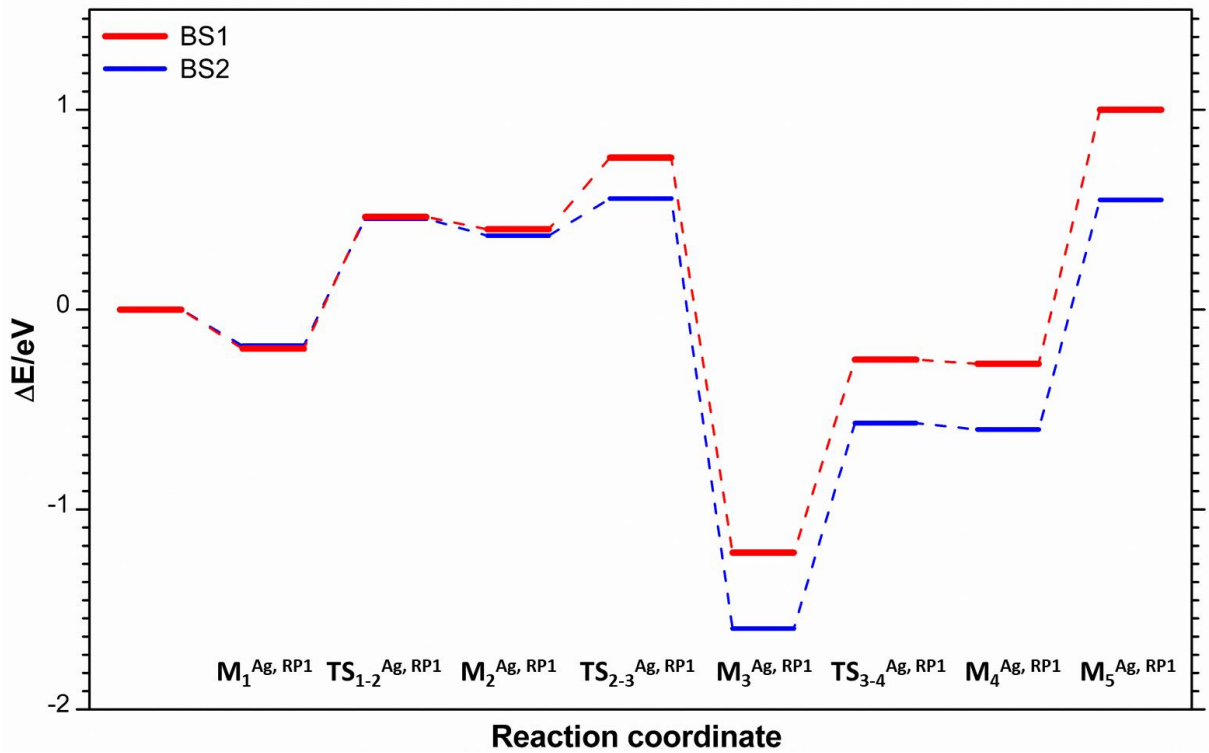

Figure B2: Energy profiles for the H_2 dissociation and H_2O formation along the reaction path RP1 on pristine Ag_{10}/CeO_2 (111) computed with both BS1 and BS2 basis sets.

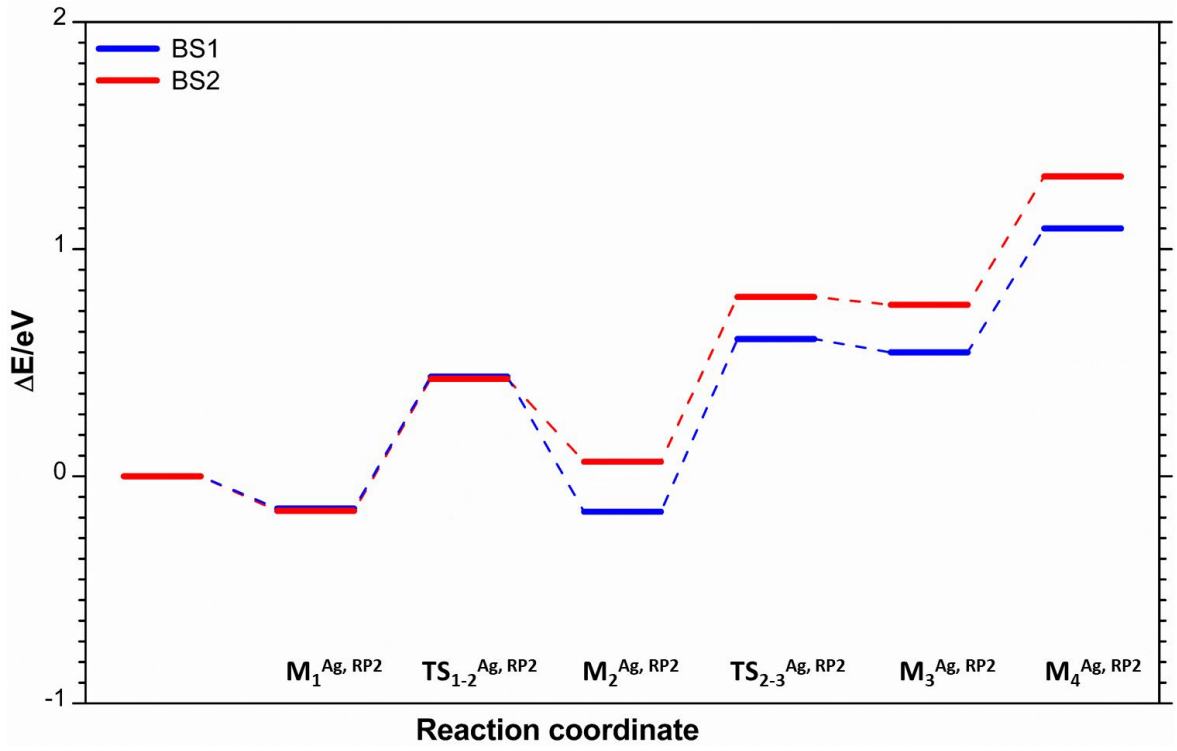

Figure B3: Energy profiles for the H_2 dissociation and H_2O formation along the reaction path RP2 on pristine Ag_{10}/CeO_2 (111) computed with both BS1 and BS2 basis sets

Table B1. Selected atomic charges (Q, in $|e^-|$) and distances (d, in Å) for structures associated with the water formation dissociation on clean CeO_2 and on Ag_{10}/CeO_2 along the RP1 path. O^3 is the subsurface O involved in the two step H transfer. The other atoms correspond to those defined in Table 2 in chapter 5.

	$Q(H^1/H^2)$	$Q(O^1/O^2)$	$Q(Ce^1)$	$Q(Ag_{10})$	$d(O^1\text{-}H^1)$	$d(H^2\text{-}O^1)$	$d(H^2\text{-}O^2)$	$d(H^2\text{-}Ce^1)$	$d(O^1\text{-}Ce^2)$	$d(O^3\text{-}H^2)$	d(H-Ag)
$TS_{3\text{-}3'}^{C}$	0.23/0.31	-1.00/-1.12	2.13	-	0.967	3.307	-	2.182	-	1.200	-
$M_{3'}$	0.23/0.25	-1.00/-0.99	2.13	-	0.964	2.910	-	2.171	-	0.876	-
$TS_{3'\text{-}4}^{C}$	0.28/0.31	-1.00/-1.30	2.13	-	0.970	1.126	-	2.234	-	1.515	-
$TS_{3\text{-}4}^{C}$	0.24/-0.14	-0.81/-1.22	2.48	-	0.967	1.423	3.003	2.348	-	-	-
M_4^{C}	0.30/0.25	-0.64	2.16	-	1.032	0.963	-	-	2.610	-	-
$TS_{3\text{-}4}^{Ag,\ RP1}$	0.21/0.41	-0.89/-1.14	2.15	1.28	0.960	1.141	1.455	2.492	2.762	-	2.796
$M_4^{Ag,\ RP1}$	0.30/0.25	-0.63/-1.30	2.14	1.26	1.026	0.962	-	-	2.662	-	5.575

Table B2. Selected atomic charges (Q, in $|e^-|$) and distances (d, in Å) for the structures associated with the H_2 dissociation and water formation on $Ag_{10}/CeO_2(111)$ along the RP2 path (see Figure 11 of chapter 5 for the corresponding structures). Ag^1 and Ag^2 are respectively at the edge on top of the cluster on the side of the H_2 adsorption. H^1 and H^2 are respectively the H farther and closest to the oxide surface. O is at the edge of the cluster. Ce^1 correspond to the closest Ce to the water molecule.

	$Q(H^1/H^2)$	Q(O)	$Q(Ag^1/Ag^2)$	$Q(Ag_{10})$	$d_{H\text{-}H}$	$d(Ag^1\text{-}H^1)$	$d(Ag^1\text{-}H^2)$	$d(Ag^2\text{-}H^1)$	$d(H^2\text{-}O)$	$d(H^1\text{-}O)$	d(O-Ce)
$M_1^{Ag,\ RP2}$	-0.05/-0.05	-1.26	0.18/0.04	1.33	0.751	2.700	2.675	3.936	2.898	3.425	-
$TS_{1\text{-}2}^{Ag,\ RP2}$	-0.22/0.17	-1.21	0.13/0.04	1.29	0.961	1.889	1.952	4.094	1.352	2.308	-
$M_2^{Ag,\ RP2}$	-0.40/0.23	-0.96	0.31/0.19	1.64	3.489	1.8324	2.421	1.9439	0.970	3.768	-
$TS_{2\text{-}3}^{Ag,\ RP2}$	-0.11/0.24	-0.49	-0.05/0.05	1.04	1.595	2.083	-	-	0.966	1.012	2.559
$M_3^{Ag,\ RP2}$	-0.12/0.25	-0.46	-0.06/-0.07	1.01	-	2.170	-	-	0.965	0.985	2.554